Simula SpringerBriefs on Computing 17
Reports on Computational Physiology

Kimberly J. McCabe *Editor*

Computational Physiology

Simula Summer School 2023 – Student Reports

simula

OPEN ACCESS

Springer

Simula SpringerBriefs on Computing

Reports on Computational Physiology

Volume 17

About this series

In 2016, Springer and Simula launched an Open Access series called the Simula SpringerBriefs on Computing. This series aims to provide concise introductions to the research areas in which Simula specializes: scientific computing, software engineering, communication systems, machine learning and cybersecurity. These books are written for graduate students, researchers, professionals and others who are keenly interested in the science of computing, and each volume presents a compact, state-of-the-art disciplinary overview and raises essential critical questions in the field.

Simula's focus on computational physiology has grown considerably over the last decade, with the development of multi-scale mathematical models of excitable tissues (brain and heart) that are becoming increasingly complex and accurate. This subseries represents a new branch of the SimulaSpringer Briefs that is specifically focused on computational physiology. Each volume in the series will introduce and explore one or more sub-fields of computational physiology, and present models and tools developed to address the fundamental research questions of the field. Whenever possible, the software used will be made publicly available.

By publishing the Simula SpringerBriefs on Computing and the sub-series on computational physiology, Simula Research Laboratory acts on its mandate of emphasizing research education. Books in the series are published by invitation from one of the editors, and authors interested in publishing in the series are encouraged to contact any member of the editorial board.

Kimberly J. McCabe
Editor

Computational Physiology

Simula Summer School 2023 – Student Reports

simula

Springer

Editor
Kimberly J. McCabe
Simula Research Laboratory
Oslo, Norway

ISSN 2512-1677 ISSN 2512-1685 (electronic)
Simula SpringerBriefs on Computing
ISSN 2730-7735 ISSN 2730-7743 (electronic)
Reports on Computational Physiology
ISBN 978-3-031-53144-6 ISBN 978-3-031-53145-3 (eBook)
https://doi.org/10.1007/978-3-031-53145-3

This work was supported by Simula Research Laboratory.

This Springer imprint is published by the registered company Springer Nature Switzerland AG
The registered company address is: Gewerbestrasse 11, 6330 Cham, Switzerland

Paper in this product is recyclable.

Series Foreword

Dear reader,

The series *Simula SpringerBriefs on Computing* was established in 2016, with the aim of publishing compact introductions and state-of-the-art overviews of select fields in computing. Research is increasingly interdisciplinary, and students and experienced researchers both often face the need to learn the foundations, tools, and methods of a new field. This process can be demanding, and typically involves extensive reading of multidisciplinary publications with different notations, terminologies and styles of presentation. The briefs in this series are meant to ease the process by explaining important concepts and theories in a specific interdisciplinary field without assuming extensive disciplinary knowledge and by outlining open research challenges and posing critical questions in the field.

Simula has a major research program in computational physiology that includes a long and close collaboration with the University of California (UC) San Diego. To reflect this research focus, we established in 2020 a new subseries entitled *Simula Springer Briefs on Computing - Reports on Computational Physiology*. The subseries includes both introductory and advanced texts on select fields of computational physiology, designed to advance interdisciplinary scientific literacy and promote effective communication and collaboration in the field. This subseries is also the outlet for collections of reports from the annual Summer School in Computational Physiology, organized by Simula, University of Oslo, and UC San Diego. The school starts in June each year with students spending two weeks in Oslo learning the principles underlying mathematical models commonly used in studying the heart and the brain. During their stay in Oslo, students are assigned a research project to work on over the summer. In August, they travel to San Diego for another week of training and project work, and a final presentation of their findings. Every year, we have been impressed by the students' creativity and we often see results that could lead to a scientific publication. Starting with the 2021 edition of the summer school, we have taken the course one step further by having each team conclude their project with a scientific report that can pass rigorous peer review as a publication in this new series.

All items in the main series and the subseries are published within the SpringerOpen framework, as this will allow authors to use the series to publish an initial version of their manuscript that could subsequently evolve into a full-scale book on a broader theme. Since the briefs are freely available online, the authors do not receive any direct income from the sales; however, remuneration is provided for every completed manuscript. Briefs are written on the basis of an invitation from a member of the editorial board.

Suggestions for possible topics are most welcome, and interested authors are encouraged to contact a member of the editorial board.

March 2023

Dr. Joakim Sundnes
sundnes@simula.no

Dr. Kimberly J. McCabe
kimberly@simula.no

Dr. Andrew McCulloch
amcculloch@ucsd.edu

Dr. Aslak Tveito
aslak@simula.no

Preface

Since 2014, we have organized an annual summer school in computational physiology. The school starts in June each year and the graduate students spend two weeks in Oslo learning the principles underlying mathematical models commonly used in studying the heart and the brain. At the end of their stay in Oslo, the students are assigned a research project to work on over the summer. In August the students travel to the University of California, San Diego to present their findings. Each year, we have been duly impressed by the students' progress and we have often seen that the results contain the rudiments of a scientific paper.

Starting in the 2021 edition of the summer school, we have taken the course one step further and aim to conclude every project with a scientific report that passes rigorous peer review as a publication in this new series called *Simula SpringerBriefs on Computing – reports on computational physiology*.

One advantage of this course adjustment is that we have the opportunity to introduce students to scientific writing. To ensure the students get the best introduction in the shortest amount of time, we have commissioned a professional introduction to science writing by Nature. The students participate in a *Nature Masterclasses* workshop in order to strengthen skills in high quality scientific writing and publishing. The workshop is tailored to publications in the field of computational physiology and allows students to gather real-time feedback on their reports.

We would like to emphasise that the contributions in this series are brief reports based on the intensive research projects assigned during the summer school. Each report addresses a specific problem of importance in physiology and presents a succinct summary of the findings (8-15 pages). We do not require that results represent new scientific results; rather, they can reproduce or supplement earlier computational studies or experimental findings. The physiological question under consideration should be clearly formulated, the mathematical models should be defined in a manner readable by others at the same level of expertise, and the software used should, if possible, be made publicly available. All reports in this series are subjected to peer-review by the other students and supervisors in the program.

We would like to express our gratitude for the very fruitful collaboration with Springer -Nature and in particular with Dr. Martin Peters, the Executive Editor for Mathematics, Computational Science and Engineering.

The editors of *Simula SpringerBriefs on Computing – Reports on Computational Physiology*:

Oslo, Norway
November 2023

Kimberly J McCabe
Andrew D McCulloch
Aslak Tveito
Jennifer L Hazen

Acknowledgements

The Simula Summer School in Computational Physiology is a team effort, with many scientists contributing their time to give lectures and advise projects for the students. We would like to thank the lecturers and project advisors for their expertise and willing participation in the course: Dr. Hermenegild Arevalo, Dr. Pietro Benedusi, Dr. Jørgen Dokken, Dr. Andrew Edwards, Dr. Ada Johanne Ellingsrud, Dr. Henrik Finsberg, Dr. Nickolas Forsch, Konstantin Holzhausen, Dr. Zeinab Jahed, Dr. Mikkel Lepperød, Dr. Glenn Lines, Dr. Molly Maleckar, Maria Hernandez Mesa, Dr. Kimberly McCabe, Dr. Andrew McCulloch, Lena Myklebust, Oscar Odeigah, Dr. Padmini Rangamani, Dr. Marie Rognes, Vemund Schøyen, Dr. Joakim Sundnes, Dr. Marte Julie Sætra, Dr. Aslak Tveito, Julie Johanne Uv, Dr. Daniela Valdez-Jasso, Dr. Kristian Valen-Sendstad, and Dr. Samuel Wall.

Administrative support for the school was provided by Dr. Kimberly McCabe, Dr. Andy Edwards, Dr. Nickolas Forsch, Dr. Rachel Thomas, Dr. Stian Engen, and Hanie Tampus. At UCSD, we received vital administrative support from Jennifer Stowe. Formatting support for this volume was provided by Dr. Jennifer Hazen.

The Simula Summer School in Computational Physiology is supported through the Simula-UiO-UCSD Research PhD Training Programme (SUURPh), an endeavour funded by the Norwegian Ministry of Education and Research. Additional financial support is derived from SIMENT, an INTPART mobility grant from the Norwegian Research Council. The school also received funding from Digital Life Norway (DLN) to support student mobility.

Contents

Chapter 1
Studying the Role of Astrocytic Membrane Properties on Microscopic Fluid Flow in Brain Tissue

Nigar Abbasova, Adyant Balaji, Elena Bernardelli, Ada J Ellingsrud, and Marte J Sætra

Abstract The role of astrocyte networks in brain volume homeostasis and waste clearance has not received enough attention from the neuroscience community. However, recent research efforts indicate that glial cells are crucial for fluid flow through brain tissue, contributing to clearance and maintenance of brain volume. We examine the role of various glial cotransporters in the spatial and temporal changes of the intra- and extracellular volume fractions and fluid dynamics via computational modelling. The model is incorporated within the Kirchhoff-Nernst-Planck electrodiffusive framework and takes into account ionic electrodiffusion and fluid dynamics. Our research shows that all model configurations demonstrate similar fluid fluxes, except those involving HCO_3^- dynamics. The model configuration that included the NBC cotransporter was observed to have the greatest intracellular total volume-weighted fluid velocity of 16 μm/s.

Nigar Abbasova
Department of Physics, University of Oslo, NO

Adyant Balaji
Department of Bioengineering, University of California San Diego, USA

Elena Bernardelli
Department of Mathematics, University of Trento, IT

Ada J Ellingsrud
Department of Numerical Analysis and Scientific Computing, Simula Research Laboratory, NO

Marte J Sætra (corresponding author)
Department of Numerical Analysis and Scientific Computing, Simula Research Laboratory, NO
e-mail: martejulie@simula.no

K. J. McCabe (ed.), *Computational Physiology*, Simula SpringerBriefs on Computing 17,
https://doi.org/10.1007/978-3-031-53145-3_1

1.1 Introduction

Although astrocytes comprise a large part of the glial cell population in the mammalian brain [1], the role of astrocyte networks has not received enough attention from the neuroscience community. However, recent research within astrocytic networks and brain clearance pathways shows that astrocytes are likely to be crucial for fluid flow through brain tissue, which contributes primarily to brain volume homeostasis and waste clearance [2]. One of the key questions that has yet to be understood relates to the role of the astrocytic membrane and its effect on the flow of transmembrane and compartmental fluid. Another closely related phenomenon is the shrinkage of the extracellular space between neurons and surrounding astrocytes during neuronal stimulation [3].

Østby et al. 2009 [3] studied the extracellular shrinkage induced by neural activity by investigating the astrocytic membrane mechanisms. They report that $Na^+/K^+/Cl^-$ (NKCC1) and Na^+/HCO_3^- (NBC) cotransporters appear to be crucial factors in achieving the measurable extent of the shrinkage of the extracellular space (ECS). Jin et al. [4] studied the dynamics of extracellular K^+ ions during neural stimulation and the effect of the membrane water channel aquaporin-4 (AQP4) in astrocytes. However, both authors ([3, 4]) excluded spatial effects from consideration, thus preventing them from looking into intracompartmental gradients. Afterwards, Sætra et al. 2023 [2] introduced a computational framework to characterise the spatial and temporal dynamics of the astrocytic network triggered by neural activity. However, the authors were able to estimate the electrochemomechanical response as well as the water movement within the compartments of the astrocytic network without studying the effects of different membrane mechanisms.

In this work, we implement other membrane mechanisms in the framework of Sætra et al. 2023 [2] and evaluate how they affect microscopic fluid flow in brain tissue. We do so by analysing the fluid velocities in the astrocyte network and the extracellular space surrounding it. We also investigate the effect of the new membrane mechanisms on the spatial and temporal dynamics of the intra- and extracellular volume fractions. Our base model for membrane mechanisms includes Na^+, K^+ and Cl^- leak channels with a Na^+/K^+ pump. We explore other model configurations by expanding on the base model by adding different combinations of the K^+-coupled Cl^- transporter (KCC1), the Na^+-coupled HCO_3^- transporter (NBC) and the $Na^+/K^+/Cl^-$ (NKCC1) cotransporter. The different model configurations are adopted from Østby et al. 2009 [3]. Our research revealed that all models demonstrate similar ionic fluxes, apart from those involving HCO_3^- dynamics. Additionally, these model configurations had the highest total fluid velocities, both in the intra- and extracellular spaces. The highest intracellular and extracellular fluid velocity observed was 16 μm/min in the model configuration that involved the NBC cotransporter.

1.2 Methods

1.2.1 Modelling Fluid Flow Through Astrocyte Networks

Our aim is to predict the temporal and spatial evolution of the volume fraction α_r, ion concentrations $[Na^+]_r$, $[K^+]_r$, $[Cl^-]_r$ and $[HCO_3^-]_r$, electric potential ϕ_r, and hydrostatic pressure p_r in the intracellular space (ICS, $r = i$) and the extracellular space (ECS, $r = e$). To do so, we build on a model developed by Sætra et al. [2], which models the system as a 1D domain of length 300 μm representing the tissue between two blood vessels. See Figure 1 for a visualisation of the system.

To model compartmental fluid flow, we implement the M3 model scenario from Sætra et al. 2023 [2]. The intracellular fluid flow is driven by hydrostatic and osmotic forces, while the extracellular fluid flow is driven by hydrostatic and electro-osmotic forces. The fundamental basis of the model is the electrodiffusive Kirchhoff-Nernst-Planck framework, and the model dynamics is described using coupled partial differential equations. See Sætra et al. 2023 [2] Section 4.2 for more details.

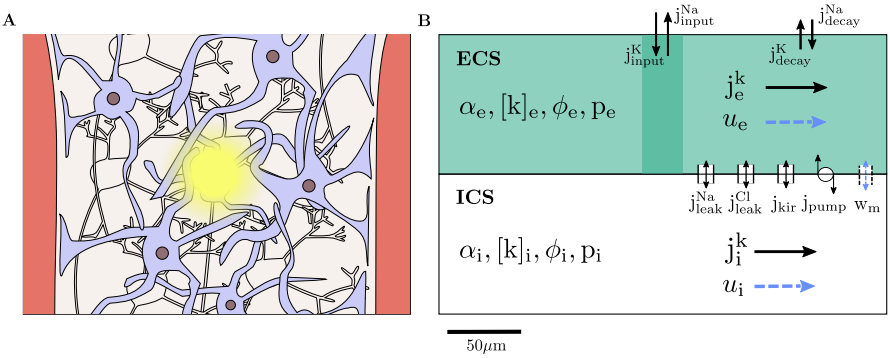

Fig. 1: Representation of the model devised by Sætra et al. (reproduced with permission from Sætra et al. 2023) [2]. A: Brain tissue between two blood vessels with astrocytes (purple), neurons (grey), and ECS with neuronal activity in the middle. B: System represented as 1D domain, including ICS (astrocytes) and ECS. The neuronal activity is represented by the input currents of Na^+ and K^+ (j^{K}_{input} and j^{Na}_{input}) in the input zone and the decay currents (j^{K}_{decay} and j^{Na}_{decay}) throughout the domain. The transmembrane currents are modelled as an inward rectifying K^+ current (j_{Kir}), Na^+ and Cl^- leak currents (j^{Na}_{leak} and j^{Cl}_{leak}), as well as a Na^+/K^+ pump current (j_{pump}). Intracellular and extracellular currents (j^{k}_{i} and j^{k}_{e}) are driven by electrodiffusion and advection. The compartmental fluid flow in the intracellular and extracellular space is denoted by u_i and u_e, respectively, and the transmembrane fluid flow is denoted by w_m.

1.2.2 Modelling Neuronal Activity

Sætra et al. 2023 model neuronal activity as a stimulus in the form of an external input flux of K^+ ions into the ECS and the simultaneous removal of Na^+ ions from active neurons within the input zone. We implement the same method with the input zone defined in the interval $[L_1, L_2]$ with $L_1 = 1.35 \cdot 10^{-4}$ m and $L_2 = 1.65 \cdot 10^{-4}$ m, during time interval [10 s, 20 s]. We model the input fluxes by following the same framework:

$$j^{\mathrm{K}}_{\mathrm{input}} = -j^{\mathrm{Na}}_{\mathrm{input}} = j_{\mathrm{in}}. \tag{1.1}$$

Here, $j^{\mathrm{K}}_{\mathrm{input}}$ is the input flux for potassium, $j^{\mathrm{Na}}_{\mathrm{input}}$ is the input flux for sodium and j_{in} $(\mathrm{mol}/(\mathrm{m}^2\mathrm{s}))$ is a constant.

Similarly, the decay of both of these ions from the extracellular space due to neuronal pumps and cotransporters is represented by the decay fluxes,

$$j^{\mathrm{K}}_{\mathrm{decay}} = -j^{\mathrm{Na}}_{\mathrm{decay}} = -k_{\mathrm{dec}}([\mathrm{K}^+]_{\mathrm{e}} - [\mathrm{K}^+]_{\mathrm{e,init}}), \tag{1.2}$$

where the decay current $j^{\mathrm{K}}_{\mathrm{decay}}$ is defined across the whole domain: $j^{\mathrm{K}}_{\mathrm{decay}} : \Omega \times (0, T] \rightarrow \mathbb{R}$ $(\mathrm{mol}/(\mathrm{m}^2\mathrm{s}))$. k_{dec} here denotes the decay factor for the concentration of extracellular potassium $[\mathrm{K}^+]_{\mathrm{e}}$, and $[\mathrm{K}^+]_{\mathrm{e,init}}$ is the initial extracellular potassium concentration.

1.2.3 Membrane Mechanisms

In Table 1.1, we present a summary of membrane mechanisms, derived from the study by Østby et al. 2009 [3]. We modify the transmembrane flux density of the ions j^k_{m} for each ion species k as described in each model configuration.

Table 1.1: Model configurations implemented in the study.

Model configuration	Membrane mechanisms
MC1 (base model)	Na^+, K^+, Cl^- leak channels + Na^+/K^+ pump
MC2	MC1 + cotransporter KCC1
MC3	MC1 + cotransporter NBC
MC4	MC1 + cotransporter NKCC1
MC5	MC1 + cotransporters NBC and NKCC1

For all the parameters in the following sections, we refer to Table 1.2 in Section 1.2.4.

1.2.3.1 Model Configuration 1

Model configuration 1 (MC1) models the transport of water by osmosis across the membrane, as well as hydrostatic pressure gradients. We also adopt the mechanisms of the ionic transport, such as a Na^+ leak channel, a Cl^- leak channel, a K^+ leak channel, and a Na^+/K^+ pump. The membrane flux densities (mol/(m^2s)) are given by:

$$j_{\mathrm{m}}^{\mathrm{Na}} = \frac{g_{\mathrm{Na}}}{F z_{\mathrm{Na}}}(\phi_{\mathrm{m}} - E_{\mathrm{Na}}) + 3j_{\mathrm{pump}}, \tag{1.3}$$

$$j_{\mathrm{m}}^{\mathrm{K}} = \frac{g_{\mathrm{K}}}{F z_{\mathrm{K}}}(\phi_{\mathrm{m}} - E_{\mathrm{K}}) - 2j_{\mathrm{pump}}, \tag{1.4}$$

$$j_{\mathrm{m}}^{\mathrm{Cl}} = \frac{g_{\mathrm{Cl}}}{F z_{\mathrm{Cl}}}(\phi_{\mathrm{m}} - E_{\mathrm{Cl}}). \tag{1.5}$$

The reversal potentials are given by the Nernst equation:

$$E_k = \frac{\mathrm{RT}}{F z_k} \ln\left(\frac{[\mathrm{k}]_{\mathrm{e}}}{[\mathrm{k}]_{\mathrm{i}}}\right), \tag{1.6}$$

where R is the gas constant, T is the temperature at which we compute the reversal potential and the pump flux density j_{pump} is given by:

$$j_{\mathrm{pump}} = \rho_{\mathrm{pump}}\left(\frac{[\mathrm{Na}^+]_{\mathrm{i}}^{1.5}}{[\mathrm{Na}^+]_{\mathrm{i}}^{1.5} + P_{\mathrm{Na_i}}^{1.5}}\right)\left(\frac{[\mathrm{K}^+]_{\mathrm{e}}}{[\mathrm{K}^+]_{\mathrm{e}} + P_{\mathrm{K_e}}}\right), \tag{1.7}$$

where ρ_{pump} is the maximum pump rate, $P_{\mathrm{Na_i}}$ is the $[\mathrm{Na}^+]_{\mathrm{i}}$ threshold and $P_{\mathrm{K_e}}$ is the $[\mathrm{K}^+]_{\mathrm{e}}$ threshold.

1.2.3.2 Model Configuration 2

Model configuration 2 (MC2) is a derivation of MC1, with an additional cotransporter KCC1 responsible for the transport of K^+ and Cl^- both inward and outward across the neuronal membrane. We implement the cotransporter by modifying equations (1.4) and (1.5) by adding a term describing the flux of K^+ and Cl^- ions through the cotransporter given as

$$J_{\mathrm{KCC1}} = \frac{g_{\mathrm{KCC1}}}{F}\frac{\mathrm{RT}}{F}\ln\left(\frac{[\mathrm{K}^+]_{\mathrm{e}}[\mathrm{Cl}^-]_{\mathrm{e}}}{[\mathrm{K}^+]_{\mathrm{i}}[\mathrm{Cl}^-]_{\mathrm{i}}}\right). \tag{1.8}$$

1.2.3.3 Model Configuration 3

Model configuration 3 (MC3) is a derivation of MC1, with an additional cotransporter NBC responsible for the transport of Na^+ and HCO_3^- inward across the neuronal membrane.

We implement the cotransporter by modifying equation (1.3) by adding the term describing the flux of Na^+:

$$J_{\mathrm{NBC}} = \frac{g_{\mathrm{NBC}}}{F z_{\mathrm{NBC}}}(\phi_{\mathrm{m}} - E_{\mathrm{NBC}}), \tag{1.9}$$

and considering a new equation describing the ion flux of HCO_3^-, that is

$$j_{\mathrm{m}}^{\mathrm{HCO}_3^-} = 2J_{\mathrm{NBC}} \tag{1.10}$$

Here, g_{NBC} is the conductance per unit area for the NBC cotransporter. The reversal potential of NBC is

$$E_{\mathrm{NBC}} = \frac{\mathrm{RT}}{z_{\mathrm{NBC}}F} \ln\left(\frac{[\mathrm{Na}^+]_{\mathrm{e}}[\mathrm{HCO}_3^-]_{\mathrm{e}}^2}{[\mathrm{Na}^+]_{\mathrm{i}}[\mathrm{HCO}_3^-]_{\mathrm{i}}^2}\right), \tag{1.11}$$

where z_{NBC} is the effective valence of the NBC cotransporter complex, here taken to be -1, setting $z_{\mathrm{NBC}} = -(n-1) = -1$ where n is the stoichiometry, and adopting $n = 2$.

1.2.3.4 Model Configuration 4

Model configuration 4 (MC4) is a derivation of MC1, with an additional cotransporter NKCC1 responsible for the transport of Na^+, K^+ and Cl^-. We implement the cotransporter by modifying equations (1.3) and (1.4) by adding a term that describes the flux of Na^+ and K^+ ions, given as

$$J_{\mathrm{NKCC1}} = \frac{g_{\mathrm{NKCC1}}}{F}\frac{\mathrm{RT}}{F} \ln\left(\frac{[\mathrm{Na}^+]_{\mathrm{e}}[\mathrm{K}^+]_{\mathrm{e}}}{[\mathrm{Na}^+]_{\mathrm{i}}[\mathrm{K}^+]_{\mathrm{i}}}\left(\frac{[\mathrm{Cl}^-]_{\mathrm{e}}}{[\mathrm{Cl}^-]_{\mathrm{i}}}\right)^2\right). \tag{1.12}$$

We also modify equation (1.5) by adding (1.12) multiplied by a factor of two to describe the flux of two Cl^- ions. Here, g_{NKCC1} is the conductance per unit area for the NKCC1 cotransporter.

1.2.3.5 Model Configuration 5

Model configuration 5 (MC5) is a derivation of MC1 with two additional cotransporters, NBC and NKCC1, responsible for transport Na^+, K^+, Cl^- and HCO_3^- inward across the neuronal membrane. We implement MC5 by modifying equations (1.3), (1.4) and (1.5) by adding the two terms describing the flux of Na^+, K^+ and Cl^-, given as (1.12) and considering new equations describing the ions flux of HCO_3^- as in equations (1.10).

1.2.4 Model Implementation

1.2.4.1 Boundary Conditions

The boundary conditions incorporated into the model have been adopted from Sætra et al. 2023 [2]. This includes sealed-end boundary conditions to ensure that no ions or fluids are entering of leaving the system on the boundary Γ:

$$\alpha_r j_r^k \cdot n_\Gamma = 0 \qquad \text{on} \quad \Gamma, \tag{1.13}$$

$$\alpha_r u_r \cdot n_\Gamma = 0 \qquad \text{on} \quad \Gamma, \tag{1.14}$$

where n_Γ is the outward pointing normal vector.
We constraint the electrical potential by requiring that

$$\int_\Omega \phi_e \, dx = 0, \tag{1.15}$$

where ϕ_o is the extracellular electric potential. To enforce this zero-average constraint, we introduce an additional unknown Lagrange multiplier c_e, as described by Sætra et al. 2023 in Section 4.7. Following the same set up as in [2] for the extracellular hydrostatic pressure p_e, we set

$$p_o = 0 \quad \text{on} \quad \Gamma_{\text{right}}. \tag{1.16}$$

1.2.4.2 Initial Conditions

We first set a collection of pre-established initial values from empirical measurements of ion concentrations as shown in Table 1.2 and Table 1.3. We then calibrated the models by running simulations for 10^4 s, with $N = 400$ and $\Delta t = 10^{-2}$, setting the transmembrane water permeability η_m to zero. Values of the intracellular and extracellular ion concentrations from the final timestep were then used as initial conditions throughout the paper. When running the simulations with stimulus, we set the water permeability to a nonzero value from Table 1.2, and change the time step from $\Delta t = 10^{-2}$ to $\Delta t = 10^{-3}$ for a total simulation time of 60 s.

1.2.4.3 Model Parameters

We implement the model parameters shown in Table 1.2.

Table 1.2: Model parameters.

Symbol	Definition	Value	Ref.
L	Length of domain	$3.0 \cdot 10^{-4}$ m	[2]
F	Faraday's constant	96485.3 C/mol	
R	Gas constant	8.314 J/(molK)	
T	Temperature	300 K	
D_{Na}	Na^+ diffusion constant	$1.33 \cdot 10^{-9}$ m^2/s	[2]
D_{K}	K^+ diffusion constant	$1.96 \cdot 10^{-9}$ m^2/s	[2]
D_{Cl}	Cl^- diffusion constant	$2.03 \cdot 10^{-9}$ m^2/s	[2]
D_{HCO3}	HCO_3^- diffusion constant	$1.09 \cdot 10^{-9}$ m^2/s	[3]
z_{Na}	Na^+ valence	1	
z_{K}	K^+ valence	1	
z_{Cl}	Cl^- valence	-1	
$z_{\mathrm{HCO_3^-}}$	HCO_3^- valence	-1	
z_{NBC}	NBC cotransporter valence	-1	
g_{Na}	Membrane conductance for Na^+	1 S/m^2	[2]
g_{K}	Membrane conductance for K^+	16.96 S/m^2	[5]
g_{Cl}	Membrane conductance for Cl^-	1 S/m^2	[2]
g_{NKCC1}	Membrane conductance for g_{NKCC1}	$2 \cdot 10^{-2}$ S/m^2	[3]
g_{KCC1}	Membrane conductance for g_{KCC1}	$7 \cdot 10^{-1}$ S/m^2	[3]
g_{NBC}	Membrane conductance for g_{NBC}	$8 \cdot 10^{-1}$ S/m^2	[3]
ρ_{pump}	Maximum pump rate	$1.12 \cdot 10^{-6}$ mol/(m^{2}s)	[2]
$P_{\mathrm{Na_i}}$	$[Na^+]_i$ threshold for Na^+/K^+ pump	10 mol/ m^3	[2]
$P_{\mathrm{K_e}}$	$[K^+]_e$ threshold for Na^+/K^+ pump	1.5 mol/ m^3	[2]
j_{in}	Constant input flux density	$9.05 \cdot 10^{-7}$ mol/(m^{2}s)	
k_{dec}	Decay factor for $[K^+]_e$	$2.9 \cdot 10^{-8}$ m/s	[2]

The implemented code is openly available at
https://github.com/hittheant/Simula_Summer_Project_1.

1.3 Results

1.3.1 Calibration

We calibrate the system as described in the Methods section. Figure 1.2 illustrates the temporal and spatial dynamics of the system after calibrating the model and running the simulation for 30 s without stimulus for base model MC1.

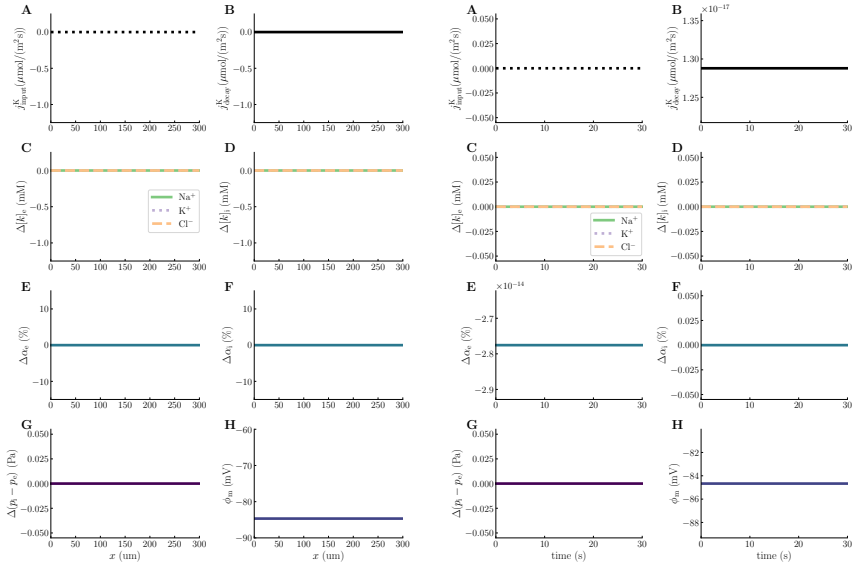

Fig. 1.2: Post-calibration dynamics of the system with model configuration 1 (MC1) without stimulus. For this simulation, the water permeability was set to zero. Left two columns: Spatial dynamics post-calibration, measured at the end of the simulation (t = 30 s). Right two columns: Time evolution measured at L = $1.50 \cdot 10^{-4}$ m.

We expect the ionic concentrations to remain constant in time and space when no stimulus is applied, which is what we observe for MC1 (Figure 1.2 C-D). We anticipate that our system will demonstrate the same behaviour in space and time for other physical quantities, such as variations in the transmembrane hydrostatic pressure difference (Figure 1.2 G), membrane potential (Figure 1.2 H) and compartmental volume fractions (Figure 1.2 E-F). The expected result is the same for all model setups; however, we only demonstrate the results for MC1 since the other model configurations appear to behave the same after calibration.

The post-calibrated ion concentrations are summarised in Table 1.3 for each model configuration. We observe that the ionic concentrations of the different species do not vary drastically between the different models. The largest difference appears between MC2 and MC5, where we see that MC5 has the lowest intracellular Na^+ concentration of 14.873 mM, and MC2 has the highest intracellular Na^+ concentration of 16.017 mM. We observe a similar pattern between all ionic species in these two model configurations, where MC2 has the highest intracellular concentration of all ions and MC5 has the lowest. We also note that MC3 and MC4 have almost identical baseline concentrations for all ions, with the exception of small differences of 0.001 mM between the intracellular K^+ concentration and the extracellular Na^+ and K^+ concentrations.

Table 1.3: Ionic concentrations after calibration for different model scenarios. Empirical concentrations are taken from [5] and [6] and were used as initial values for the model pre-calibration.

	$[Na^+]_i$ (mM)	$[K^+]_i$ (mM)	$[Cl^-]_i$ (mM)	$[HCO_3^+]_i$ (mM)	$[Na^+]_e$ (mM)	$[K^+]_e$ (mM)	$[Cl^-]_e$ (mM)	$[HCO_3^+]_e$ (mM)
Empirical	15.189	99.959	5.145	11.300	144.662	3.082	133.71	15.000
MC1	15.510	99.190	5.064		146.580	3.019	133.872	
MC2	16.017	101.812	8.178		140.498	2.844	127.644	
MC3	15.510	99.189	5.064	8.416	146.581	3.020	133.872	14.069
MC4	15.510	99.190	5.064		146.580	3.019	133.872	
MC5	14.873	98.520	3.691	8.526	149.173	3.040	136.618	13.848

The membrane potentials are also very similar for all models with $\phi_m = -85$ mV, with the exception of MC2, where $\phi_m = -86$ mV (Table 1.4). We also observe the same deviation for MC2 and MC5 as before, with different j_{pump} values compared to the rest of the configurations. Specifically, for MC2, the j_{pump} value is 0.491 mol/m^{2}s, while MC5 has the lowest j_{pump} value of 0.483 mol/m^{2}s. Generally, the membrane potential ϕ_m, pump flux j_{pump}, and reversal potentials for each ionic species appear to remain within a similar range (Table 1.4). We also see on Table 1.4 that the reversal potential of Cl^- varies widely across the different models, with the highest and lowest E_{Cl} values 22mV apart.

Table 1.4: Physical quantities after calibration for different model scenarios.

	ϕ_m (mV)	j_{pump} (mol/m^{2}s)	E_{Na} (mV)	E_K (mV)	E_{Cl} (mV)
MC1	-85	0.493	-58	90	85
MC2	-86	0.491	-56	92	71
MC3	-85	0.493	-58	90	85
MC4	-85	0.493	-58	90	85
MC5	-85	0.483	-60	90	93

1.3.2 Stimulus Dynamics

We show the results of our simulation with a stimulus for each model configuration (MC1-MC5) in Figures 1.3 and 1.4. These figures show the temporal and spatial changes, respectively, in ionic concentrations in the ICS and ECS. We also present the time evolution of the changes in the volume fractions of the ICS and ECS in Figure 1.5, subfigures a and b, respectively.

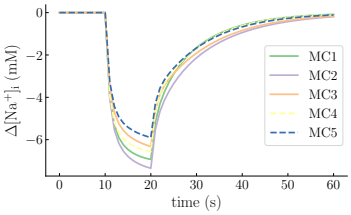

(a) Change in Na^+ concentration in the ICS.

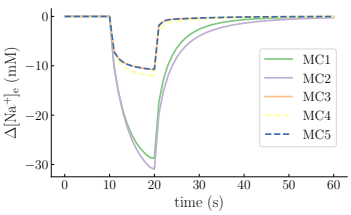

(b) Change in Na^+ concentration in the ECS.

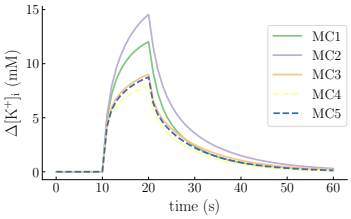

(c) Change in K^+ concentration in the ICS.

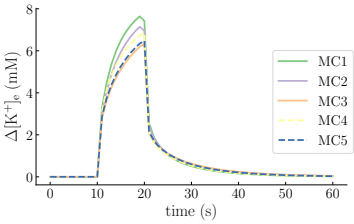

(d) Change in K^+ concentration in the ECS.

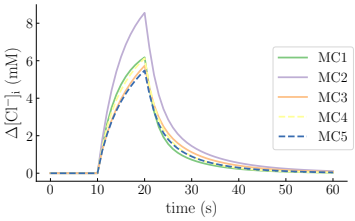

(e) Change in Cl^- concentration in the ICS.

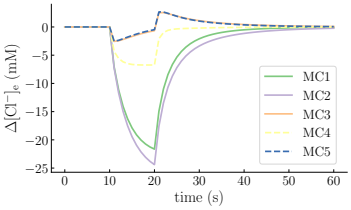

(f) Change in Cl^- concentration in the ECS.

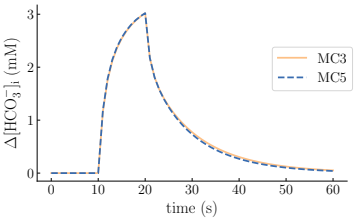

(g) Change in HCO_3^- concentration in the ICS.

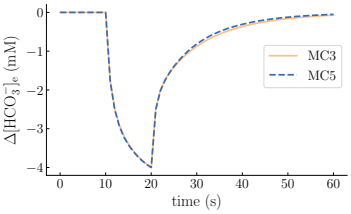

(h) Change in HCO_3^- concentration in the ECS.

Fig. 1.3: Temporal dynamics in changes in ionic concentrations in ICS and ECS for different model configurations (MC1-MC5). The system is simulated for 60 s, with stimulation activated between [10 s, 20 s]. We measure the system at L = $1.50{\cdot}10^{-4}$ m. The change in HCO_3^- concentration is only shown for MC3 and MC5.

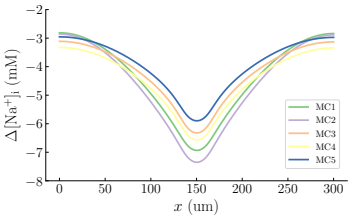

(a) Change in Na^+ concentration in the ICS.

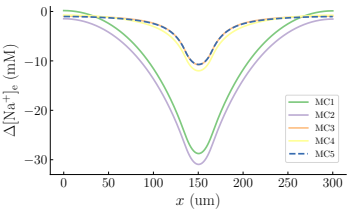

(b) Change in Na^+ concentration in the ECS.

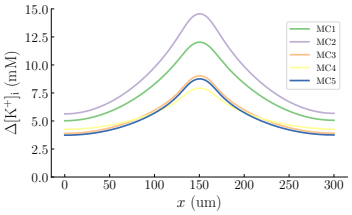

(c) Change in K^+ concentration in the ICS.

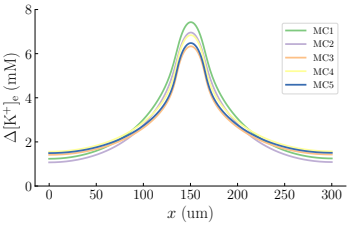

(d) Change in K^+ concentration in the ECS.

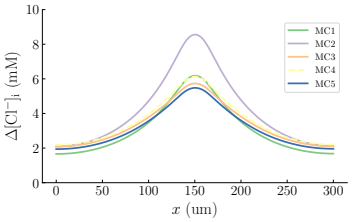

(e) Change in Cl^- concentration in the ICS.

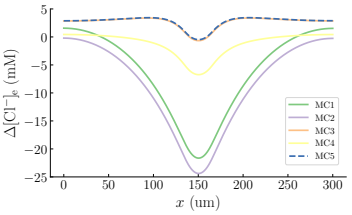

(f) Change in Cl^- concentration in the ECS.

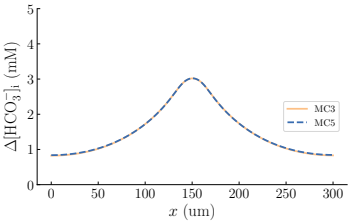

(g) Change in HCO_3^- concentration in the ICS.

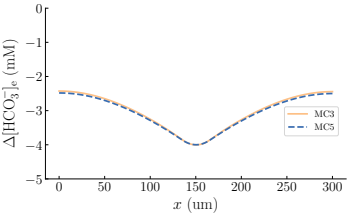

(h) Change in HCO_3^- concentration in the ECS.

Fig. 1.4: Spatial profiles of the change in ionic concentrations in ICS and ECS for different model configurations (MC1-MC5). The system is simulated for 60 s, with stimulation activated between [10 s, 20 s]. We measure the system at the end of the stimulation, t = 20 s. The change in HCO_3^- concentration is only shown for MC3 and MC5.

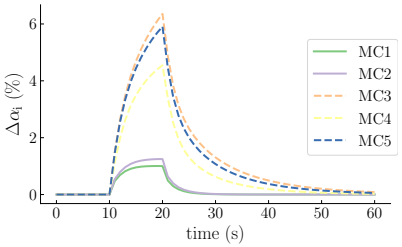

(a) Time evolution of the change in ICS volume fraction with stimulus, measured at L = $1.50 \cdot 10^{-4}$ m.

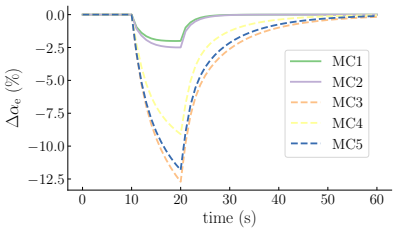

(b) Time evolution of the change in ECS volume fraction with stimulus, measured at L = $1.50 \cdot 10^{-4}$ m.

Fig. 1.5: Changes in volume fraction α_r as a function of time in ICS and ECS for all model configurations (MC1-MC5).

We anticipate that the ionic concentrations in the compartments will remain constant until the stimulus is applied. This is seen in Figure 1.3 for all model configurations. For example, in subfigure a, we can observe that the intracellular Na^+ concentration remains the same until the stimulus begins in all model configurations. We can observe that the behaviour of MC3 and MC5 are very similar throughout the temporal evolution of all ionic species (Figure 1.3, subfigures a - h). The increase of $[K^+]_e$ and $[K^+]_i$ can be seen most prominently in MC1 and MC2, and we see a similar effect of stimulation on these models in terms of extracellular and intracellular $[Na^+]$. MC4 has the lowest magnitude change in $[Cl^-]_e$ among the models that do not simulate HCO_3^- dynamics (MC1, MC2 and MC4). The model configurations that contain the NBC cotransporter for HCO_3^- (MC3 and MC5) show a much lower influx of Cl^-.

In terms of spatial dynamics, we can see in Figure 1.4 that the behaviour of models MC3, MC4 and MC5 is similar for all ions concentrations in ICS and ECS, except for extracellular Cl^- concentration as shown in subfigure f.

In both subfigures a and b, the volume fraction remains constant before applying the stimulus, as expected. After the stimulus was applied, we can see an increase in the volume fraction in the intracellular space and a decrease in the extracellular space. In fact, in response to ionic changes, the volume of the intracellular compartment increases by more than 6% for MC3 and MC5. The two model configurations where we can see the smallest increase are MC1 and MC2. Conversely, in response to the ionic changes, the volume of the extracellular compartment decreases to 12.5% for MC3 and MC5. As before, the model configurations where we see the smallest decrease are MC1 and MC2.

The total intracellular and extracellular volume-weighted fluid velocities as observed at the end of stimulation (at t = 20 s) are shown in Figure 1.6, subfigures a and b, respectively. All fluid velocities are multiplied by the volume fraction of each compartment to obtain a volume-weighted result. The maximal ICS volume-weighted fluid velocities for all model configurations are also summarised in Table 1.5. Here, we see that MC1 and MC2 have similarly low maximum water velocities

in ICS, while MC3, MC4 and MC5 have similarly high maximum values (with MC3 and MC5 having the maximum ICS water velocity of 16 μm/min). We also note that MC3 and MC5 have almost identical fluid velocity plots. All models show fluid flowing in the same direction; positive intracellular fluid velocities for $x > 150$ μm and negative intracellular fluid velocities for $x < 150$ μm and vice versa in the case of extracellular velocities.

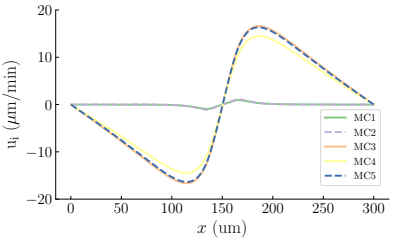

(a) Spatial profiles of the total volume-weighted fluid velocity in the ICS, measured at the end of the stimulus (t = 20 s).

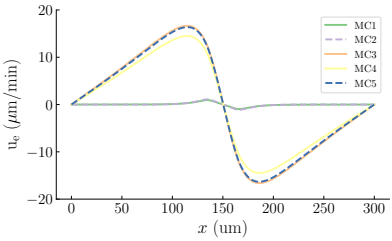

(b) Spatial profiles of the total volume-weighted fluid velocity in the ECS, measured at the end of the stimulus (t = 20 s).

Fig. 1.6: Spatial profile of the total volume-weighted fluid velocity in the ICS and ECS for all model configurations (MC1-MC5).

Table 1.5: Maximal total compartmental volume-weighted fluid velocities for different model configurations (MC1-MC5) during neuronal stimulus measured at the end of the stimulation (t = 20 s).

	$u_{i,\,max}$ (μm/min)
MC1	0.96
MC2	1.1
MC3	16
MC4	14
MC5	16

We also present the osmotic and hydrostatic components of the ICS fluid velocity for MC1 and MC3 in Figure 1.7. When comparing the osmotic and hydrostatic components of the ICS fluid velocity between the model with the highest maximum velocity, MC3, and the model with the lowest maximum velocity, MC1, we see that the higher total ICS velocity in MC3 is due to the ratio of the osmotic contribution to the hydrostatic contribution.

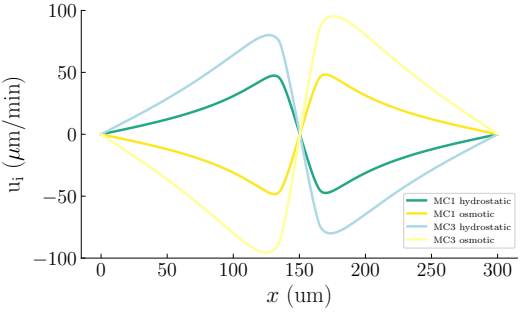

Fig. 1.7: Comparing the volume-weighted osmotic and hydrostatic components of intracellular fluid velocity for MC1 and MC3.

1.4 Discussion

We have expanded on a previous computational model for predicting ionic electrodiffusion and fluid dynamics in brain tissue by adding glial KCC1, NBC and NKCC1 cotransporters. Further, we assess how the various cotransporters affect characteristics such as the energy required to maintain equilibrium, spatial and temporal dynamics of ions, and water velocities during neuronal activity. Our findings show that with no stimulus, MC5 has a lower Na^+/K^+ pump flux value than the other models, from which we can infer that the astrocyte expends less energy with this configuration of membrane mechanisms. When the stimulus is applied, MC1, MC2 and MC4 showed the most similarity for all the ion concentration dynamics. We also found that MC3 has the highest total intracellular of 16 μm/s.

1.4.1 Calibration and Zero Stimulus Dynamics

When there is no stimulus, we found very similar steady state ion concentration values across our model configurations, with the exception of intracellular and extracellular Cl^- concentrations (with $[Cl^-]_e$ and $[Cl^-]_i$ for MC2 the biggest deviation: not significant, $p > 0.05$). The Na^+/K^+ pump is the only ionic transport mechanism in our model that requires chemical energy to move ions against concentration gradients. Therefore, we were interested in seeing whether the flux through the Na^+/K^+ pump (j_{pump}) would have different values at equilibrium for the different configurations of the model. We see from Table 1.4 that MC5 has a significantly ($p < 0.05$) lower pump flux value than the other models. As MC5 has both the NBC and NKCC1 cotransporters, this low pump flux can be attributed to their net action in equilibrium. The flux values for MC1, MC3, and MC4 are identical to three significant figures, while MC5 has the lowest flux value. This is interesting as MC5

has both cotransporters, NBC and NKCC1, and needs the least energy to maintain equilibrium due to its low pump flux value.

1.4.2 Stimulus Dynamics

Focusing on the temporal Na^+/K^+ dynamics in Figure 1.3, we can see that there is a decrease in the ionic concentration of Na^+ in the extracellular space due to the efflux of sodium ions due to the neuronal activities represented by the stimulus. The decrease in $[Na^+]_i$ as shown in Figure a is due to the shrinkage of the extracellular space (and thereby the expansion of the astrocytic volume) resulting in a lower concentration of Na^+ (in spite of the influx of Na^+ ions (as $[Na^+]_e > [Na^+]_i$ during stimulation).

Neuronal stimulation results in an increase of $[K^+]_i$ at a greater rate than the decrease in $[Na^+]_i$. This creates an outward electrostatic gradient. To balance this gradient, we see an inward flux of Cl^- ions in all the model configurations. This behaviour is different in MC3 and MC5, where we see an exponential decrease in $[Cl^-]_e$ (subfigure f) as in the other models followed by a linear increase for the remaining period of stimulation and an exponential increase at the end of the constant stimulus period above the baseline concentration before decaying back to its equilibrium. We believe that this is due to the dynamics of HCO_3^- (subfigures h and g), which sees an exponential influx, in a sense playing the role of Cl^- as seen by the other model. Therefore, since Cl^- has an outward flux from the astrocytic membrane during stimulation, the intracellular concentration of HCO_3^- continues to increase exponentially throughout stimulation. Analysing subfigures g and h, intracellular and extracellular HCO_3^- concentrations are quite similar in both MC3 and MC5. This means that the NKCC1 cotransporter does not influence the spatial dynamics in the changes in HCO_3^- concentrations.

The magnitude of the osmotic and hydrostatic flows in the ICS for MC1 are nearly equal and in opposite directions, as seen in Figure 1.7. However, this is not the case for MC3, where the osmotic flow is more powerful than the hydrostatic, leading to a higher net water velocity. The osmotic water velocity depends on the immobile ions. As we see similarly high net fluid flows for MC3, MC4, and MC5 compared to MC1 and MC2, we believe that the cotransporters involving Na^+ ions could be one of the common factors among the former group that causes this. The presence of HCO_3^- ions and its effect on the valency and number of immobile ions could lead to increased osmotic flow. This could explain the higher total water velocities observed in MC3 and MC5, as demonstrated in Table 1.5.

We opted to adjust the initial concentrations of the ions to obtain new steady states for our model configurations, while empirically setting the membrane conductance for each ion channel. This was a deliberate choice, and one could instead make the case for setting the concentrations empirically and adjusting the membrane conductivity to reach equilibrium (as done by Østby et al. 2009 [3]).

Although the comparison between each of our model configurations is useful, validation with empirical data could provide more biologically relevant information. While we are able to determine the effect of different mechanisms and their effect on shrinkage, a future goal is to compare these results with in vivo experiments and measurements of volume changes along with knockout experiments to identify the contribution of each membrane mechanism to determine the validity of our model. Future objectives to extend this model include incorporating additional membrane processes found in astrocytes, such as active water transport through the NKCC1 channel and the inward rectifying K^+ current described in [2].

1.5 Conclusion

In conclusion, our research underscores the role of astrocyte networks and glial cotransporters in the regulation of brain volume and waste clearance. Through our computational model within the Kirchhoff-Nernst-Planck electrodiffusive framework, we have identified the NBC cotransporter as a key player, exhibiting the highest fluid velocities. These findings highlight the implications of targeting glial cotransporters to modulate brain volume homeostasis and waste clearance, offering new directions for neuroscience research.

References

1. Sara Mederos, Candela González-Arias, and Gertrudis Perea. Astrocyte–Neuron Networks: A Multilane Highway of Signaling for Homeostatic Brain Function. Frontiers in Synaptic Neuroscience, 10, 2018.
2. Marte J. Sætra, Ada Johanne Ellingsrud, and Marie E. Rognes. Neural activity induces strongly coupled electro-chemo-mechanical interactions and fluid flow in astrocyte networks and extracellular space – a computational study. PLoS Computational Biology, 19:e1010996, 07/2023 2023.
3. Ivar Østby, Leiv Øyehaug, Gaute T. Einevoll, Erlend A. Nagelhus, Erik Plahte, Thomas Zeuthen, Catherine M. Lloyd, Ole P. Ottersen, and Stig W. Omholt. Astrocytic Mechanisms Explaining Neural-Activity-Induced Shrinkage of Extraneuronal Space. PLOS Computational Biology, 5(1):e1000272, January 2009. Publisher: Public Library of Science.
4. Byung-Ju Jin, Hua Zhang, Devin K. Binder, and A. S. Verkman. Aquaporin-4-dependent K(+) and water transport modeled in brain extracellular space following neuroexcitation. The Journal of General Physiology, 141(1):119–132, January 2013.
5. G Halnes, I Østby, KH Pettersen, SW Omholt, and GT Einevoll. Electrodiffusive model for astrocytic and neuronal ion concentration dynamics. PLoS Comput Biol., 2013.
6. C. K. Tong and M. Chesler. Modulation of spreading depression by changes in extracellular ph. Journal of Neurophysiology, 84(5):2449–2457, 2000. PMID: 11067987.

Chapter 2
Computational Modeling of Ephaptic coupling in Myelinated and Unmyelinated Axon Bundles Using the EMI Framework

Alessandro Gatti, Ramón Nartallo-Kaluarachchi, Abhinav Uppal, and Pietro Benedusi

Abstract This report examines the Extracellular-Membrane-Intracellular (EMI) framework for modeling action potentials along 3D axons. We investigate the effect of myelination and the potential for ephaptic coupling in this model. Additionally, we assess the convergence and stability of a range of Runge-Kutta time-stepping algorithms on simple geometries with manufactured solutions. We first analyze single axons and the influence of myelin on the speed of action potentials. Then, we use a 3D geometry of nine cylinders to represent an axonal bundle and study the induced potential in the central axon in both myelinated and unmyelinated cases. Finally, we discuss the biological implications of ephaptic coupling and the importance of 3D modeling for precise simulations of spiking neurons.

2.1 Introduction

Hodgkin and Huxley's 1952 work [1] was a pioneering effort to quantitatively describe the chemical processes that cause excitatory neurons to fire. Since then, a variety of alternative models, such as FitzHugh-Nagumo [2] and Hindmarsh-Rose [3] ODE models, have been developed to model excitable cells. The emergence of neural networks has further led to the modeling of neurons as single points in

Alessandro Gatti
Department of Mathematics, University of Trento, IT

Ramón Nartallo-Kaluarachchi
Mathematical Institute, University of Oxford, UK

Abhinav Uppal
Department of Bioengineering, University of California San Diego, USA

Pietro Benedusi (corresponding author)
Department of Numerical Analysis and Scientific Computing, Simula Research Laboratory, NO
e-mail: benedp@simula.no

K. J. McCabe (ed.), *Computational Physiology*, Simula SpringerBriefs on Computing 17,
https://doi.org/10.1007/978-3-031-53145-3_2

space with only time-dependent dynamics. In this report, we explore two biological scenarios in which spatial and temporal dynamics are necessary to accurately model the propagation and induction of action potentials. Specifically, we investigate the effects of myelination [4] and ephaptic coupling in axonal bundles [5]. To do this, we use the recent EMI model to incorporate spatial dynamics into a partial differential equation (PDE) framework [6].

2.1.1 Myelination

The myelin sheath is an extended and modified plasma membrane that is wrapped around the nerve axon in a spiral pattern [7]. It is derived from and is part of Schwann cells in the peripheral nervous system (PNS) and oligodendroglial cells in the central nervous system (CNS). Each myelin-generating cell provides myelin for only one segment of the axon. The nodes of Ranvier, which are short portions of the axon left uncovered, are essential for the functioning of myelin. This myelin sheath increases the resistance of the axonal membrane, lengthening its electrical space constant, and thus facilitating signal transmission along the axon. Additionally, myelin decreases the capacitance of the axonal membrane, so that less charge (in the form of Na^+) is required to depolarize the cell. Both of these effects increase the speed of action potential propagation.

2.1.2 Ephaptic Coupling

The term *ephapse* was proposed in 1941 by Arvanitaki [8] to describe neural structures coming into contact or in close proximity, without coupling via anatomically differentiated synapses. Where Arvanitaki had been studying an experimental preparation with two giant axons (from *Sepia officinalis*) forming an ephapse by making the axons touch (for 5 mm in 4 to 5 cm long axons), the term ephaptic coupling has since come to describe short-range coupling between non-contiguous neuronal membranes [9], alternatively described as 'electric field effects' [10].

Similarly to how spiking individual neurons can give rise to extracellular action potentials, network-level activity can alter the local electric environment in nervous tissue. This spatiotemporal variation in extracellular potential and its gradient electric field feed back into the same network, inducing ephaptic coupling [5]. This electric ephaptic coupling can be contrasted with ionic ephaptic coupling, where local changes in extracellular ion concentrations can alter Nernst potentials [11].

Although ephaptic coupling between neurons can be considered a weak effect compared to chemical or electrical synapses (measurements of endogenous electric fields are on the order of a few mV/mm, see [12] for a summary of experimental data), it can still have network-level implications in healthy and pathological nervous tissue [10]. For instance, weak electric fields can entrain slow neocortical oscillations

[13]. Additionally, mathematical models of ephaptic coupling in axon bundles show induced synchronization of firing activity [14] and modulation of transmission delays [15].

In pathological scenarios, ephaptic entrainment has been implicated in neurodegenerative disease models considering damaged neurons [16]. Ephaptic coupling is also hypothesized to play a role in pathologies resulting from demyelination of cranial nerves under compression, such as trigeminal neuralgia (facial pain) through the fifth cranial nerve [17] and vestibular paroxysmia (short episodic vertigo) from the eighth cranial nerve ([18], [19]).

Thus, studying ephaptic coupling can improve our understanding of network-level feedback under healthy and pathological conditions. Modeling studies of ephaptic coupling also offer the translational benefit of providing an evaluation framework in the design of exogenous (transcranial) stimulation protocols [12]. Given the key role of extracellular potentials in ephaptic coupling, here we extend previous work on modeling axon bundles using the EMI framework [11] by contrasting unmyelinated and myelinated axons in a bundle.

2.2 Methods

2.2.1 The EMI Model

The EMI model is a PDE framework that has recently been developed to simulate excitable cells, such as neurons and cardiac cells, from the first principles [6]. It divides the extracellular space, the cell membrane, and the intracellular space into distinct components. When both spatial and temporal dynamics are taken into account, it is suitable for modeling the effects of myelination and ephaptic coupling.

For a single cell, denoted Ω_i, surrounded by an extracellular domain, Ω_e, the EMI model is given by the following coupled PDE-ODE,

$$\begin{aligned}
\nabla \cdot \sigma_i \nabla u_i &= f, && \text{in} \quad \Omega_i, \\
\nabla \cdot \sigma_e \nabla u_e &= g, && \text{in} \quad \Omega_e, \\
\sigma_e \nabla u_e \cdot \mathbf{n}_e &= -\sigma_i \nabla u_i \cdot \mathbf{n}_i \equiv I_m, && \text{at} \quad \Gamma, \\
v &= u_i - u_e, && \text{at} \quad \Gamma, \\
\frac{\partial v}{\partial t} &= \frac{1}{C_m}(I_m - I_{ion}), && \text{at} \quad \Gamma,
\end{aligned} \tag{2.1}$$

where u_i, u_e, and v are intracellular, extracellular, and membrane potentials, respectively, which are commonly given in mV. Furthermore, σ_i and σ_e are intracellular and extracellular conductances, respectively (typically in mS/cm), C_m is the membrane capacitance (typically in $\mu F/cm^2$), and Γ denotes the cell membrane. $\mathbf{n_i}$ and $\mathbf{n_e}$ represent the outward-pointing normal vectors. The ionic currents through channels,

pumps, and exchangers at the membrane are denoted by I_{ion} and are typically given in $\mu A/cm^2$. A schematic representation of the model domain is given in Fig. 2.1.

We assumed that the external boundary $\partial\Omega_e$ is insulated, which leads to the following Neumann boundary condition

$$\sigma_e \nabla u_e \cdot \mathbf{n}_e = 0, \qquad \text{at} \quad \partial\Omega_e. \tag{2.2}$$

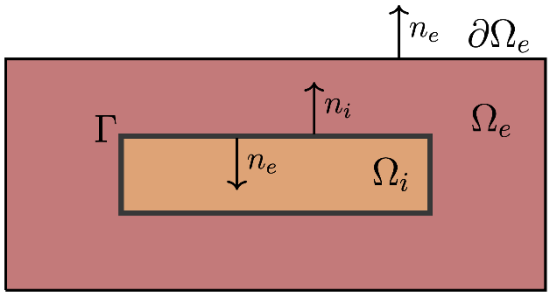

Fig. 2.1: Illustration of an EMI model domain consisting of an extracellular domain, Ω_e, a cell membrane, Γ, and an intracellular domain, Ω_i. $\mathbf{n_e}, \mathbf{n_i}$ represent normal vectors and $\partial\Omega_e$ represents the boundary of the extracellular space.

2.2.2 Numerical Methods

2.2.2.1 Multi-Dimensional Primal Formulation of the EMI Model

In order to numerically integrate the EMI model, we derive a weak formulation [6]. In particular, we use the multi-dimensional primal formulation which is expressed as follows: find $u_i \in V_i = H^1(\Omega_i)$, $u_e \in V_e = H^1(\Omega_e)$, $I_m \in Q^* = H^{-1/2}(\Gamma)$ such that

$$\begin{aligned}
\int_{\Omega_i} \sigma_i \nabla u_i \cdot \nabla v_i dx - \int_\Gamma I_m v_i ds &= \int_{\Omega_i} f v_i dx, \\
\int_{\Omega_e} \sigma_e \nabla u_e \cdot \nabla v_e dx - \int_\Gamma I_m v_e ds &= \int_{\Omega_i} g v_e dx, \\
\int_\Gamma -u_e j_m ds + \int_\Gamma u_i j_m ds - \int_\Gamma \Delta t C_m^{-1} I_m j_m ds &= \int_\Gamma h j_m ds,
\end{aligned} \tag{2.3}$$

for all the test functions $v_i \in V_i$, $v_e \in V_e$ and $j_m \in Q^*$ [6]. In this formulation, the time-dependent equations are discretized according to an implicit Euler scheme. The

known right-hand side h combines the previous transmembrane potential solution, v_0, and the evaluation of the ionic current, I_{ion}, into $h \equiv v_0 - C_m^{-1}\Delta t I_{ion}$. However, as discussed in the following section, this final equation can be modified according to any time discretization.

2.2.2.2 Runge-Kutta Time-Stepping in the EMI Model

As discussed above, the derivation of the weak formulation requires a choice of time discretization. Depending on the choice of the time-stepping algorithm, the final equation will differ. We consider the well-studied Runge-Kutta (RK) methods, a family of classical ODE integrators [20]. For a homogeneous differential equation of the form

$$\frac{dy}{dt} = f(y(t)), \tag{2.4}$$

an s-order RK scheme is a one-step method of the following form,

$$y_{n+1} = y_n + h\sum_{i=1}^{s} b_i k_i, \tag{2.5}$$

where,

$$k_1 = f(y_n), \tag{2.6}$$

$$\vdots$$

$$k_s = f(y_n + h\sum_{j=1}^{s} a_{ij}k_j). \tag{2.7}$$

Thus, the method is uniquely defined by the matrix vector pair $\boldsymbol{A}, \boldsymbol{b}$, where $\boldsymbol{A} = (a_{ij})$ and $\boldsymbol{b} = (b_1, ..., b_s)$. We can also define the vector $\boldsymbol{k} = (k_1, ..., k_2)$. To make this method consistent with the order s, certain conditions on $\boldsymbol{A}, \boldsymbol{b}$ must be satisfied, limiting the number of RK methods for each given order. When $\boldsymbol{A}$ is lower triangular with zero diagonal, the method is explicit; otherwise, it is implicit. We investigate the form of final EMI equation for a generalized RK scheme for both the passive and Hodgkin-Huxley conductance dynamics.

2.2.2.3 The Passive Conductance EMI Model

We consider the time-dependent equation from the EMI model with passive conductance, corresponding to $I_{ion}(v) = v$ [6],

$$\frac{dv}{dt} = \frac{1}{C_m}\left(I_m - v(t)\right). \tag{2.8}$$

Considering an RK method of order s, we discretise this equation as,

$$v_{t+1} = v_t + h\sum_{i=1}^{s} b_i k_i, \tag{2.9}$$

$$= v_t + h\boldsymbol{b}^\top \boldsymbol{k}. \tag{2.10}$$

We further notice that

$$k_i = \frac{1}{C_m}(I_m - v_t - h\sum_{j=1}^{s} a_{ij}k_j), \tag{2.11}$$

which we write in vector notation as,

$$\boldsymbol{k} = \frac{1}{C_m}(I_m - v_t)\boldsymbol{u} - h\boldsymbol{A}\boldsymbol{k}, \tag{2.12}$$

where $\boldsymbol{u}$ is a s-vector of 1s. Defining $\beta = \frac{h}{C_m}$ and $\boldsymbol{I}$ to be the s-dimensional identity matrix, we assume $\boldsymbol{I} + \beta\boldsymbol{A}$ to be invertible and write $\boldsymbol{k}$ explicitly as

$$\boldsymbol{k} = \frac{1}{C_m}(I_m - v_t)(\boldsymbol{I} + \beta\boldsymbol{A})^{-1}\boldsymbol{u}. \tag{2.13}$$

As such, our RK scheme can be written as

$$v_{t+1} = (1 - \beta\boldsymbol{b}^\top(\boldsymbol{I} + \beta\boldsymbol{A})^{-1}\boldsymbol{u})v_t + \beta\boldsymbol{b}^\top(\boldsymbol{I} + \beta\boldsymbol{A})^{-1}\boldsymbol{u}I_m. \tag{2.14}$$

According to the weak formulation of the EMI model, this yields conservation law,

$$\int_\Gamma u_i\, ds - \int_\Gamma u_e\, ds - \beta\boldsymbol{b}^\top(\boldsymbol{I} + \beta\boldsymbol{A})^{-1}\boldsymbol{u}\int_\Gamma I_m\, ds$$
$$= (1 - \beta\boldsymbol{b}^\top(\boldsymbol{I} + \beta\boldsymbol{A})^{-1}\boldsymbol{u})\int_\Gamma v_t\, ds. \tag{2.15}$$

Given the Butcher tableau, $(\boldsymbol{A}, \boldsymbol{b})$, one can use this formulation to calculate the function,

$$g_{\mathrm{RK}}(\beta) = \beta\boldsymbol{b}^\top(\boldsymbol{I} + \beta\boldsymbol{A})^{-1}\boldsymbol{u}, \tag{2.16}$$

which can then be used to implement any RK scheme on the EMI model. Furthermore, we notice that $g_{\mathrm{RK}}(\beta)$ is related to the well-studied stability function of the RK family, which is defined [20],

$$R(z) = 1 + z\boldsymbol{b}^\top(\boldsymbol{I} - z\boldsymbol{A})^{-1}\boldsymbol{u}, \tag{2.17}$$

namely, the relation is,

$$g_{\mathrm{RK}}(\beta) = 1 - R(-\beta), \tag{2.18}$$

yielding conservation law,

$$\int_\Gamma u_i \, ds - \int_\Gamma u_e \, ds + (R(-\beta) + 1) \int_\Gamma I_m \, ds = R(-\beta) \int_\Gamma v_t \, ds. \tag{2.19}$$

The stability function can be written as

$$R(z) = \frac{\det(\boldsymbol{I} - z\boldsymbol{A} + z\boldsymbol{u}\boldsymbol{b}^\top)}{\det(\boldsymbol{I} - z\boldsymbol{A})}, \tag{2.20}$$

where for explicit scheme, due to their lower triangularity, the denominator is 1. Therefore, for explicit schemes, the stability function R and therefore g_{RK} is a polynomial of degree s, which we denote $p_s(\beta)$ that has form,

$$p_s(\beta) = \sum_{n=1}^{s} (-1)^{n+1} \beta^n \Theta(\boldsymbol{A}, \boldsymbol{b}, n), \tag{2.21}$$

with,

$$\Theta(\boldsymbol{A}, \boldsymbol{b}, n) = \sum_{i_0=n}^{s} b_{i_0} \sum_{i_1=n-1}^{i_0-1} a_{i_0,i_1} \cdots \sum_{i_k=n-k}^{i_{k-1}-1} a_{i_{k-1},i_k} \cdots \sum_{i_{n-1}=n-1}^{i_{n-2}-1} a_{i_{n-2},i_{n-1}}, \tag{2.22}$$

for $n = 2, ..., s$ and extended to $n = 1$ by,

$$\Theta(\boldsymbol{A}, \boldsymbol{b}, 1) = \sum_{i_0=1}^{s} b_{i_0} \tag{2.23}$$

This yields conservation law,

$$\int_\Gamma u_i \, ds - \int_\Gamma u_e \, ds - p_s(\beta) \int_\Gamma I_m \, ds = (1 - p_s(\beta)) \int_\Gamma v_t \, ds. \tag{2.24}$$

Following this process, we can derive the functions g_{RK} associated with a range of explicit and implicit RK schemes. In addition, we note that for explicit RK schemes of order p, we have the following approximation,

$$R(z) = 1 + z + \frac{z^2}{2!} + \frac{z^3}{3!} + ... + \frac{z^p}{p!} + O(z^{p+1}), \tag{2.25}$$

therefore $R(z) = e^z + O(z^{p+1})$. Using this property, we can define the following scheme that approximates any explicit, p-order RK scheme to order p,

Table 2.1: Common Runge-Kutta schemes and the associated functions $g_{\mathrm{RK}}(\beta)$.

Scheme	Abbrev.	Order	Implicit/ Explicit	$g_{\mathrm{RK}}(\beta)$
Explicit Euler	EE	1	E	β
Explicit Midpoint	EMP	2	E	$\beta - \frac{\beta^2}{2}$
Runge-Kutta 4	RK4	4	E	$\beta - \frac{\beta^2}{2} + \frac{1}{6}\beta^3 - \frac{1}{24}\beta^4$
Implicit Euler	IE	1	I	$\frac{\beta}{1+\beta}$
Trapezoidal Rule	TPR	2	I	$\frac{\beta}{2} + \frac{\beta-\beta^2}{2+\beta}$
Exponential function	EF	$p \in \mathbb{N}$	E	$1 - e^{-\beta}$

$$\int_\Gamma u_i \, ds - \int_\Gamma u_e \, ds + (e^{-\beta} + 1) \int_\Gamma I_m \, ds = e^{-\beta} \int_\Gamma v_t \, ds, \tag{2.26}$$

which is referred to in Table 2.1 as "Exponential function" (EF). This scheme represents the exact solution of the linear time-dependent equation.

As shown above, using both higher-order and implicit schemes in the passive conductance model can be done via direct calculation, and therefore at no additional computational cost.

2.2.2.4 Numerical Convergence of RK Schemes

In order to compare the convergence and stability of the different RK schemes, we consider the simple square unit domain shown in Fig. 2.2.

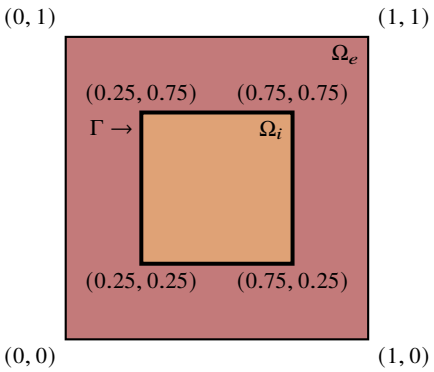

Fig. 2.2: Domain of integration. $\Omega_e, \Omega_i, \Gamma$ represent the extracellular space, the intracellular space and the membrane, respectively.

Using the manufactured solution method [21], we define the source functions

$$f = f(x, y, t) = -8\pi^2 \sin(2\pi x) \sin(2\pi y)(1 + e^{-t}), \tag{2.27}$$

$$g = g(x, y, t) = -8\pi^2 \sin(2\pi x) \sin(2\pi y). \tag{2.28}$$

In this case, the exact solution is given by,

$$u_i(x, y, t) = (1 + e^{-t}) \sin(2\pi x) \sin(2\pi y), \tag{2.29}$$

$$u_e(x, y, t) = \sin(2\pi x) \sin(2\pi y), \tag{2.30}$$

$$v(x, y, t) = e^{-t} \sin(2\pi x) \sin(2\pi y). \tag{2.31}$$

We calculate the L^2 error between the numerical solutions, $\tilde{u}_i^{N,\Delta t}$, $\tilde{u}_e^{N,\Delta t}$, $\tilde{v}^{N,\Delta t}$, using the finite element method (FEM) and the exact solutions above. We present the two error terms,

$$e_u^{N,\Delta t} = \sqrt{||u_i - \tilde{u}_i^{N,\Delta t}||^2 + ||u_e - \tilde{u}_e^{N,\Delta t}||^2}, \tag{2.32}$$

$$e_v^{N,\Delta t} = \sqrt{||v - \tilde{v}^{N,\Delta t}||^2}. \tag{2.33}$$

We assess the convergence with respect to both temporal and spatial resolution. For the spatial convergence test, we fix $\Delta t = 0.01/64$ and vary the mesh resolution parameter, $N = 16, 32, ..., 256$, which equals the number of intervals in each direction of spatial discretisation of the domain, as shown in Fig. 2.5. For the temporal resolution, we fix $N = 512$ and perform two experiments. Firstly, we use $\Delta t = 0.01/n$ for $n = 0.1, 0.5, 1, 2, 4, 8, 16, 32$, as shown in Fig. 2.6.

2.2.2.5 The Active Conductance Model

For the EMI model with active conductance, the time-dependent equation becomes [6],

$$\frac{dv}{dt} = \frac{1}{C_m} \left(I_m - I_{\text{ion}}(v(t)) \right), \tag{2.34}$$

where $I_{\text{ion}}(v(t))$ is a non-linear function, for example of Hodgkin-Huxley type. In this case, explicit expressions cannot be derived when applying RK schemes. Given an implicit RK scheme with Butcher tableau, $(\boldsymbol{A}, \boldsymbol{b})$, the scheme is again,

$$v_{t+1} = v_t + h \sum_{i=1}^{s} b_i k_i, \tag{2.35}$$

$$= v_t + h \boldsymbol{b}^\top \boldsymbol{k}. \tag{2.36}$$

However, the equations for k_i yield a non-linear system of equations to be solved at each time-step,

$$k_i = \frac{1}{C_m}(I_m - I_{\text{ion}}(v_t - h\sum_{j=1}^{s} a_{ij}k_j)), \tag{2.37}$$

which we write in vector notation as,

$$\boldsymbol{k} = \frac{1}{C_m}(I_m - F_{\text{ion}}(v_t, \boldsymbol{A}, \boldsymbol{k})), \tag{2.38}$$

where,

$$F_{\text{ion}}(v_t, \boldsymbol{A}, \boldsymbol{k}) = \begin{pmatrix} I_{\text{ion}}(v_t + \boldsymbol{e}_1^\top \boldsymbol{A}\boldsymbol{k}) \\ \vdots \\ I_{\text{ion}}(v_t + \boldsymbol{e}_s^\top \boldsymbol{A}\boldsymbol{k}) \end{pmatrix}, \tag{2.39}$$

where $\{\boldsymbol{e}_i\}_{i=1}^s$ are the standard basis vectors in $\mathbb{R}^s$.

Most frequently, one considers an active conductance of Hodgkin-Huxley type [1],

$$I_{\text{ion}}(v) = g_{\text{Na}}(v)(v - E_{\text{Na}}) + g_{\text{K}}(v)(v - E_{\text{K}}) + g_{\text{L}}(v)(v - E_{\text{L}}) + g(v)(v - E_{\text{Na}}), \tag{2.40}$$

where the gating variables, g_{ion}, for each ion, are non-linear functions of v given by the solution to an ODE. This form allows us to define semi-implicit schemes for this model. At each time step, the gating variables are updated according to a numerical method, typically the Rush-Larsen method [22]. To define a semi-implicit scheme, we update the gating variables with membrane potential v_t rather than the value $v_t + h\sum_{j=1}^s a_{ij}k_j$. This now yields a simplified system of equations for k_i,

$$\begin{aligned} k_i = \frac{1}{C_m}[I_m - g_{\text{Na}}(v_t)(v_t + h\sum_{j=1}^{s} a_{ij}k_j - E_{\text{Na}}) - g_{\text{K}}(v_t)(v_t + h\sum_{j=1}^{s} a_{ij}k_j - E_{\text{K}}) \\ - g_{\text{L}}(v_t)(v_t + h\sum_{j=1}^{s} a_{ij}k_j - E_{\text{L}}) - g(v_t)(v_t + h\sum_{j=1}^{s} a_{ij}k_j - E_{\text{Na}})], \end{aligned} \tag{2.41}$$

which is linear. In vector notation, the system becomes

$$\boldsymbol{k} = \frac{1}{C_m}[I_m - I_{\text{ion}}(v_t)]\boldsymbol{u} - \beta G\boldsymbol{A}\boldsymbol{k}, \tag{2.42}$$

where $G = g_{\text{Na}}(v_t) + g_{\text{K}}(v_t) + g_{\text{L}}(v_t) + g(v_t)$. This has solution,

$$\boldsymbol{k} = \frac{1}{C_m}[I_m - I_{\text{ion}}(v_t)](\boldsymbol{I} + \beta G\boldsymbol{A})^{-1}\boldsymbol{u}. \tag{2.43}$$

Thus, the scheme becomes as follows:

$$v_{t+1} = v_t + \beta \boldsymbol{b}^\top [I_m - I_{\text{ion}}(v_t)](\boldsymbol{I} + \beta G \boldsymbol{A})^{-1} \boldsymbol{u}. \tag{2.44}$$

Under the weak formulation this gives us conservation law,

$$\begin{aligned} \int_\Gamma u_i \, ds - \int_\Gamma u_e \, ds - \beta \boldsymbol{b}^\top (\boldsymbol{I} + \beta G \boldsymbol{A})^{-1} \boldsymbol{u} \int_\Gamma I_m \, ds \\ = \int_\Gamma v_t - I_{\text{ion}}(v_t) \boldsymbol{b}^\top (\boldsymbol{I} + \beta G \boldsymbol{A})^{-1} \boldsymbol{u} \, ds. \end{aligned} \tag{2.45}$$

However, this inverse matrix that must be calculated equates to solving a linear system at each time step.

2.2.3 Model Setup and Geometries

We employ the multi-dimensional EMI formulation (eq. 2.1) with an implicit Euler scheme (eq. 2.4). We use a Hodgkin-Huxley active conductance model [1] integrated with a Rush-Larsen scheme [22]. The source terms f and g in eq. 2.1 are set to 0 [6].

The model parameters were chosen as shown in Table 2.2. The conductance values for the unmyelinated axons correspond to the giant squid axon [1]. For the myelinated axons, we scaled the corresponding unmyelinated conductances such that the total number of ion channels would match for the two axon types. The axon length, radii, and node lengths were chosen to make the geometry and results easier to visualize. The synaptic conductance $g(v_t)$ in I_{ion} represents a stimulation current applied to a synapse of length l_{node} on one edge of unmyelinated and myelinated axons.

2.2.3.1 Single Axon with and without Myelination

Fig. 2.3 illustrates the geometries we employed in our simulation to compare the velocity of the action potential in a single axon for the unmyelinated (a) and myelinated (b) scenarios. Table 2.2 contains the parameters used for the axons.

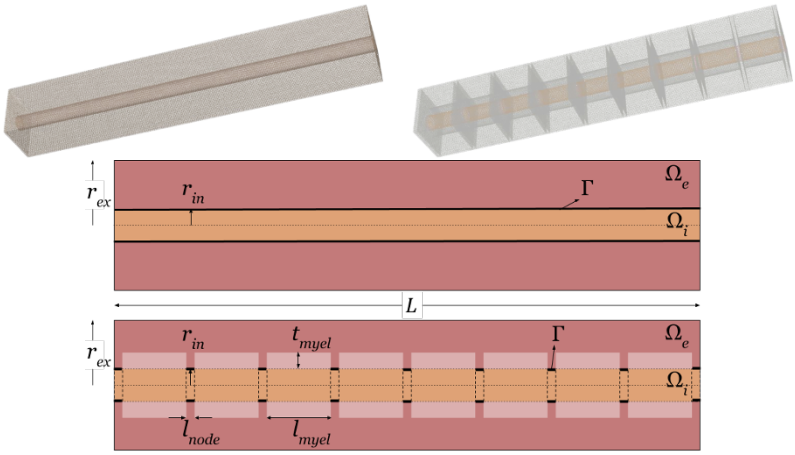

Fig. 2.3: ParaView renders of the `gmsh` geometries for (top left) unmyelinated, and (top right) myelinated single axons, where (bottom) shows a schematic representation of both axon types using parameters from Table 2.2.

Table 2.2: Parameters used for single axon simulations with and without myelin.

Parameter	**Value**	
	Unmyelinated	Myelinated
Axon length L (mm)	10	10
Intracellular radius r_{in} (mm)	0.2	0.2
Extracellular radius r_{ex} (mm)	1	1
Myelin thickness t_{myel} (mm)	–	0.2
Number of nodes of Ranvier	–	10
Length of node l_{node} (mm)	–	0.1
Internodal distance $l_{myel}(mm)$	–	1
$\bar{g}_L(mS/cm^2)$	0.3	3
$\bar{g}_{Na}(mS/cm^2)$	120	1200
$\bar{g}_K(mS/cm^2)$	36	360
$E_L(mV)$	-54.38	-54.38
$E_{Na}(mV)$	54.8	54.8
$E_K(mV)$	-88.98	-88.98

2.2.3.2 Axon Bundle

For our simulations considering bundles of unmyelinated axons, we arranged nine axons in a 3×3 grid. A cross-section showing this spatial arrangement is depicted in Fig. 2.4. Each axon in the bundle was matched to use the same parameters and geometries as the single axon simulations described previously. The same arrange-

ment and parameter matching to single axon simulations was also applied to a 3×3 bundle of myelinated axons.

For both the unmyelinated and myelinated axon bundles, the eight axons on the periphery were stimulated using synapses of length l_{node} (as in the single axon simulations), while the central axon in the bundle was not stimulated externally. Membrane voltage changes in this central axon were examined to look for evidence of ephatic coupling.

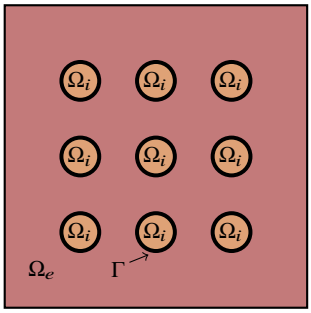

Fig. 2.4: Arrangement of nine axons forming a bundle. Ω_i denotes the intracellular space of each axon, Ω_e denotes the extracellular space, and Γ denotes the membranes.

2.3 Results

2.3.1 Convergence

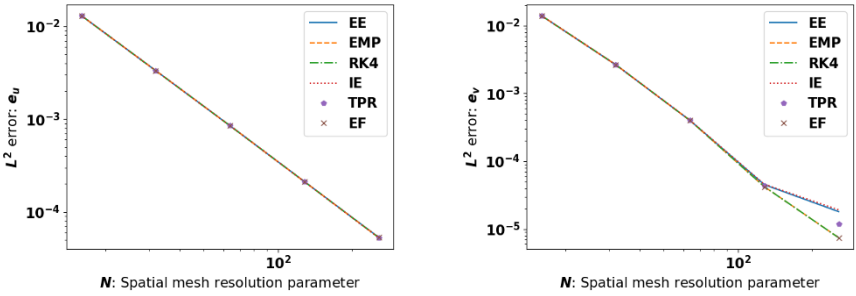

Fig. 2.5: Convergence with respect to mesh size with fixed time-step. Left: e_u Right: e_v.

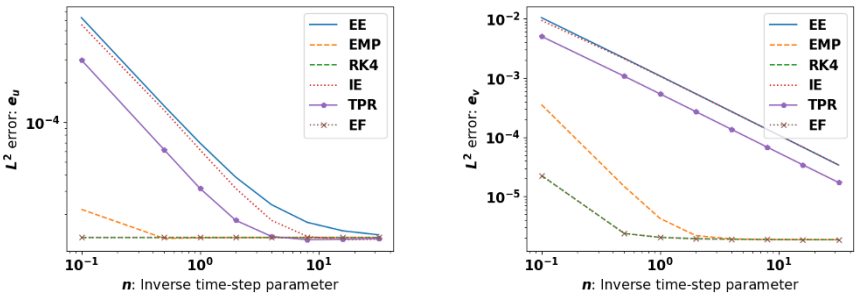

Fig. 2.6: Convergence with respect to temporal resolution for small time-steps and fixed mesh size. Left: e_u Right: e_v.

Firstly, we consider the convergence results for the square-in-square, passive conductance, manufactured solution discussed previously. We integrate the system using FEniCS and the RK schemes listed in Table 2.1. In Fig. 2.5, we display the error for a sequence of increasing spatial (mesh) resolutions for both the intra-extracellular potential and the membrane potential. As shown, all the methods converge comparably with respect to mesh resolution, as they only modulate the time-stepping error. Next, we consider a series of decreasing time steps. As can be seen in Fig. 2.6, higher-order methods are limited by spatial discretisation, but all methods appear to converge to the exact solution. It is clear that the higher-order methods, EMP, RK4 and TPR have lower errors than the first-order methods EE and IE. For these higher-order methods, in order to assess their convergence and their stability, we find the time steps at which they obtain similar error values. By increasing the time steps so dramatically, we can limit the effect of the spatial discretisation error and compare the methods more effectively. As shown in Table 2.3, the least stable of

Table 2.3: Errors for large time-steps for higher order RK schemes.

Δt	**RK4**		Δt	**EMP**		Δt	**TPR**	
	e_u	e_v		e_u	e_v		e_u	e_v
2.5	1.03×10^{-5}	5.62×10^{-6}	1.6	1.03×10^{-5}	2.15×10^{-4}	3.0	1.60×10^{-5}	2.50×10^{-4}
2.6	2.99×10^{-5}	4.70×10^{-4}	1.8	1.64×10^{-5}	2.15×10^{-4}	3.2	1.30×10^{-4}	2.17×10^{-3}
2.7	1.74×10^{-3}	2.90×10^{-2}	2.0	1.65×10^{-1}	2.78	3.4	1.12×10^{-3}	1.87×10^{-2}

the higher order methods is EMP, followed by RK4 and finally TPR, the implicit scheme. Importantly, the higher order explicit schemes had much lower error yet are less stable. This means that, depending on the constraints of the particular problem, one should opt for an implicit scheme for greater stability or an explicit scheme for greater accuracy.

2.3.2 Speed of Action Potential Propagation in Single Axons

We conducted a simulation to compare the propagation speed of an action potential in a myelinated axon with that of an unmyelinated one. Fig. 2.7 shows the membrane potential in both cases recorded at a single point on the membrane and at the end of the axon. The action potential profile is similar in both cases. The key difference is that the potential propagates faster in the myelinated axon; therefore, it arrives at the end of the axon earlier, as shown in Fig. 2.7.

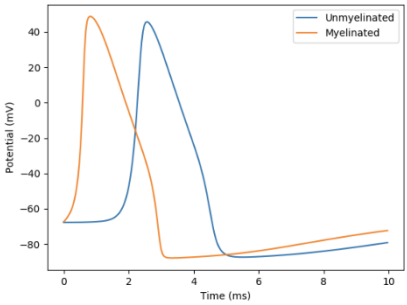

Fig. 2.7: Potential of myelinated and unmyelinated axons over time measured at the node located at the end of the axon membrane.

Our simulation supports the biological theory that argues that myelination causes faster propagation of action potential [23]. This further validates this approach to modeling myelination by modulating the conductance values in the nodes of Ranvier.

2.3.3 Ephaptic Coupling in Unmyelinated and Myelinated Axon Bundles

Next, we simulate the 9-cylinder axonal bundle with myelinated and unmyelinated axons, while stimulating only the 8 peripheral axons. We then measured the induced activity in the unstimulated central axon.

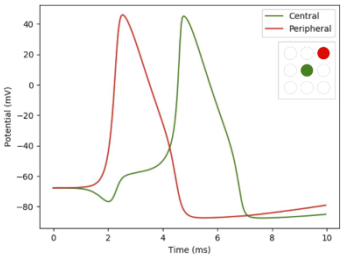

(a) Comparison between the action potential of the central and peripheral axon in the unmyelinated case.

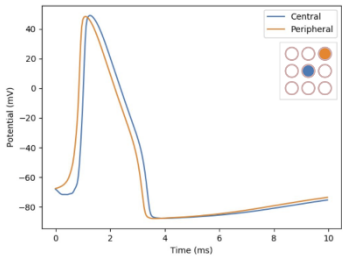

(b) Comparison between the action potential of the central and peripheral axon in the myelinated case.

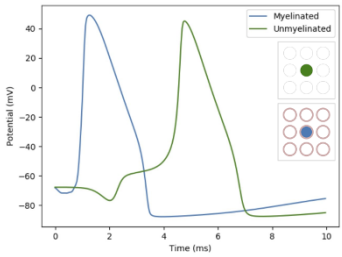

(c) Comparison between the action potential of central axons in the unmyelinated and myelinated cases.

Fig. 2.8: Plots showing the action potentials induced in the central axon alongside (a chosen) peripheral axon in both the myelinated and unmyelinated cases.

In Fig. 2.8 (subfigure 2.8a), we show that in the unmyelinated case, ephaptic coupling did occur as an action potential was induced in the central axon. There is a noticeable time-lag between the spike in the peripheral and central axons. In the myelinated case, shown in Fig. 2.8 (subfigure 2.8b), ephaptic coupling also occurred with an induced potential in the central axon. There is no such time-lag in the case of the myelinated axons. The different profiles of the induced action potentials in each case are highlighted in Fig. 2.8 (subfigure 2.8c), which shows the unmyelinated and myelinated central axons side by side.

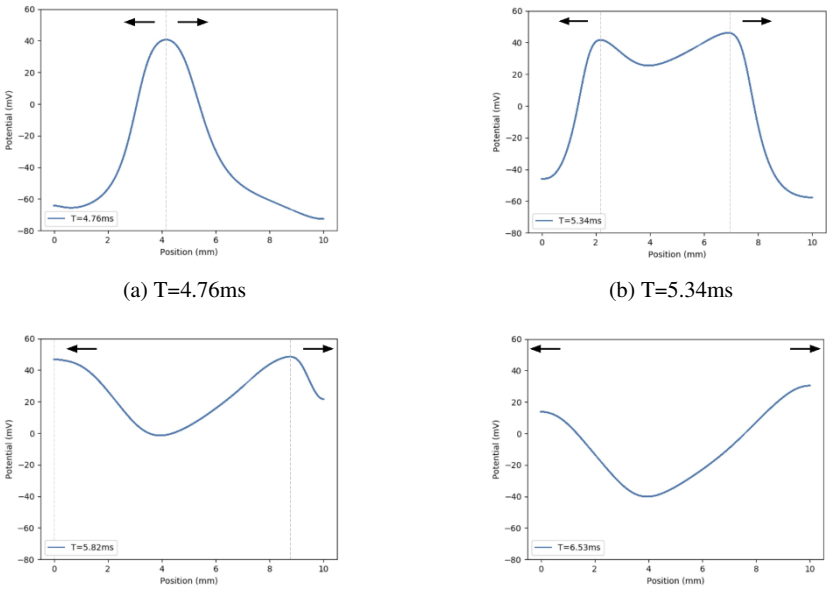

(a) T=4.76ms (b) T=5.34ms

(c) T=5.82ms (d) T=6.53ms

Fig. 2.9: Action potentials induced in the central axon of the unmyelinated bundle for different time-stamps. Arrows depict the splitting of the induced potential into forward and backward propagating impulses.

Interestingly, in our simulations we have observed a backpropagation phenomenon in the central unmyelinated axon as one can see from Fig. 2.9.

Our simulations show that ephaptic coupling is possible in the EMI model, for both myelinated and unmyelinated axons. Furthermore, we have shown that myelination severely increases the speed of the propagation of action potentials under direct stimulation and indirect induction.

2.4 Discussion

In this report, we presented a computational approach to modeling myelination and ephaptic coupling of axons using the EMI framework [6]. As part of this analysis, we studied a range of time-stepping algorithms for both the passive and the Hodgkin-Huxley conductance models, obtaining an analytical expression for the weak formulation for generalized RK schemes. As a result, we can integrate the EMI model with any RK scheme. We concluded that higher-order schemes are advantageous in terms of both stability and accuracy, with explicit methods being more accurate and implicit methods being more stable. Our computational simulations

also validated the hypothesis that myelination speeds up the propagation of action potentials. Finally, we showed that ephaptic coupling was possible in the EMI model for both myelinated and unmyelinated axons, where myelination accelerated the propagation of the induced action potential.

Our work further supports the notion that biophysical models of excitable cells should take into account spatial geometry and dynamics to model more specialized biological phenomena. Both myelination and ephaptic coupling are important features of neuronal function and show pathology in disease, such as myelin loss in multiple sclerosis [24] or reduced ephaptic entrainment in neurodegenerative conditions [16]. For this reason, our report represents an important step towards complete models of excitable cells and the phenomena that can arise.

Although the EMI framework is a detailed and biophysically realistic model, further work using the more detailed KNP-EMI model [11], would allow for a more complete analysis of the parameters that modulate the emergence of induced action potentials, such as the distance between the axons in the bundle. Parameter values as measured in demyelinated axons could also be considered for modeling ephaptic coupling under pathological conditions [25].

Furthermore, this report is a proof-of-concept showing that modeling ephaptic coupling and myelination is possible within this model, yet does not claim to replicate the exact dynamics seen in biological experiments. Further studies could confirm that the model outputs are consistent with theoretical predictions, that is, from the cable equation [26], or from experimental results.

References

1. Alan Lloyd Hodgkin and Andrew Fielding Huxley. A quantitative description of membrane current and its application to conduction and excitation in nerve. Journal of Physiology, 117(4), 1952.
2. Richard FitzHugh. Mathematical models of threshold phenomena in the nerve membrane. The Bulletin of Mathematical Biophysics, 17:257–278, 1955.
3. J. L. Hindmarsh and R.M. Rose. A model of neuronal bursting using three coupled first order differential equations. Proceedings of the Royal Society of London. Series B. Biological Sciences, 221(1222):87–102, 1984.
4. Daniel K Hartline. What is myelin? Neuron Glia Biology, 4(2):153–63, 2008.
5. Costas A Anastassiou, Rodrigo Perin, Henry Markram, and Christof Koch. Ephaptic coupling of cortical neurons. Nature Neuroscience, 14(2):217–23, 2011.
6. Aslak Tvieto, Kent-Andre Mardal, and Marie E Rognes. Modeling Excitable Tissue: The EMI Framework. Springer, 2021.
7. Pierre Morell and Richard H Quarles. Basic Neurochemistry: Molecular, Cellular and Medical Aspects. Lippincott-Raven, 6th edition, 1999.
8. A. Arvanitaki. Effects evoked in an axon by the activity of a contiguous one. Journal of Neurophysiology, 5(2):89–108, March 1942. Publisher: American Physiological Society.
9. J. G. Jefferys. Nonsynaptic modulation of neuronal activity in the brain: electric currents and extracellular ions. Physiological Reviews, 75(4):689–723, October 1995. Publisher: American Physiological Society.
10. Costas A. Anastassiou and Christof Koch. Ephaptic coupling to endogenous electric field activity: why bother? Current opinion in neurobiology, 31:95–103, 2015.

11. Ada J. Ellingsrud, Andreas Solbrå, Gaute T. Einevoll, Geir Halnes, and Marie E. Rognes. Finite element simulation of ionic electrodiffusion in cellular geometries. Frontiers in Neuroinformatics, 14(11), 2020.
12. Giulio Ruffini, Ricardo Salvador, Ehsan Tadayon, Roser Sanchez-Todo, Alvaro Pascual-Leone, and Emiliano Santarnecchi. Realistic modeling of mesoscopic ephaptic coupling in the human brain. PLOS Computational Biology, 16(6):e1007923, June 2020. Publisher: Public Library of Science.
13. Flavio Fröhlich and David A. McCormick. Endogenous Electric Fields May Guide Neocortical Network Activity. Neuron, 67(1):129–143, July 2010.
14. S. Binczak, J. C. Eilbeck, and A. C. Scott. Ephaptic coupling of myelinated nerve fibers. Physica D: Nonlinear Phenomena, 148(1):159–174, January 2001.
15. Helmut Schmidt, Gerald Hahn, Gustavo Deco, and Thomas R. Knösche. Ephaptic coupling in white matter fibre bundles modulates axonal transmission delays. PLOS Computational Biology, 17(2):e1007858, February 2021. Publisher: Public Library of Science.
16. Gabriel Moreno Cunha, Gilberto Corso, Marcelo M. S. Lima, and Gustavo Zampier dos Santos Lima. Electrophysiological damage to neuronal membrane alters ephaptic entrainment. Scientific Reports, 13(11974), 2023.
17. Giovanni Grasso, Alessandro Landi, and Concetta Alafaci. A Novel Pathophysiological Mechanism Contributing to Trigeminal Neuralgia. Molecular Medicine, 22(1):452–454, January 2016. Number: 1 Publisher: BioMed Central.
18. Thomas Brandt, Michael Strupp, and Marianne Dieterich. Vestibular paroxysmia: a treatable neurovascular cross-compression syndrome. Journal of Neurology, 263(1):90–96, April 2016.
19. Emilie Kierig, Johannes Gerb, Rainer Boegle, Birgit Ertl-Wagner, Marianne Dieterich, and Valerie Kirsch. Vestibular paroxysmia entails vestibular nerve function, microstructure and endolymphatic space changes linked to root-entry zone neurovascular compression. Journal of Neurology, 270(1):82–100, January 2023.
20. Ernst Hairer and Gerhard Wanner. Solving Ordinary Differential Equations II: Stiff and Differential-Algebraic Problems. Springer, 1996.
21. Aslak Tvieto, Karoline Jaeger, Miroslav Kuchta, Kent-Andre Mardal, and Marie E Rognes. A cell-based framework for numerical modeling of electrical conduction in cardiac tissue. Frontiers in Physics, 5(48), 2017.
22. S Rusch and H Larsen. A practical algorithm for solving dynamic membrane equations. IEEE Transactions on Biomedical Engineering, 25:389–392, 1978.
23. D Purves, GJ Augustine, and D Fitzpatrick. Neuroscience. Sunderland, 2001.
24. Maria Podbielska, Naren L Banik, Ewa Kurowska, and Edward L. Hogan. Myelin recovery in multiple sclerosis: The challenge of remyelination. Brain Sciences, 3(3):1282–1324, 2013.
25. Michael Hines and Peter Shrager. A computational test of the requirements for conduction in demyelinated axons. Restorative Neurology and Neuroscience, 3(2):81–93, 1991.
26. H Bokil, N Laaris, K Blinder, M Ennis, and A Keller. Ephaptic interactions in the mammalian olfactory system. Journal of Neuroscience, 21(20), 2001.

Chapter 3
Augmentation of Cardiac Ischemic Geometry for Improving Machine Learning Performance in Arrhythmic Risk Stratification

Ambre Bertrand, Carolyna Yamamoto, Giulia Monopoli, Thomas Schrotter, Lena Myklebust, Julie J Uv, Hermenegild J Arevalo, and Mary M Maleckar

Abstract Ventricular arrhythmias frequently occur as a complication of myocardial infarction (MI), due to significant changes in the heart's structure and electrophysiology. If left untreated, these alterations may lead to sudden cardiac death (SCD). It is therefore critical to evaluate risk prediction accurately in post-infarction patients to enable early intervention and improve patient outcomes. This work introduces a novel approach to improve arrhythmia risk assessment in post-infarction patients. We propose a new pipeline to build physiologically realistic image-based models of patient hearts, producing more realistic meshes compared to publicly available pipelines. We generate a library of 90 cardiac geometries of MI patients and use

Ambre Bertrand
Department of Computer Science, University of Oxford, UK

Carolyna Yamamoto
Department of Biomedical Engineering, Johns Hopkins University, USA

Giulia Monopoli
Department of Computational Physiology, Simula Research Laboratory, NO; Department of Mathematics, University of Oslo, NO

Thomas Schrotter
Gottfried Schatz Research Center - Division of Medical Physics and Biophysics, Medical University of Graz, AT

Lena Myklebust
Department of Computational Physiology, Simula Research Laboratory, NO; Department of Informatics, University of Oslo, NO

Julie J Uv
Department of Computational Physiology, Simula Research Laboratory, NO; Department of Informatics, University of Oslo, NO

Hermenegild J Arevalo
Department of Computational Physiology, Simula Research Laboratory, NO

Mary M Maleckar (corresponding author)
Department of Computational Physiology, Simula Research Laboratory, NO e-mail: mmaleck@simula.no

K. J. McCabe (ed.), *Computational Physiology*, Simula SpringerBriefs on Computing 17,
https://doi.org/10.1007/978-3-031-53145-3_3

these cardiac models to estimate likelihood of reentry using electrophysiological (EP) simulations. However, due to the computationally expensive nature of this approach, we also introduce a data augmentation pipeline to train a machine learning (ML) model for risk stratification, enabling accurate and real-time prediction of the simulation outcomes. Our trained ML model achieved an accuracy of 88.0% and F1 score of 48%, with a prediction time of 0.01 seconds per case (compare with approximately 5 hours per case for EP simulations). In conclusion, the work presented here improved the accuracy of personalised biventricular geometries, introduced a novel data augmentation approach for scar distribution, and decreased prediction time of risk of arrhythmias post-MI by more than five orders of magnitude.

3.1 Introduction

Ventricular arrhythmias are a common consequence of MI and are associated with a significant increase in SCD in post-MI patients [1, 2]. Infarction occurs when blood flowing to a portion of the myocardium decreases or stops flowing altogether, typically due to a narrowed or completely occluded coronary artery. A rapid reparative process is initiated to rebuild the infarcted myocardium and preserve the structural integrity of the ventricles, resulting in the formation of a scar [3]. Ventricular scar tissue is characterised by dense fibrosis, comprising of collagen and fibrocytes, as well as regions containing surviving myocyte bundles. The heterogeneous presence of dense fibrosis can lead to conduction block, delineating the borders of potential reentry circuits. Fibrosis also contributes to the development of slow tissue conduction, a pivotal factor in the formation of reentry mechanisms [4]. The combination of these factors creates a vulnerable environment, acting as a substrate for ventricular arrhythmias. The role of fibrotic tissue in initiating and maintaining ventricular arrhythmias is indeed complex and remains an active area of research [5, 6, 7]. Timely and accurate prediction of these arrhythmias is crucial to enable early intervention and improve post-MI patient outcomes, and as such represents an important clinical challenge to address.

The occurrence of arrhythmic events in patients at risk may be prevented by an implantable cardioverter-defibrillator (ICD), making these devices the primary treatment of choice for high-risk post-MI patients [8]. However, ICD implantation is costly and associated with adverse effects [9]. Therefore, there is value in developing non-invasive methods for prospective identification of post-MI patient subgroups with the highest risk of arrhythmia.

Image-derived mechanistic computational models of cardiac electrical function have proven successful in predicting arrhythmic risk [10, 11]. Despite their effectiveness, these methods rely on complex, computationally expensive models. As a result, there is a growing need for more efficient approaches. By replacing mechanistic simulations with a statistical model, it is possible to learn the relationship between the inputs and outputs of a physical process, based solely on data and with no phenomenological information. Deep learning (DL) models have emerged as a

promising solution, due to their ability to analyse large amounts of data and identify complex patterns [12, 13, 14, 15]. While these statistical methods reduce computational cost compared to mechanistic simulations, achieving accurate results requires a substantial amount of training data [16].

Data augmentation can help address this issue by increasing the size and complexity of the training dataset, thanks to manipulations performed on the existing data. Augmenting the dataset enhances the model's ability to generalise to unseen cases, by exposing it to more heterogeneous cases and mitigating overfitting [17]. To this end, biophysical simulations of cardiac electrical function can be used to generate large amounts of data within physiological expectations. Thus, DL models are able to better capture process intricacies at a local scale and better represent population heterogeneities at a global scale, improving their accuracy in performing personalized predictions of arrhythmic risk.

This study aims to enhance risk stratification of post-MI patients using augmented, biophysically-accurate image-based models of the heart. Building on the work by [14], we propose a novel meshing pipeline to obtain realistic anatomical models based on patient magnetic-resonance (MR) images, including ventricular scar location and fiber orientation. To increase the variability of our population, we augment the original anatomical models obtained from clinical MR images by changing scar characteristics including size, thickness and location. We then perform personalised electrophysiological simulations on over 100 different modelled cases to obtain activation sequences in the ventricles using varying conduction velocities to reflect tissue properties in healthy tissue and scar. Subsequently, we determine the risk of arrhythmia of each case based on the absence or presence of reentry observed in the simulation results.

Understanding the pathophysiological link between anatomical properties of the healthy myocardium and scar and ventricular arrhythmias can inform approaches to identify patients at risk. Using the augmented dataset and simulation outputs, we train a graph convolutional neural network (GCN) to predict the occurrence of reentry based on regional properties of the myocardium. Our model is able to emulate the simulation results within 88.0% accuracy and improve prediction time by five orders of magnitude, thus enabling rapid, personalised risk stratification.

3.2 Methods

3.2.1 Dataset

The available data consists of standard short axis late gadolinium enhanced magnetic resonance images (LGE MRI) provided by Rigshospitalet in Copenhagen, DK, which counts 30 confirmed cases suffering from first-time MI. The reader can refer to [14] for further details.

3.2.2 Data Augmentation

3.2.2.1 Ventricular Mesh Generation

For each scan, the LGE MRI stack was imported into ADAS 3D (version 2.12.0) and the slices were automatically aligned using their pre-trained model. The left ventricular (LV) epicardium and endocardium contours were automatically generated using the ADAS 3D auto-segmentation model with only minor manual adjustments needed. For the right ventricle (RV), the epicardium and endocardium were manually segmented and the contours were then generated.

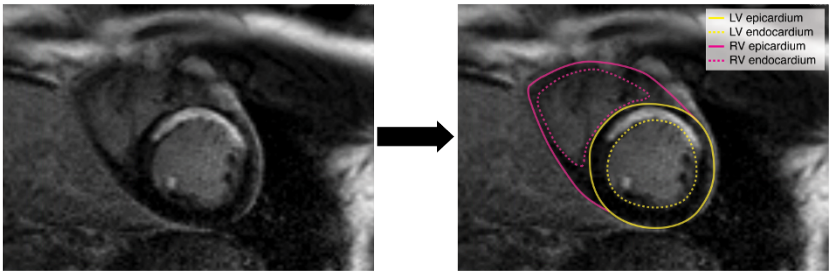

Fig. 3.1: Left: Short axis LGE MRI. Right: Contours of the epicardium and endocardium of the left ventricle (LV) and the right ventricle (RV).

The extracted contours (Figure 3.2A) were refined using an automated pre-processing script based on Blender (version 3.01). The refinement ensures that the ventricular base is consistently flat (Figure 3.2B). The resulting surfaces (ventricular base, LV epi- and endocardium, RV epi- and endocardium and septum) represent a single closed surface of a biventricular mesh (Figure 3.2C).

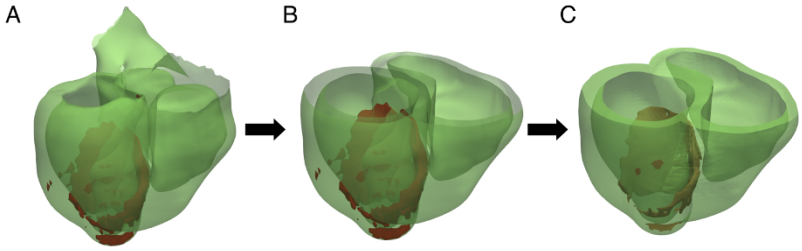

Fig. 3.2: (A) Surface mesh generated from epicardial and endocardial contours of the left and right ventricles (green) and surface mesh of the scar generated from 50% FWHM (red). (B) Ventricular mesh with flat base. (C) Closed-surface biventricular mesh and smoothed scar mesh.

The surfaces are combined, scaled and rendered as a single 3D tetraheadral mesh using gmsh (version 4.8.4) [18]. Based on considerations of [14] we chose a spatial resolution of 400 µm for each generated mesh. At this point, the generated 3D mesh does not include any cardiac muscle fiber information. To generate fiber information for a given mesh an implementation based on the works of [19] was used. Finally, in order to be able to perform openCARP simulations [20], the resulting mesh is converted to the respective CARP format using meshtool [21].

3.2.2.2 Scar Mesh Generation

After generating the LV epicardial and endocardial contours in ADAS 3D, the LV scar tissue was characterized using full width at half maximum (FWHM) threshold method. For every LGE MRI scan, at least 3 distinct scar geometries were generated using different FWHM percentages: 30%, 50% (Figure 3.2A), and an arbitrary percentage value between 20% and 70%, other than 30% or 50%. Subsequently, each scar surface mesh underwent refinement in Blender to ensure that the scar tissue is contained within the left ventricle and that small scar chunks with a surface smaller than 10 mm^2 are discarded. Furthermore, the refinement process improves the quality of the scar surface by eliminating any artifacts and smoothing the scar surfaces (Figure 3.2C). Finally, the scar surfaces are incorporated into the 3D tetrahedral mesh generation process.

In order to extend the scar population per mesh, an artificial scar generation algorithm was developed which injects scar tissue into given biventricular geometries. The algorithm solves an Eikonal wave equation for a given set of either manually or randomly selected source points within the mesh [22]. The volumes contained within the propagated wavefronts, after an adjustable period of time, are labeled as new scar tissue (Figure 3.3). Furthermore, inner regions of generated scar tissue are labeled as infarct tissue, while the outer regions are labeled as border zone. The

velocity of the wave propagation can be controlled in order to generate complex scar shapes.

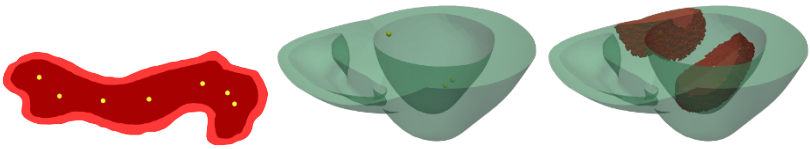

Fig. 3.3: Artificial scar generation illustration with example. Based on source points (yellow) a propagating wave is computed. The enclosed volume represents new scar tissue with border zone (light red) and ischemic tissue (dark red).

3.2.2.3 Mesh Feature Extraction

After generating the LV epicardial and endocardial contours in ADAS 3D, the 17 American Heart Association (AHA) segments were computed for the LV. The AHA segments are a widely accepted clinical convention that define different anatomical regions of the LV [23]. For each segment, we calculated the segment mass, LV wall thickness, scar mass within the segment, and scar percentage. In addition to the segments, the region between the LV endocardium and epicardium was divided into 10 layers (with Layer 1 corresponding to the endocardial surface and Layer 10 corresponding to the epicardial surface). For each segment, we also calculated the layer surface area, scar area, and scar percentage for each of the 10 layers within the segment.

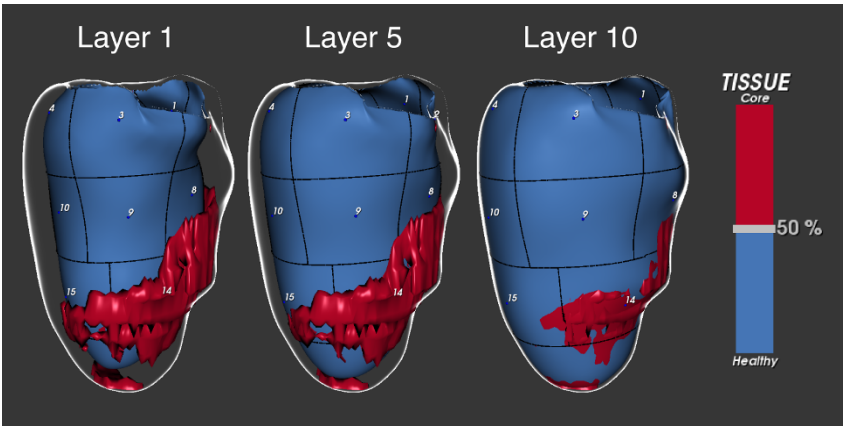

Fig. 3.4: Left ventricle anatomy subdivided into 17 AHA segments and 10 layers from endocardium to epicardium. Scar threshold at 50% FWHM.

3.2.3 Electrophysiological Simulations

Building upon the work of [14], we incorporated the Ten Tusscher model [24] to simulate electrical wave propagation in healthy cardiac tissue. By manipulating ionic conductances and tissue conductivity reduction along transverse and longitudinal axes, our model captured the intricate progression of damage occurring post-MI. We employed the same parameters for healthy tissue and ischemic regions as those used in [14]'s work.

3.2.3.1 Stimulus Point Selection

For the selection of the stimulation points, we follow a different strategy than [14]. Instead of selecting a stimulation point per AHA segment, we decided to select stimulation points which are positioned near the scar. [25] showed that premature beats in acute ischemia first occur in healthy myocardium adjacent to ischemic regions; stimulation points near the scar tissue are therefore more likely to induce reentry. Furthermore, the selection of stimulation points follows a similar strategy as the artificial scar generation approach presented in Section 3.2.2.2. Specifically, the border zone of each scar is used as a starting point for the Eikonal wave propagation algorithm. The volume enclosed within the propagated wavefront after a short period of time represents tissue which is close to the scar (Figure 3.5). Within this volume, we select a number of points and ensure that they are spaced apart by a minimum distance.

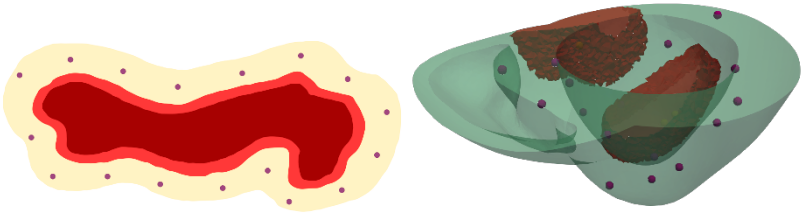

Fig. 3.5: Stimulation point selection illustration with example. Starting from the border zone regions (light red) a propagating wave is computed. The enclosed volume (light yellow) represents a region near the scar tissue. Within this region up to 17 stimulation points are selected.

3.2.3.2 Vulnerability Simulation Protocol

We conducted the simulation protocol at the different locations (see Section 3.2.3.1) pointed out in [14]. In summary, each simulation involved the delivery of pacing stimuli, known as S1. Initially, these S1 stimuli were administered with a fixed cycle

length of 350 milliseconds, followed by an S2 stimulus 200 milliseconds later. If no irregular heart rhythms were observed during this phase, we gradually reduced the time interval between S1 and S2 in 10-millisecond increments. We continued this process until we either detected abnormal reentrant circuits within the heart, or until the S2 stimulus failed to propagate. In cases where the S2 stimulus failed to propagate, we introduced an S3 stimulus 250 milliseconds after the last successful S2 delivery, and followed the same procedure as before. If reentry was not detected even after the S3 stimulus, we introduced an additional S4 stimulus 250 milliseconds later, following the same protocol as with the S2 and S3 stimuli. Finally, the resultant outcomes were categorized as follows: absence of reentry, temporary reentry, or persistent reentry.

3.2.4 Arrhythmic Risk Prediction Model

The electrophysiological simulations described above provide an accurate estimation of ventricular activation times and, if present, re-entrant circuits in each subject. Simulation outputs are obtained using a fully phenomenological, multi-scale modelling pipeline that requires high performance computing (HPC) resources. As such, this approach is computationally expensive. From a clinical perspective, this limitation creates a need for faster methods that can reliably estimate of the outcome of interest whilst avoiding the requirement of HPC resources, which are typically scarce in clinical settings. Here, we present a machine learning emulator of the simulation model based on a large population of virtual cases, to accelerate re-entry risk predictions and circumvent the need for HPC in the clinic. The overall model pipeline is presented in Figure 3.6.

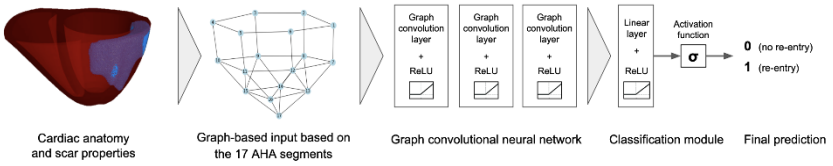

Fig. 3.6: Proposed pipeline for the arrhythmic risk prediction model using a graph-based representation of the heart, including global and local properties. The model is based on a graph convolutional network, GCN, and is trained on ground truth labels (reentry or no reentry) obtained from numerical simulations.

3.2.4.1 Training Data Generation

Our predictive model is developed using data obtained from the original dataset described in [14]. This dataset comprises 129 cases; 30 original image-based patient-specific cardiac models, plus an additional 99 augmented models with varying scar size and transmurality, amounting to a total of 1 to 5 cases per patient. Cases originating from the same patient are used for either training or testing, not both, to avoid training data information leaking into the test set. Given its small size, the dataset is split into training and testing sets with a 80%-20% ratio, yielding 104 training cases (25 patients) and 25 test cases (5 patients).
The ground truth label for each case is derived from the results of the numerical simulations determining ventricular activation times, reentry circuits, and subsequent risk of arrhythmia in [14]. The binary label extracted from these simulations represents the presence (1) or absence (0) of a reentry observed in each simulated case.

3.2.4.2 Data Representation

Given the complexity of the anatomical models, dimensionality reduction and feature extraction are a necessary pre-processing step to capture the data efficiently before it can be used as input to the machine learning model. We encapsulate structural properties of the cardiac models at a global scale by building a graph-based representation of each model based on the 17 AHA left ventricular segments [23]. Each graph consists of 17 nodes and 72 edges; this structure is identical for all cases. Each node corresponds to one AHA segment, while edges represent an existing connection between neighbouring segments. This representation allows us to implicitly encode the structure of the heart in an anatomically accurate manner, instead of having to represent this information in tabular format. In addition, we include two regional tissue properties computed for each segment: segment volume (ml) and scar volume (ml). For segments where no scar is present, the latter value is set to zero. These local properties, which vary from case to case, are encoded within a feature vector at each node corresponding to the relevant segment.

3.2.4.3 Model Architecture

Graph convolutional networks extend on traditional convolutional neural network architectures, originally developed for grid-like Euclidian spaces, by applying the same filtering principles to graph-like data [26]. We develop a model using GCN layers to process the data encapsulated by our graphical inputs, followed by a classification module to perform binary classification. We propose a GCN-based graph-level prediction architecture with the following structure:

1. One input GCN layer size (2,h) followed by rectified linear unit (ReLU) activation.

2. Two hidden GCN layers size (h,h) to convolve the node-wise features, followed by ReLU activation.
3. One output GCN layer size (h,1) to obtain a single node-wise feature.
4. One fully connected linear layer size (17,1) to obtain a single output feature from the 17 node-wise outputs.
5. A final sigmoid activation layer to obtain the final prediction as a probability between 0 and 1.

Typically, the size h of the hidden layers is chosen as an intermediate between the input and output sizes. Given that each node has two input features and one output, we select h=2 as an adequate hidden layer size. Only two hidden layers are implemented to avoid overfitting, given the small dataset size. The model has a total number of 39 parameters, less than half the size of the dataset, which also helps to minimise the chance of overfitting.

3.2.4.4 Training and Evaluation

Binary cross-entropy is chosen as a suitable loss function to train the model, as it measures the difference between predicted probabilities and ground truth binary labels. Given the small size of the dataset, we train our model for 200 epochs with a batch size of 1, a learning rate of 0.001, and the Adam optimiser [27].

The model is evaluated using different metrics to reflect its performance in predicting presence or absence of re-entry. Accuracy measures the correctly classified observations across both outcomes, while F1 score combines precision and recall to measure the performance of the model in classifying a single type of outcome. F1 score is the typical metric used to evaluate the performance of a binary classifier.

3.2.4.5 Implementation and Software

We used Python v3.10, with Pytorch v1.4 and Pytorch Geometric v2.3.1. The model was trained using Google Colab with an NVIDIA T4 GPU, 12.7GB of system RAM, and 78.2GB of disk memory.

3.3 Results

3.3.1 Mesh Pipeline

Figure 3.7 shows a subset of generated meshes of the pipeline. Using the entire height of a surface mesh (e.g., Figure 3.2) produces CARP files which are roughly twice as large in size compared to those of [14].

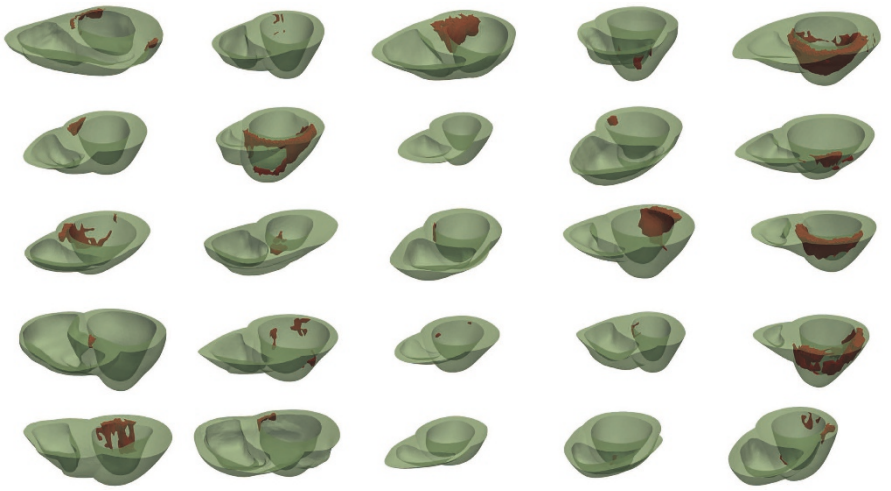

Fig. 3.7: 25 out of 30 generated meshes from our meshing pipeline using 50 % FWHM. Each mesh contains heart tissue (green) and scar tissue (red).

In order to reduce the mesh size to similar levels as [14] we decided to restrict the mesh generation to the lower 25% part of the biventricular mesh geometry. Furthermore, this step also greatly reduces computation times for EP simulations. In cases where no scar tissue is present within the 25% lower part of the mesh geometry we replace scars using the scar injection algorithm from Section 3.2.2.2.

3.3.2 EP Simulations

Despite the reduction of mesh sizes, we were unfortunately not able to complete all EP simulations for the entire biventricular population in the allotted time frame. Because of this circumstance, we decided to use the data from [14] for the arrhythmic risk prediction model.

3.3.3 Performance of Arrhythmic Risk Prediction Model

The simulation results taken from [14] are summarised in Figure 3.8. Of the 129 simulations, re-entry was induced in 53 cases, while the remaining 76 cases resulted in a healthy ventricular activation pattern with no re-entries observed. Here, we consider cases with induced re-entry as the positive class. After splitting the dataset into training and testing sets, we obtain 40 positive cases in the training set (64 negative cases) and 10 positive cases in the testing set (15 negative cases). We

observe a trend between increasing scar size and occurrence of re-entry, and largest percentage of re-entries in areas of the left ventricle near the left descending artery (LAD), as seen in Figure 3.8.

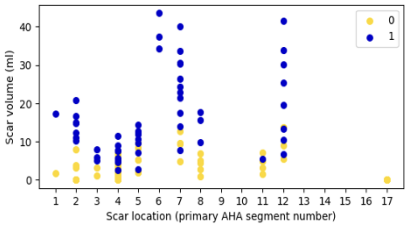

Artery territory	Left anterior descending artery (LAD)	Right coronary artery (RCA)	Left circumflex artery (LCX)
AHA segments	1,2,7,8,14,13,17	3,4,9,10,15	5,6,11,12,16
Number of cases	45	50	34
Number of cases with re-entry	22	11	20
Percentage of cases with re-entry (%)	48.9	22.0	58.9

Fig. 3.8: (left) Distribution of re-entry occurrences in 129 simulated ventricular activation sequences. Presence and absence of re-entry are indicated by 1 and 0, respectively. The scar location is defined using the AHA segment corresponding to the highest scar volume present. (right) Summary of re-entry occurrences and frequency in related arteries.

Our model was trained to perform binary classification on the labelled cases provided. The training time for 104 cases was 1 minute and 37s. When evaluated on the 25 test cases, the trained model had an accuracy of 88.0% and the F1 score was 48.0%. The trained model predicted the outcome of a single case in 0.01 seconds.

3.4 Discussion

In this project, we have presented a novel approach for biventricular mesh generation and rapid arrhythmic risk assessment in post-infarction patients. Our work contributes as an improvement of the [14] work in a variety of ways.

A comprehensive workflow was employed for the processing and preparation of cardiac imaging data, with the ultimate goal of creating patient-specific 3D models of the ventricles. Several key steps and methodologies were applied to achieve this. Automated contour generation for the LV with the software ADAS demonstrated high accuracy with minimal manual adjustments, while manual segmentation was applied to the RV. Refinement of extracted contours, unified surface mesh generation, and the incorporation of realistic cardiac muscle fiber information contribute to the creation of a detailed 3D model.

Various augmentation techniques were introduced to enhance the characterization of scar tissue within the LV. These techniques not only improve the precision of scar modeling but also enable the exploration of diverse scar geometries for in depth analysis. Firstly, the scar tissue within the LV was characterized using the FWHM threshold method. To diversify the scar geometries, three distinct scar configurations were generated for each LGE MRI scan. Secondly, to further enrich the scar

population within each mesh, an innovative artificial scar generation algorithm was developed.

As a result, our innovative mesh generation pipeline successfully produced a diverse array of patient-specific biventricular meshes featuring realistic scar geometries, thereby providing valuable assets for assessing risk of arrhythmia through mechanistic EP simulations. Due to time constraints, we weren't able to complete the simulations for all biventricular populations. Instead, we used the already present data of [14] for the arrhythmic risk prediction model.

Our predictive model was able to classify reentry events with a high accuracy, but a low F1 score, which may be due to the small size of the dataset. The architecture of the model was designed to account for this by including relatively few trainable parameters. However, the model may still struggle to learn these parameters correctly given the limited number of training samples. The small number of input features extracted from the dataset may be another potential limitation. We believe that the model performance would improve when applied to a larger, richer dataset. Additionally, the structure of the proposed model makes it readily extendable to predict the location of reentries by performing classification at node-level instead of at graph-level.

Despite its limitations, our model was able to predict the outcome-of-interest significantly faster than the original numerical simulations. Typically, one EP simulation can take upwards of 5 hours to complete for a single patient, using approaches and computational resources similar to the ones used in [14]. In contrast, our GCN model was able to predict presence of arrhythmia in just 0.01 seconds. This improvement in prediction time represents a speed-up of over five orders of magnitude. This is particularly significant in clinical settings, where decision-making may be time sensitive and powerful HPC resources may not be available. Furthermore, rapid prediction times may also be advantageous in further computational studies, by generating large populations of virtual cases with the aim to investigate parameter inference and explore trends in cohorts of healthy and diseased patients [28, 29].

In conclusion, we presented a novel cardiac meshing pipeline and ML-based predictive model to determine risk of arrhythmia in post-MI patients. Our pipeline allowed for reconstruction of personalised and physiologically accurate 3D meshes of the human ventricles based on 2D LGE MRI scans. Using the patient-specific biventricular meshes, we simulated electrical propagation on the ventricles, and determined risk of arrhythmia due to reentry. Our predictive model was able to learn from the mechanistic simulations and significantly accelerate prediction times. This work paves the way towards more accurate and faster computational methods for arrhythmic risk stratification, helping to improve therapeutic strategies and long-term outcomes of post-MI patients.

3.5 Acknowledgements

This work was partly supported by the Research Council of Norway (303178, 309762). Simulations were performed on resources provided by Sigma2 - the National Infrastructure for High Performance Computing and Data Storage in Norway.

References

1. DM Henkel, BJ Witt, BJ Gersh, SJ Jacobsen, SA Weston, RA Meverden, and VL Roger. Ventricular arrhythmias after acute myocardial infarction: a 20-year community study. Am Heart J, 151(4):806–812, 2006.
2. DP Zipes and HJ Wellens. Sudden cardiac death. Circulation, 98:2334–2351, 1998.
3. Yao Sun and Karl T. Weber. Infarct scar: a dynamic tissue. Cardiovascular Research, 46(2):250–256, 05 2000.
4. William G Stevenson. Ventricular scars and ventricular tachycardia. Transactions of the American Clinical and Climatological Association, 120:403, 2009.
5. I Kazbanov, K ten Tusscher, and A Panfilov. Effects of heterogeneous diffuse fibrosis on arrhythmia dynamics and mechanism. Sci Rep, 6:20835, 2016.
6. F Leyva, A Zegard, O Okafor, and et al. Model-based feature augmentation for cardiac ablation target learning from images. J Am Coll Cardiol, 79:665–678, 2022.
7. Thao P Nguyen, Zhilin Qu, and James N Weiss. Cardiac fibrosis and arrhythmogenesis: the road to repair is paved with perils. Journal of molecular and cellular cardiology, 70:83–91, 2014.
8. Zachary Goldberger and Rachel Lampert. Implantable cardioverter-defibrillators: expanding indications and technologies. JAMA, 295(7):809–818, 2006.
9. Douglas S Lee, Andrew D Krahn, Jeffrey S Healey, David Birnie, Eugene Crystal, Paul Dorian, Christopher S Simpson, Yaariv Khaykin, Douglas Cameron, Amir Janmohamed, et al. Evaluation of early complications related to de novo cardioverter defibrillator implantation: insights from the ontario icd database. Journal of the American College of Cardiology, 55(8):774–782, 2010.
10. Hermenegild Arevalo, Gernot Plank, Patrick Helm, Henry Halperin, and Natalia Trayanova. Tachycardia in post-infarction hearts: insights from 3d image-based ventricular models. PloS one, 8(7):e68872, 2013.
11. Hermenegild J Arevalo, Fijoy Vadakkumpadan, Eliseo Guallar, Alexander Jebb, Peter Malamas, Katherine C Wu, and Natalia A Trayanova. Arrhythmia risk stratification of patients after myocardial infarction using personalized heart models. Nature communications, 7(1):11437, 2016.
12. Natalia A Trayanova. Learning for prevention of sudden cardiac death, 2021.
13. AK Feeny, MK Chung, A Madabhushi, et al. Artificial intelligence and machine learning in arrhythmias and cardiac electrophysiology. circ arrhythm electrophysiol 13 (8): e7952, 2020.
14. Mary M Maleckar, Lena Myklebust, Julie Uv, Per Magne Florvaag, Vilde Strøm, Charlotte Glinge, Reza Jabbari, Niels Vejlstrup, Thomas Engstrøm, Kiril Ahtarovski, et al. Combined in-silico and machine learning approaches toward predicting arrhythmic risk in post-infarction patients. Frontiers in Physiology, 12:745349, 2021.
15. D Dalton, H Gao, and D Husmeier. Emulation of cardiac mechanics using graph neural networks. Computer Methods in Applied Mechanics and Engineering, 401:115645, 2022.
16. Natalia A Trayanova, Dan M Popescu, and Julie K Shade. Machine learning in arrhythmia and electrophysiology. Circulation research, 128(4):544–566, 2021.
17. RC Lozoya, B Berte, H Cochet, P Jais, N Ayache, and M Sermesant. Model-based feature augmentation for cardiac ablation target learning from images. IEEE Trans Biomed Eng, 66:30–40, 2019.

18. Christophe Geuzaine and Jean-François Remacle. Gmsh: A 3-d finite element mesh generator with built-in pre-and post-processing facilities. International journal for numerical methods in engineering, 79(11):1309–1331, 2009.
19. Jason D Bayer, Robert C Blake, Gernot Plank, and Natalia A Trayanova. A novel rule-based algorithm for assigning myocardial fiber orientation to computational heart models. Annals of biomedical engineering, 40:2243–2254, 2012.
20. Gernot Plank, Axel Loewe, Aurel Neic, Christoph Augustin, Yung-Lin Huang, Matthias A.F. Gsell, Elias Karabelas, Mark Nothstein, Anton J. Prassl, Jorge Sánchez, Gunnar Seemann, and Edward J. Vigmond. The opencarp simulation environment for cardiac electrophysiology. Computer Methods and Programs in Biomedicine, 208:106223, 2021.
21. Aurel Neic, Matthias A.F. Gsell, Elias Karabelas, Anton J. Prassl, and Gernot Plank. Automating image-based mesh generation and manipulation tasks in cardiac modeling workflows using meshtool. SoftwareX, 11:100454, 2020.
22. Zhisong Fu, Robert M Kirby, and Ross T Whitaker. A fast iterative method for solving the eikonal equation on tetrahedral domains. SIAM Journal on Scientific Computing, 35(5):C473–C494, 2013.
23. M Cerqueira, N Weissman, V Dilsizian, A Jacobs, S Kaul, W Laskey, D Pennell, J Rumberger, T Ryan, and M Verani. Standardized myocardial segmentation and nomenclature for tomographic imaging of the heart. Circulation, 105:539–542, 2002.
24. Kirsten HWJ Ten Tusscher and Alexander V Panfilov. Alternans and spiral breakup in a human ventricular tissue model. American Journal of Physiology-Heart and Circulatory Physiology, 291(3):H1088–H1100, 2006.
25. R. Coronel, F. J. Wilms-Schopman, L. R. Dekker, and M. J. Janse. Heterogeneities in [k+]o and tq potential and the inducibility of ventricular fibrillation during acute regional ischemia in the isolated perfused porcine heart. Circulation, 92:120–129, 1995.
26. Thomas N. Kipf and Max Welling. Semi-supervised classification with graph convolutional networks, 2017.
27. Diederik P. Kingma and Jimmy Ba. Adam: A method for stochastic optimization, 2017.
28. S.A. Niederer, Y Aboelkassem, C.D. Cantwell, C Corrado, S Coveney, E.M. Cherry, T Delhaas, Fenton F.H., A.V. Panfilov, P Pathmanathan, G Plank, M Riabiz, C.H. Roney, R.W. Dos Santos, and L Wang. Creation and application of virtual patient cohorts of heart models. Philos Trans A Math Phys Eng Sci, 378(2173):20190558, 2020.
29. S. A. Niederer, M. S. Sacks, M Girolami, and K Willcox. Scaling digital twins from the artisanal to the industrial. Nat Comput Sci, 1(5):313–320, 2021.

Chapter 4
Non-Invasive Detection of Fetal Ischemia Through Electrocardiography

Álvaro José Bocanegra Pérez, Matthew J Magoon, Manisha Sahota, Leonie Schicketanz, Julie J Uv, Patrick M Boyle, and Hermenegild J Arevalo

Abstract During pregnancy, fetal distress requiring clinical intervention can be difficult to accurately monitor and diagnose, necessitating technological improvements to bring clear information to patients and their care teams. Non-invasive fetal Electrocardiography (NI-fECG) monitoring may allow for earlier and more reliable detection of global cardiac ischemia due to hypoxia. However, the low signal-to-noise ratio of the fetal heartbeat relative to the maternal heartbeat remains a challenge. To enable reliable recognition of ischemia in NI-fECG, we propose an approach that combines simulating a pregnant torso and an unsupervised machine-learning method. Three stages of fetal cardiac ischemia: none (healthy), moderate, and severe, were introduced to the model. For each case, Electrocardiograms (ECGs) were simulated with the standard 12 leads, plus 3 additional abdominal leads. Unsupervised Multiple-Kernel Learning (MKL) with k-means clustering identified changes consistent with fetal cardiac ischemia despite noise from the parental heart. Thus, in

Álvaro José Bocanegra Pérez
Sensing in Physiology and Biomedicine (Physense), Universitat Pompeu Fabra, ES

Matthew J Magoon
Department of Bioengineering, University of Washington, USA

Manisha Sahota
Department of Biomedical Engineering, King's College London, UK

Leonie Schicketanz
Institute of Biomedical Engineering, Karlsruhe Institute of Technology, DE

Julie J Uv
Department of Computational Physiology, Simula Research Laboratory, NO

Patrick M Boyle
Department of Bioengineering, University of Washington, USA; Institute for Stem Cell and Regenerative Medicine, University of Washington, USA; Center for Cardiovascular Biology, University of Washington, USA

Hermenegild J Arevalo (corresponding author)
Department of Computational Physiology, Simula Research Laboratory, NO e-mail: hermenegild@simula.no

K. J. McCabe (ed.), *Computational Physiology*, Simula SpringerBriefs on Computing 17,
https://doi.org/10.1007/978-3-031-53145-3_4

this early proof-of-concept investigation, our results suggest that NI-fECG may offer a means for detecting global cardiac ischemia.

4.1 Introduction

The most common techniques for monitoring fetal distress in clinical practice are single hand-held Doppler ultrasound or Cardiotocography (CTG) which provide information about the Fetal Heart Rate (FHR). However, Doppler ultrasound techniques cannot provide estimates of Fetal Heart Rate Variability (FHRV) and the accuracy of FHR estimates is technically limited by factors such as low sampling frequency and imprecise alignment with the fetal heart. Due to the lack of robustness of FHR monitoring, Caesarean deliveries are often performed with limited evidence of reducing adverse long-term neonatal outcomes [1].

Recent studies have highlighted the potential of fetal Electrocardiography (fECG) in providing a more reliable assessment of fetal distress. Currently, fECG is obtained via a scalp electrode which is directly attached to the fetal scalp [2]. As this procedure is invasive and requires the amniotic membrane to be ruptured, it is not routinely performed. Non-Invasive fetal ECG (NI-fECG) provides an alternative approach for continuous *in-utero* fetal monitoring with negligible risk to the parent and fetus, as it only requires skin-contact electrodes on the parent's skin to obtain information about fetal cardiac activity [3]. Analysis of ECG waveforms is routinely performed in clinical practice to provide information about cardiac function in adults. However, interpretation of NI-fECG is more challenging due a lack of standardisation of NI-fECG acquisition protocols and low signal-to-noise ratios in abdominal ECGs due to signal interference from the parental heart, small fetal myocardial volumes and parental and fetal motion artefacts [4].

Consequently, sophisticated post-processing techniques are required to extract the NI-fECG from the abdominal signal mixture. Common NI-fECG extraction techniques include adaptive filtering [5, 6, 7, 8, 9], Kalman filtering [10, 11, 12] and wavelet transform [13, 14]. Furthermore, blind source separation is a technique that leverages principle component analysis (PCA) and independent component analysis (ICA) to separate the mixture of independent signals in the abdominal ECG [15, 16, 17]. Further NI-fECG extraction techniques include template subtraction which involves subtracting a synthetic parental ECG which is generated by using parental QRS complex estimates from the abdominal signal to create a template parental ECG [18, 19, 20, 21, 22, 23]. While effective for single-channel ECG denoising, NI-fECG extraction techniques are significantly limited by the need for precise parental QRS complex detection, which is challenging in the case where the parental and fetal R wave temporally overlap [24].

Deep neural networks have recently emerged as an alternative NI-fECG extraction approach [25] with several studies proposing deep convolution encoder-decoder network implementations to extract the NI-fECG from the abdominal signal mixture [26, 27, 28, 29]. However, there are many challenges of such deep learning based

methods. Such challenges include training the model to directly extract the NI-fECG due to it being significantly weaker than the parental ECG as well as the contamination of the extracted NI-fECG with the residual parental ECG which makes identification of the P and T waves challenging. Moreover, the lack of gold-standard training data and NI-fECG databases that can be used to evaluate NI-fECG extraction algorithms may hinder the robustness and generalisation performance of the model[30].

An additional approach to analysing ECG signals through the use of artificial intelligence is unsupervised machine learning, which enables the analysis of the natural distribution of the data. Due to the complexity of data sets, unsupervised machine learning is often used in conjunction with dimensionality reduction techniques to allow the number of dimensions of a set of inputs to be reduced while preserving the information provided. Principal component analysis (PCA) is the most commonly used dimensionality reduction technique [31]. However, when working with clinical data it can fall short, as it is monovariate and linear. Other techniques, such as Multiple Kernel Learning (MKL) have been used to analyse biological signals as a multivariate and non-linear alternative [32, 33, 34].

In clinical practice, monitoring of the ST segment in adult 12 lead ECGs is commonly performed to diagnose myocardial ischemia [35]. ST segment analysis has additionally been identified as a marker of fetal distress due to hypoxia [36, 37]. However, use of fetal ST analysis remains limited as it is currently carried out using invasive fetal scalp electrodes. Notably, Clifford *et al.* compared the FHR and ST deviation derived from fetal scalp electrode data and non-invasive abdominal electrodes, highlighting their clinical similarity [38]. This provides an opportunity to leverage computational cardiac electrophysiology to acquire synthetic NI-fECGs and develop machine learning techniques to enhance detection of ST segment deviation indicative of fetal ischemia, which could improve clinical decision-making regarding when a Caesarean section should be performed to optimise parental and fetal outcomes. Herein, we performed fetal and parental cardiac electrophysiology simulations using an image-based finite element model of a pregnant torso to acquire realistic simulated NI-fECGs in healthy and diseased conditions to determine the extent to which we can detect fetal ischemia.

4.2 Methods

To generate a data set, 10 simulations were conducted with openCARP [39] followed by a machine-learning based approach to characterise ischemia in the NI-fECG.

4.2.1 Geometrical Mesh Construction

In this study, the geometrical mesh of a pregnant torso developed by Uv *et al.* [4] was used. Briefly, a CT-based cardiac biventricular geometry [40] was combined with an MRI-based whole body pregnant model [41] to represent the parental and fetal hearts embedded in an anatomical pregnant torso. The parental heart was scaled, translated and rotated to obtain the fetal heart. The epicardial, myocardial and endocardial layers were defined as 30%, 25% and 45% of the cardiac wall thickness respectively [42]. Myocardial fibre orientations were assigned to the model using a previously validated rule-based method [43].

4.2.2 Electrophysiological Modelling

4.2.2.1 Ionic Models

The ten Tusscher model of the human ventricular myocyte was used to determine the ionic current properties of the parental heart [44]. For the fetal heart, the ionic model was modified to reflect increasing ischemic levels in three stages: healthy, moderate and severe ischemia. Table 4.1 presents how the default properties were changed following the work presented in [45]. For the fetal epicardial, mid-myocardial and endocardial layers, the membrane transient outward conductance g_{to} was set to 0.073 Sm^{-1} [3].

In the myocardium, the intracellular and extracellular conductivities were set to $g_i = (0.27, 0.081, 0.045)\ Sm^{-1}$ and $g_e = (0.9828, 0.3654, 0.3654)\ Sm^{-1}$ in the longitudinal, transverse and normal directions respectively and the torso was given an isotropic conductivity of 0.216 Sm^{-1} [3]. Tissue propagation was modelled with the monodomain approach.

Table 4.1: Summary of the parameters of the ten Tusscher ionic model of the human ventricular myocyte [44] modified to simulate healthy, moderate and severe ischemia in the fetal endocardial layer.

Cell Model Parameters	Healthy	Moderate Ischemia	Severe Ischemia
$[K^+]_o\,(mmol/l)$	5.4	12.5	15.0
$g_{Na}, g_{Ca,L}\,(\%)$	100	75	50
$P_{NaK}\,(\%)$	100	100	30
$k_{NaCa}\,(\%)$	100	100	20
$V_{maxup}\,(\%)$	100	100	90
$V_{rel}\,(\%)$	100	100	5

4.2.2.2 Stimulation Protocol

Both the fetal and parental heart were stimulated following the protocol proposed by Durrer *et al.* [46]. For all simulations, the parental heartbeat was set to a cycle length of 667 ms, which corresponds to a healthy adult heartbeat during the second trimester of 90 bpm [47]. For the fetal heart, simulations for the following different heart cycle lengths (heart rates) were conducted: 462 ms (130 bpm), 400 ms (150 bpm), 353 ms (170 bpm). For a gestational age over 32 weeks, these heart rates correspond to the range of normal fetal heart rates between 110–160 bpm [48].

4.2.3 Extracellular Potential Measurements

The extracellular potentials were recovered in a post-processing step with openCARP at the electrode locations defined in Figure 4.1. The four limb and six precordial electrodes match the standard electrode positions to calculate the 12 lead ECG. Figure 4.1 also illustrates the calculation of three abdominal leads derived from electrode positions from previous work [4].

Since the extraction of the NI-fECG without distorting its waveform morphology is an unsolved problem, an ECG showing only fetal activity was required. Hence, we assumed that the simulation results with mixed activity from the parental and fetal heart could be obtained approximately by superimposing simulations results where only one heart was active at a time. To obtain a pure fetal signal, simulations where only the parental heart was active were performed and subtracted from simulation results with parental and fetal cardiac activity.

To investigate how sensitive our proposed analysis protocol was to inadequately extract NI-fECGs, we developed a method to linearly suppress the parental activities in the abdominal recordings. Accordingly, chest and abdominal leads were scaled and subtracted from each other, using only leads that captured the parental activity in the same direction, e.g. leads A52 and aVF from the 12 lead ECG.

4.2.3.1 Simulation Setup

By changing the fetal heart rate and inducing three stages of increasing ischemia in the fetal heart, nine simulation sets of 5 s recordings were generated. To reduce overall computation time, a simulation where only the parental heart was active was conducted to retrieve the pure fetal signal for all nine cases.

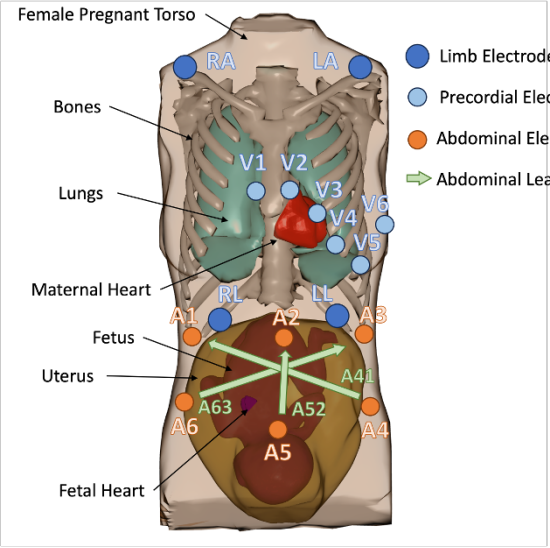

Fig. 4.1: Visualisation of the pregnant torso model illustrating the electrode positions and the calculated abdominal leads.

4.2.4 ECG Signal Analysis

Since NI-fECGs are complex signals with multiple sources (leads) aligned in time, we applied unsupervised machine learning analysis to a dimensionality reduced space to determine whether we could differentiate between healthy and ischemic cases in the NI-fECGs. Using an analysis pipeline adapted from the work by Jimenez-Perez *et al.* [49], we firstly used a delineation deep learning network [50] to identify the QRS-complexes, T-waves, and ST-segments in all the leads of the different simulated NI-fECGs. Secondly, we applied MKL on the data set to generate the dimensionality reduced space. Finally, we perform a clustering analysis, characterising every cluster to determine the discriminative power of the method.

4.2.4.1 Signal Delineation

The used ECG delineation network enabled the segmentation of biomarkers that we considered relevant for this problem. Separating the NI-fECG from the parental ECG was outside of the scope of this project. However, since our goal was to analyse the NI-fECG morphology, we applied the delineation network on the pure NI-fECG which only shows fetal cardiac activity. Following this, the mask was applied to the original signal in which both fetal and maternal hearts were active. Therefore, the ideal segmentation enabled the focus of the analysis to remain on the discrimination capacity of our solution.

4.2.4.2 Dimensionality Reduction

To increase the number of cases in the dataset, we treated each cardiac cycle as a separate record. Since the simulations used biventricular geometries, no P wave was generated. Hence, the start of the cardiac cycle was taken as the beginning of the QRS complex and the end of the cardiac cycle was marked at the end of the T wave. All segments were then resampled to be of the same length and aligned to allow the MKL algorithm to generate the reduced dimensionality space.

4.2.4.3 Cluster Analysis

K-means clustering was used to partition the data into clusters to determine if underlying differences between the healthy, moderately ischemic and severely ischemic NI-fECG could be detected. The number of clusters was determined using the silhouette method [51], which allowed us to choose the number of clusters that best separates the data.

4.3 Results

4.3.1 Simulation Results

From each simulation a 15 lead ECG was constructed containing data from the standard 12 lead ECG with 3 additional abdominal leads: A41, A52, and A63 (Figure 4.2). Ideal NI-fECGs were constructed by subtracting the known parental contribution from each lead. However, the actual raw signals from our model include substantially more contribution from the parental heart than the fetal heart, obscuring even dramatic changes to the ST segment and T wave. Application of a simple linear method to suppress the signal from the parental heart enabled the visualisation of ischemic changes in the NI-fECG signal, although this still failed to reproduce the ideal signals (Figure 4.3).

4.3.2 Signal Analysis

The delineation network was applied on the pure NI-fECG signal and the mask of the onsets was applied on the original signal, which is contaminated with the parental ECG. Results for a single lead are shown in Figure 4.4. The biomarkers chosen for the analysis were the QRS complexes (in red), T waves (in blue) and the ST segments (the interval between the end of each QRS complex and the beginning of the T wave).

Each cardiac cycle was considered as a single input for the MKL method. After aligning the cycles, each segment was interpolated to a fixed value of samples,

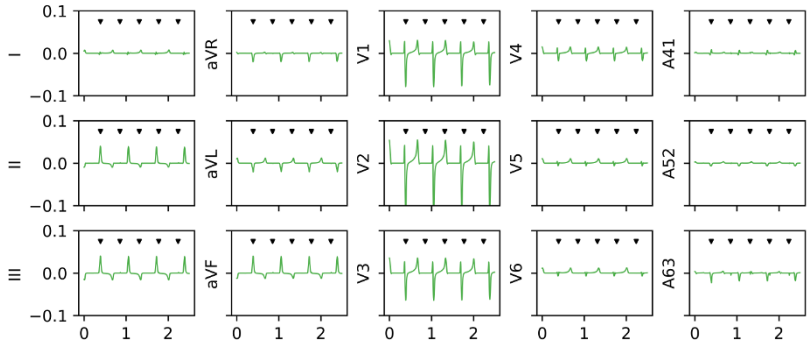

Fig. 4.2: Simulated 15 lead ECG of a healthy fetus with a heart rate of 130 bpm. Note, the fetal contribution is by the parental heartbeat, even in the abdominal leads A41, A52, and A63. Arrows indicate the beginning of each fetal heartbeat.

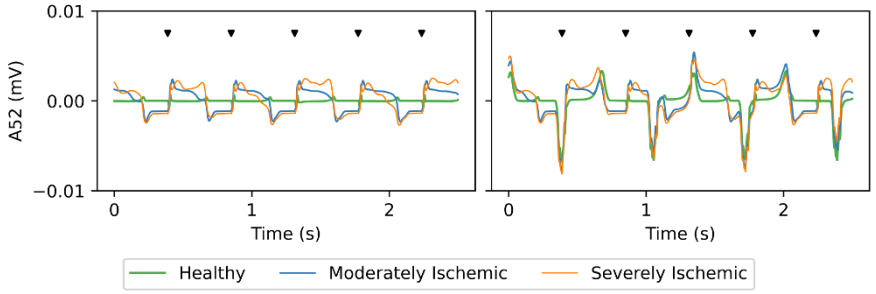

Fig. 4.3: Example of a healthy, moderately ischemic, and severely ischemic fetal heartbeat at 130 bpm. The parental heartbeat was removed ideally (left) and by a simple linear suppression technique (right). Arrows indicate the beginning of each fetal heartbeat.

allowing the database to be stored in an array. Finally, the MKL algorithm is applied on the data set to generate the output space. This process was applied to the data set of ideal abdominal ECGs where only the fetal heart was active as well as to the original abdominal ECG where the parental cardiac activity was suppressed. Figure 4.5 shows the output space for each case following dimensionality reduction.

The output of the MKL algorithm has $N - 1$ dimensions, where N represents the number of inputs or records. However, the highest variability is concentrated in the first dimension. For the clustering analysis, we considered the dimensions that accumulated 95% of the variability of the output space.

To cluster these results, the output space served as an input for the k-means algorithm. The number of clusters was decided by using the silhouette method leading to an optimum number of clusters between 3 and 16. From the simulations, it was known whether a data point corresponded to healthy, moderately ischemic, or

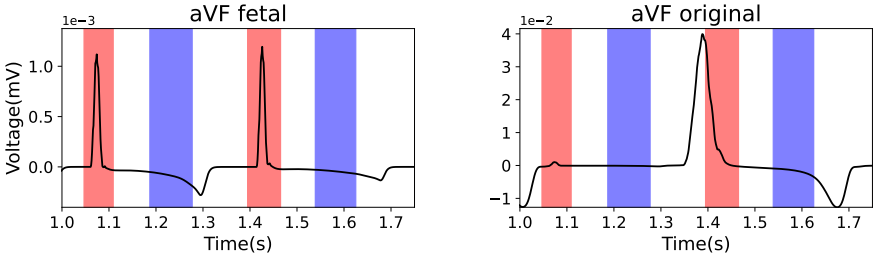

Fig. 4.4: Segmented ECGs for the ideally isolated NI-fECG (left) and the original NI-fECG (right) which includes the parental and fetal cardiac activity. The segments for the QRS complex (red) and the ST segment (blue) are detected in the isolated NI-fECG (left) and are applied to the original NI-fECG (right), both from the aVF lead in this case.

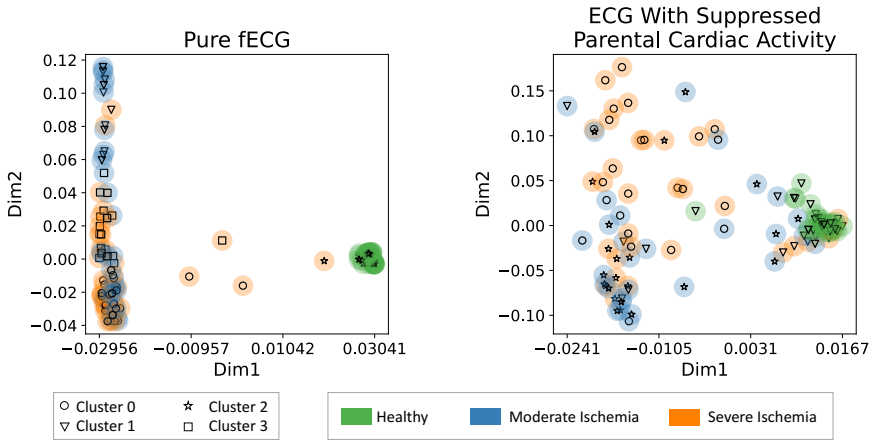

Fig. 4.5: Output spaces for the different ischemic levels from the abdominal ECG leads showing only fetal cardiac activity (left) and showing the original ECG after applying the parental suppression method (right). The markers indicate the cluster to which each point belongs, revealing four different clusters detected for the data set displayed on the left and three clusters detected for the data set on the right.

severely ischemic data. Using this information, Figure 4.5 illustrates the distribution of the different cases in the output space, highlighting the ability of the proposed method in distinguishing the three levels of ischemia. For each level of ischemia, the total number of records within each cluster was also computed, as summarised in Figure 4.6. From this, it is evident that healthy data points are mostly assigned to the same cluster. Data based on the original abdominal ECG with parental suppression

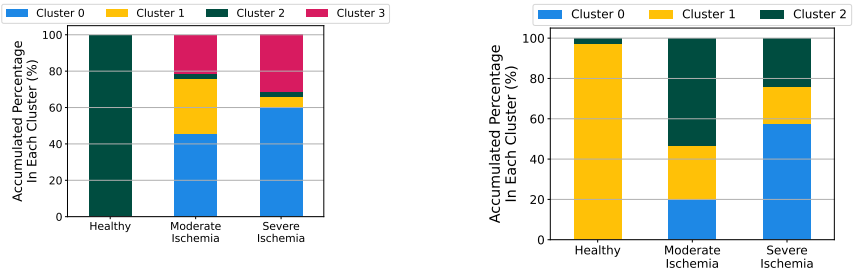

Fig. 4.6: Summary of the distribution of the data points across all clusters based on the abdominal lead recordings with only fetal cardiac activity (Left) and on the original abdominal ECG after applying the parental suppression method (Right). Each coloured bar indicates the percentage of data points assigned to a specific cluster for each ischemic level.

is more likely to be assigned to the cluster that is mostly associated with healthy data points than data based on the pure NI-fECG. Differentiating between moderately and severely ischemic NI-fECGs based on the cluster allocation is ambiguous for both data sets.

4.4 Discussion

The proposed model framework successfully generated synthetic abdominal ECGs containing signal contributions from both the parent and fetus. Moreover, a simple linear NI-fECG extraction method was implemented to suppress the parental signal, allowing dramatic ST segment changes to be identified in the ischemic fetus. In addition, the feasibility of using common machine learning techniques such as MKL for dimensionality reduction and k-means clustering to analyse the ECG signals was demonstrated, providing qualitative and quantitative evidence of distinct clusters describing the degree of fetal ischemia.

Due to the high computational cost of performing whole torso electrophysiology simulations, only monodomain simulations were performed in this preliminary investigation. Furthermore, the torso was modelled as a uniform medium hence varying tissue conductivities that affect the wavefront propagation were not considered. Performing bidomain simulations and accounting for additional tissue types such as bone, lungs and the fetal vernix caseosa would provide more realistic conduction throughout the torso and thus, more realistic ECGs. Notably, the Paniflov ten Tusscher ionic model used in this study was adapted to model fetal ischemia using data based on an adult human heart. Modifying the ionic model to reflect the ischemic fetal heart would be important to obtain more clinically realistic NI-fECG signals. Moreover, as this was a preliminary investigation, we focused on modelling severe is-

chemia only in the endocardial layer of the fetal heart to ensure the ischemic changes were sufficiently large to detect a change in the NI-fECG. Future studies simulating lower levels of ischemia in the whole fetal heart would present a more clinically relevant scenario in which the fetus would have a greater chance of resuscitation. While the pipeline developed in this study presents a promising proof-of-concept, using a simple linear method to suppress the parental heart signal is not realistic for clinical settings. NI-fECG extraction remains a challenging problem, therefore as NI-fECG extraction algorithms continue to evolve and improve in the future, techniques should be validated using real clinical data and incorporated into the workflow developed in this study to enhance the robustness of this proposed method.

4.5 Conclusions

We developed, to our knowledge, a novel workflow to detect fetal ischemia by simulating parental and fetal cardiac electrophysiology in a pregnant torso model and using MKL with k-means clustering to identify ischemic changes in signals with amplified fetal contribution. With continued development and further optimisation, our methodology may enable improved detection of fetal cardiac ischemia to better inform clinical decision-making. In future work, the pipeline will be applied to additional pregnant torso models with lower levels of ischemia applied globally to the fetal heart to better characterise fetal distress non-invasively. Additionally, the impact of incorporating time-dependent factors such as fetal movement and physiological artefacts due to parental respiration and muscle contraction should be explored.

4.6 Acknowledgements

This work was partly supported by the Kunnskapsdepartementet and the Norwegian Research Council (303178). Research reported in this brief was also partially supported by the United States' National Institute of General Medical Sciences of the National Institutes of Health of the National Institutes of Health under award number T32GM007266, to MJM. Simulations were performed on resources provided by Sigma2 - the National Infrastructure for High Performance Computing and Data Storage in Norway. This work was also facilitated through the use of advanced computational, storage, and networking infrastructure provided by the Hyak supercomputer system at the University of Washington. The content is solely the responsibility of the authors and does not necessarily represent the official views of the National Institutes of Health.

References

1. Zarko Alfirevic, Gillian ML Gyte, Anna Cuthbert, and Declan Devane. Continuous cardiotocography (ctg) as a form of electronic fetal monitoring (efm) for fetal assessment during labour. Cochrane database of systematic reviews, (2), 2017.
2. Jr Charles A Hunter, Robert J Braunlin, Kenneth G Lansford, and Suzanne B Knoebel. Method for obtaining a fetal electrocardiogram, February 4 1964. US Patent 3,120,227.
3. Eleftheria Pervolaraki, Sam Hodgson, Arun V Holden, and Alan P Benson. Towards computational modelling of the human foetal electrocardiogram: normal sinus rhythm and congenital heart block. Europace, 16(5):758–765, 2014.
4. Julie J Uv and Hermenegild Arevalo. Electrophysiological simulation of maternal-fetal ecg on a 3d maternal torso model. In 2022 Computing in Cardiology (CinC), volume 498, pages 1–4. IEEE, 2022.
5. Radek Martinek, Radana Kahankova, Homer Nazeran, Jaromir Konecny, Janusz Jezewski, Petr Janku, Petr Bilik, Jan Zidek, Jan Nedoma, and Marcel Fajkus. Non-invasive fetal monitoring: A maternal surface ecg electrode placement-based novel approach for optimization of adaptive filter control parameters using the lms and rls algorithms. Sensors, 17(5):1154, 2017.
6. Eleni Fotiadou, Judith OEH Van Laar, S Guid Oei, and Rik Vullings. Enhancement of low-quality fetal electrocardiogram based on time-sequenced adaptive filtering. Medical & biological engineering & computing, 56:2313–2323, 2018.
7. Abdullah Mohammed Kaleem and Rajendra D Kokate. An efficient adaptive filter for fetal ecg extraction using neural network. Journal of Intelligent Systems, 28(4):589–600, 2019.
8. Shuicai Wu, Yanni Shen, Zhuhuang Zhou, Lan Lin, Yanjun Zeng, and Xiaofeng Gao. Research of fetal ecg extraction using wavelet analysis and adaptive filtering. Computers in biology and medicine, 43(10):1622–1627, 2013.
9. Manuja Sharma, Peter Ritchie, Tadesse Ghirmai, Hung Cao, and Michael PH Lau. Unobtrusive acquisition and extraction of fetal and maternal ecg in the home setting. In 2017 IEEE SENSORS, pages 1–3. IEEE, 2017.
10. Rik Vullings, Bert De Vries, and Jan WM Bergmans. An adaptive kalman filter for ecg signal enhancement. IEEE transactions on biomedical engineering, 58(4):1094–1103, 2010.
11. M Suganthy and S Manjula. Enhancement of snr in fetal ecg signal extraction using combined swt and wlsr in parallel ekf. Cluster Computing, 22(Suppl 2):3875–3881, 2019.
12. Fernando Andreotti, Maik Riedl, Tilo Himmelsbach, Daniel Wedekind, Sebastian Zaunseder, Niels Wessel, and Hagen Malberg. Maternal signal estimation by kalman filtering and template adaptation for fetal heart rate extraction. In Computing in Cardiology 2013, pages 193–196. IEEE, 2013.
13. S Hema Jothi and K Helen Prabha. Fetal electrocardiogram extraction using adaptive neuro-fuzzy inference systems and undecimated wavelet transform. IETE Journal of Research, 58(6):469–475, 2012.
14. Radek Martinek, Radana Kahankova, Jan Nedoma, Marcel Fajkus, and Kristyna Cholevova. Fetal ecg preprocessing using wavelet transform. In Proceedings of the 10th International Conference on Computer Modeling and Simulation, pages 39–43, 2018.
15. Dharmendra Gurve, Jeevan K Pant, and Sridhar Krishnan. Real-time fetal ecg extraction from multichannel abdominal ecg using compressive sensing and ica. In 2017 39th Annual International Conference of the IEEE Engineering in Medicine and Biology Society (EMBC), pages 2794–2797. IEEE, 2017.
16. A Karimi Rahmati, SK Setarehdan, and BN Araabi. A pca/ica based fetal ecg extraction from mother abdominal recordings by means of a novel data-driven approach to fetal ecg quality assessment. Journal of biomedical physics & engineering, 7(1):37, 2017.
17. Radek Martinek, Radana Kahankova, Janusz Jezewski, Rene Jaros, Jitka Mohylova, Marcel Fajkus, Jan Nedoma, Petr Janku, and Homer Nazeran. Comparative effectiveness of ica and pca in extraction of fetal ecg from abdominal signals: Toward non-invasive fetal monitoring. Frontiers in physiology, 9:648, 2018.

18. Mihaela Ungureanu, Johannes WM Bergmans, Swan Guid Oei, and Rodica Strungaru. Fetal ecg extraction during labor using an adaptive maternal beat subtraction technique. 2007.
19. Maurizio Varanini, G Tartarisco, L Billeci, A Macerata, G Pioggia, and R Balocchi. An efficient unsupervised fetal qrs complex detection from abdominal maternal ecg. Physiological measurement, 35(8):1607, 2014.
20. Sebastian Zaunseder, Fernando Andreotti, Marcos Cruz, Holger Stepan, Claudia Schmieder, Hagen Malberg, Alexander Jank, and Niels Wessel. Fetal qrs detection by means of kalman filtering and using the event synchronous canceller. In Proceedings of the 7th International Workshop on Biosignal Interpretation, Como, Italy, pages 2–4, 2012.
21. Joachim Behar, Julien Oster, and Gari D Clifford. Combining and benchmarking methods of foetal ecg extraction without maternal or scalp electrode data. Physiological measurement, 35(8):1569, 2014.
22. Kwang Jin Lee and Boreom Lee. Sequential total variation denoising for the extraction of fetal ecg from single-channel maternal abdominal ecg. Sensors, 16(7):1020, 2016.
23. He Liu, Deyun Chen, and Guanghao Sun. Detection of fetal ecg r wave from single-lead abdominal ecg using a combination of rr time-series smoothing and template-matching approach. IEEE Access, 7:66633–66643, 2019.
24. Reza Sameni. Extraction of Fetal Cardiac Signals from an Array of Maternal Abdominal Recordings. PhD thesis, 07 2008.
25. Abdullah Mohammed Kaleem and Rajendra D Kokate. A survey on fecg extraction using neural network and adaptive filter. Soft Computing, 25:4379–4392, 2021.
26. Wei Zhong, Lijuan Liao, Xuemei Guo, and Guoli Wang. Fetal electrocardiography extraction with residual convolutional encoder–decoder networks. Australasian physical & engineering sciences in medicine, 42:1081–1089, 2019.
27. Qinghua Guo, Shichao Jin, Min Li, Qiuli Yang, Kexin Xu, Yuanzhen Ju, Jing Zhang, Jing Xuan, Jin Liu, Yanjun Su, et al. Application of deep learning in ecological resource research: Theories, methods, and challenges. Science China Earth Sciences, 63:1457–1474, 2020.
28. Jun Seong Lee, Minseok Seo, Sang Woo Kim, and Minho Choi. Fetal qrs detection based on convolutional neural networks in noninvasive fetal electrocardiogram. In 2018 4th International Conference on Frontiers of Signal Processing (ICFSP), pages 75–78. IEEE, 2018.
29. Shi Cao, Hui Xiao, Gao Gong, Weiyang Fang, and Chaomin Chen. Morphology extraction of fetal ecg using temporal cnn-based nonlinear adaptive noise cancelling. Plos one, 17(12):e0278917, 2022.
30. Radana Kahankova, Radek Martinek, Rene Jaros, Khosrow Behbehani, Adam Matonia, Michal Jezewski, and Joachim A Behar. A review of signal processing techniques for non-invasive fetal electrocardiography. IEEE reviews in biomedical engineering, 13:51–73, 2019.
31. Sasan Karamizadeh, Shahidan M Abdullah, Azizah A Manaf, Mazdak Zamani, and Alireza Hooman. An overview of principal component analysis. Journal of Signal and Information Processing, 4(3B):173, 2013.
32. Sergio Sanchez-Martinez, Nicolas Duchateau, Tamas Erdei, Alan G Fraser, Bart H Bijnens, and Gemma Piella. Characterization of myocardial motion patterns by unsupervised multiple kernel learning. Medical image analysis, 35:70–82, 2017.
33. Yen-Yu Lin, Tyng-Luh Liu, and Chiou-Shann Fuh. Multiple kernel learning for dimensionality reduction. IEEE Transactions on Pattern Analysis and Machine Intelligence, 33(6):1147–1160, 2010.
34. Mehmet Gönen and Ethem Alpaydın. Multiple kernel learning algorithms. The Journal of Machine Learning Research, 12:2211–2268, 2011.
35. Jean-Philippe Collet, Holger Thiele, Emanuele Barbato, Olivier Barthélémy, Johann Bauersachs, Deepak L Bhatt, Paul Dendale, Maria Dorobantu, Thor Edvardsen, Thierry Folliguet, et al. 2020 esc guidelines for the management of acute coronary syndromes in patients presenting without persistent st-segment elevation: The task force for the management of acute coronary syndromes in patients presenting without persistent st-segment elevation of the european society of cardiology (esc). European heart journal, 42(14):1289–1367, 2021.
36. MBBS Edwin Chandraharan, DCRM DFFP, Lead Consultant Labour Ward, and NHS St George's Healthcare. Stan: An introduction to its use, limitations and caveats.

37. Alexandra DJ Hulsenboom, Kim MJ Verdurmen, Rik Vullings, M Beatrijs van der Hout-van der Jagt, Anneke Kwee, Judith OEH van Laar, and S Guid Oei. Relative versus absolute rises in t/qrs ratio by st analysis of fetal electrocardiograms in labour: a case-control pilot study. Plos one, 14(3):e0214357, 2019.
38. Gari Clifford, Reza Sameni, Jay Ward, Julian Robinson, and Adam J Wolfberg. Clinically accurate fetal ecg parameters acquired from maternal abdominal sensors. American journal of obstetrics and gynecology, 205(1):47–e1, 2011.
39. Gernot Plank*, Axel Loewe*, Aurel Neic*, Christoph Augustin, Yung-Lin (Cary) Huang, Matthias Gsell, Elias Karabelas, Mark Nothstein, Jorge Sánchez, Anton Prassl, Gunnar Seemann*, and Ed Vigmond*. The openCARP simulation environment for cardiac electrophysiology. Computer Methods and Programs in Biomedicine, 208:106223, 2021.
40. H Martinez-Navarro, B Rodriguez, A Bueno-Orovio, and A Minchole. Repository for modelling acute myocardial ischemia: simulation scripts and torso-heart mesh. 2019.
41. Lazar Bibin, Jérémie Anquez, Juan Pablo de la Plata Alcalde, Tamy Boubekeur, Elsa D. Angelini, and Isabelle Bloch. Whole-body pregnant woman modeling by digital geometry processing with detailed uterofetal unit based on medical images. IEEE Transactions on Biomedical Engineering, 57(10):2346–2358, 2010.
42. Hector Martinez-Navarro, Ana Mincholé, Alfonso Bueno-Orovio, and Blanca Rodriguez. High arrhythmic risk in antero-septal acute myocardial ischemia is explained by increased transmural reentry occurrence. Scientific reports, 9(1):16803, 2019.
43. Daniel D Streeter Jr, Henry M Spotnitz, Dali P Patel, John Ross Jr, and Edmund H Sonnenblick. Fiber orientation in the canine left ventricle during diastole and systole. Circulation research, 24(3):339–347, 1969.
44. Kirsten HWJ Ten Tusscher and Alexander V Panfilov. Alternans and spiral breakup in a human ventricular tissue model. American Journal of Physiology-Heart and Circulatory Physiology, 291(3):H1088–H1100, 2006.
45. Mathias Wilhelms, Olaf Dössel, and Gunnar Seemann. Comparing simulated electrocardiograms of different stages of acute cardiac ischemia. In Functional Imaging and Modeling of the Heart: 6th International Conference, FIMH 2011, New York City, NY, USA, May 25-27, 2011. Proceedings 6, pages 11–19. Springer, 2011.
46. Dirk Durrer, R Th Van Dam, GE Freud, MJ Janse, FL Meijler, and RC Arzbaecher. Total excitation of the isolated human heart. Circulation, 41(6):899–912, 1970.
47. Lauren J Green, Lucy H Mackillop, Dario Salvi, Rebecca Pullon, Lise Loerup, Lionel Tarassenko, Jude Mossop, Clare Edwards, Stephen Gerry, Jacqueline Birks, et al. Gestation-specific vital sign reference ranges in pregnancy. Obstetrics & Gynecology, 135(3):653–664, 2020.
48. Eric H Dellinger, Frank H Boehm, and Martin M Crane. Electronic fetal heart rate monitoring: early neonatal outcomes associated with normal rate, fetal stress, and fetal distress. American journal of obstetrics and gynecology, 182(1):214–220, 2000.
49. G Jimenez-Perez, F Loncaric, PM Marti Castellote, M Ramos Jovani, E Gonzales Lopez, J Gonzales Mirelis, G Piella, O Camara, A Garcia-Alvarez, P Garcia-Pavia, et al. Machine learning-based phenotyping and risk assessment of hypertrophic cardiomyopathy-linking ecgs, morphology and genotypes. European Heart Journal-Cardiovascular Imaging, 23(Supplement_1):jeab289–431, 2022.
50. Guillermo Jimenez-Perez, Alejandro Alcaine, and Oscar Camara. Delineation of the electrocardiogram with a mixed-quality-annotations dataset using convolutional neural networks. Scientific reports, 11(1):863, 2021.
51. Peter J. Rousseeuw. Silhouettes: A graphical aid to the interpretation and validation of cluster analysis. Journal of Computational and Applied Mathematics, 20:53–65, 1987.

Chapter 5
Reconstruction of a Pancreatic Beta Cell Network From Heterogeneous Functional Measurements

Roshni Shetty, Radhika Singh-Agarwal, Stefan Meier, Christian Goetz, Andrew G Edwards

Abstract Intercellular heterogeneity is fundamental to most biological tissues. For some cell types, heterogeneity is thought to be responsible for distinct cellular phenotypes and functional roles. In the pancreatic islet, subsets of phenotypically distinct beta cells (hub and leader cells) are thought to coordinate electrical activity of the beta cell network. This hypothesis has been addressed by experimental and computational approaches, but none have attempted to reconstruct functional specialization directly from measured heterogeneity. To evaluate if electrophysiologic heterogeneity alone can explain these specialized functional roles, we created a population of human beta cell models (via genetic algorithm optimization) recapitulating the heterogeneity in an extensive patch clamp dataset (1021 pancreatic cells). Then we applied the simplified Kirchhoff network (SKNM) formalism to simulate activity of that population in a connected beta cell network. We could not immediately observe cells with obvious hub or leader phenotypes within the heterogeneous network. However, with this study we built the basis for further ”ground-up” investigation of relationships between beta cell heterogeneity and human islet function. Moreover, our workflow may be translated to other tissues where large electrophysiologic data

Roshni Shetty
Department of Pharmacology, University of California Davis, USA

Radhika Singh-Agarwal
Department of Physiology and Pharmacology, State University of New York (SUNY) Downstate Health Sciences University, USA

Stefan Meier
Department of Cardiology, Maastricht University, NL; Cardiovascular Research Institute Maastricht (CARIM), Maastricht University, NL

Christian Goetz
Institute of Biomedical Engineering, Karlsruhe Institute of Technology (KIT), DE

Andrew G Edwards (corresponding author)
Department of Computational Physiology, Simula Research Laboratory, NO e-mail: andy@simula.no

K. J. McCabe (ed.), *Computational Physiology*, Simula SpringerBriefs on Computing 17,
https://doi.org/10.1007/978-3-031-53145-3_5

sets become available, and heterogeneity is thought to influence tissue function e.g. human atria.

5.1 Introduction

Intercellular heterogeneity is the cornerstone of functional complexity and enables coordinated responses and specialized functions of cells within a tissue [1]. Hence, it has become increasingly important to study intercellular heterogeneity to unravel the mechanisms underlying the basic function of many organs, as well as disease and development. However, the ability to make detailed assessment of cellular properties in a sufficient number of cells to properly characterize heterogeneity is often limited by experimental throughput. Historically this has certainly been true, and remains true, for electrophysiological characterization of many tissues (the brain being an important exception). It is only rarely that characteristics other than the Gaussian mean and some measure of distribution spread are reported for most electrophysiologic variables. Expression measurements at the RNA and protein levels are often provided in more detail, such as for markers measurable by flow cytometry. However, this is also rare for ion transporters, the building blocks of cellular electrical activity. To date, these challenges in experimental data collection have largely prevented modeling approaches that have tried to systematically link heterogeneity in cellular properties to macroscopic electrophysiologic function.

The pancreas is an organ with both endocrine and exocrine functions. The endocrine cells (alpha, beta, gamma, delta, and epsilon) are arranged in small clusters (several hundred to one thousand cells) called islets, which serve as mini-organs. Cells of an islet work together to maintain blood glucose homeostasis [2]. Beta cells that synthesize and secrete insulin, account for approximately 70% of human islet cells [3]. Experimental studies of isolated beta cells show that they exhibit high intercellular variability in terms of the insulin the secrete in response to both basal glucose concentration (2-3 mM), and upon increasing glucose to simulate prandial conditions. This functional heterogeneity is of great importance to normal islet behavior and regulation of insulin release [4]. A prominent hypothesis in the field of beta cell biology is that subsets of beta cells served different roles in determining both electrical activity and insulin release (e.g. leader, hub, and first response cells) [5, 6]. However, the metabolic and electrical profile of these different integrated phenotypes is yet to be definitively characterized. Here, we attempt to answer whether experimental data describing heterogeneity in a range of cellular electrophysiologic properties can explain the specialized functional roles of heterogeneous beta cells within an islet.

In this study, we combine *in vitro* data obtained from a recent and comprehensive patch clamp data set of isolated human beta cells [7] with a computationally designed framework for reconstructing that heterogeneity in a population of in silico beta cell models (PoM) approach [8, 9]. In this approach, key model parameters (e.g., channel conductances, transporters maximal transport velocity) are varied to reca-

pitulate measured reference data. To align the simulated population distribution with the experimental distribution, we employ genetic algorithms as an able optimization method to find appropriate parameter adjustments. These are ”good enough” solutions to the optimization problem, but are generally not unique. Subsequently, the diverse simulated population is coupled in a tissue-level architecture, with heuristics to specify intercellular coupling in a manner that is consistent with measurements, but random with respect to the cellular electrical phenotype. This *in silico* islet can then be perturbed to gain insights into the functional significance of heterogeneity at a tissue level.

5.2 Methods

5.2.1 Data and Model

The experimental data utilized in this study was obtained from Camunas-Soler *et al.* [7] (https://github.com/jcamunas/patchseq) which comprises an extensive collection of patch clamp data encompassing 1021 pancreatic cells. Within this data set, information concerning six key electrophysiological outcome metrics were extracted from a series of 4 distinct voltage clamp protocols. The metrics were: (1) early (EE) and (2) total exocytosis (TE) (in fF/pF); (3) early and (4)late Ca^{2+} current (in pA/pF); (5) peak Na^{+} current (in pA/pF); and, (6) Na^{+} channel half-inactivation (V_{half},in mV). These data were measured in 180 healthy beta cells. Figure 5.3 shows the experimental distributions of the outcome metrics. To implement the voltage clamp protocols and derive the six outcome metrics for each member of the *in silico* population of models, we used MATLAB (release 2022B). These simulations were executed on the human pancreatic beta cell model developed by Riz *et al.* [10].

5.2.2 Workflow

Figure 5.1 shows the workflow that was followed to match the simulated model data distributions to the experimental electrophysiological data distributions [7] which is computationally expensive. Subsequently, the optimized parameters were used to create a 3D heterogeneous model of a human pancreatic islet network. First, we employed a sensitivity analysis to identify the most important parameters related to Na^{+} -and Ca^{2+} outcomes (i.e., EE and TE (in fF/pF), early and late Ca^{2+} current peaks (in pA/pF), peak Na^{+} current (in pA/pF), and Vhalf (in mV) to reduce the parameter space and increase computational efficiency. From the initial 86 parameters, only eight were selected for optimization. Subsequently, an iterative process of model generation and parameter optimization through a genetic algorithm was employed to map the model distributions to the experimental distributions. Once the fits matched sufficiently, several populations were generated. Finally, these populations were em-

bedded in a network of connected beta cells forming a heterogeneous 3D model of a pancreatic islet.

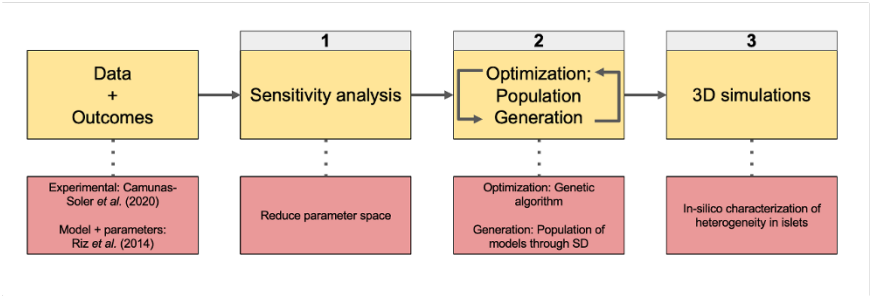

Fig. 5.1: Workflow for parameter selection, optimization, model generation and 3D simulations.

5.2.3 Sensitivity Analysis

A sensitivity analysis was performed to better understand the impact of individual parameters on the Na^+ -and Ca^{2+}-related outcome parameters, and thereby constrain the search space for the optimization algorithm. A simple linear scaling —by factors of 4, 2, 1, 0.5, and 0.25 — was applied to each model parameter individually, while the remaining parameters were held at their baseline value. First, the voltage-clamp protocols were pre-paced for at least 10 s after which the protocols were evaluated. The changes in outcome parameters for each scaling factor were compared to their baseline value.

5.2.4 Genetic Algorithm Optimization and Population Generation

From the sensitivity analysis, the parameters with most influence on the electrophysiological metrics were identified and collectively defined as $set\{\mathbf{P}\}$. An initial value of standard deviation for every parameter belonging to the $set\{\mathbf{P}\}$ was obtained from independent small-sample data sources [11], and used as the initial guess of variation for these parameters within the beta cell population. For each iteration of the GA, a new population of beta cells was generated by applying the standard deviation in $set\{\mathbf{P}\}$ to sample a from a log-normal distribution using the baseline value of the Riz *et al.* model as the centre. 750 models were generated in each population.

To address the bimodal distribution observed in the Na^+ current half-inactivation, we introduced a second Na^+ current component to the Riz *et al.* model. This sec-

ondary current had a lower average half-inactivation voltage, resulting in a population where each cell expressed either the default high Na^+ current (as in the original Riz *et. al* model) or the newly introduced low Na^+ current. The parameter $Frac_{high}$ governed the ratio of models expressing the high and low Na^+ current components (each model cell was assumed to only exhibit one dominant form of the current). An initial value of 0.15 was set, resulting in 113 models representing the high Na^+ current and 637 models expressing the low inactivation Na^+ current. Next, the six outcome metrics were assessed for each model in the population. The primary objective of the optimization was to closely align the simulated population distributions of these metrics with the corresponding experimental distributions.

Given the non-normal nature of the distributions, parameters were calculated to capture skewness (**S**), kurtosis (**K**), and the mean-to-standard deviation ratio ($\boldsymbol{\mu/\sigma}$) for both experimental and simulated distributions of skewed Gaussian metrics (such as early and total exocytosis, early and late Ca^{2+} current peaks, and peak Na^+ current). These calculations were facilitated using built-in MATLAB functions, and the GA's cost function aimed at reducing the error in (**S**), (**K**), and ($\boldsymbol{\mu/\sigma}$) between the two distributions (Equation 5.1 and 5.2),

$$Cost function = \arg\min E_1(k) \tag{5.1}$$

$$E_1(k) = \sum_k |S_e - S_s| + |K_e - K_s| + |\mu_e/\sigma_e - \mu_s/\sigma_s| \tag{5.2}$$

where k is the type of metric distribution and subscript e and s denote the value derived from the experimental and simulated distribution respectively.

For the bimodal distribution of the Na^+ current half-inactivation, a double gaussian curve was fitted using the MATLAB curve-fitting toolbox. Parameters $\mu_1, \mu_2, \sigma_1, \sigma_2$, and the ratio of the two gaussian peaks a_1/a_2 were selected for optimization. Similarly, the differences between these parameters were minimized in the cost function for both experimental and simulated distributions (Equation 5.3 and 5.4).

$$Cost function = \arg\min E_2(k) \tag{5.3}$$

$$E_2(k) = \sum_k |\mu_{1_e} - \mu_{1_s}| + |\mu_{2_e} - \mu_{2_s}| + |\sigma_{1_e} - \sigma_{1_s}| + |\sigma_{2_e} - \sigma_{2_s}| + |a_{1_e}/a_{2_e} - a_{1_s}/a_{2_s}| \tag{5.4}$$

GA optimization was performed with the Global Optimization Toolbox in MATLAB [12, 13]. Figure 5.1 outlines the main steps in this process. The standard deviations of parameters in $set\{\mathbf{P}\}$ and the $Frac_{high}$ were iteratively adjusted in each generation to minimize the error between the simulated and experimental distributions. The optimized standard deviations for $set\{\mathbf{P}\}$ and $Frac_{high}$ values were selected to construct the final population, which was again constructed by log-normal sampling of parameters in $set\{\mathbf{P}\}$ as well as $Frac_{high}$. For other non-optimized parameters (not-identified by the sensitivity analysis), independent measures of in-

tercellular variability (standard deviation) were taken from the source data used to construct the baseline Riz model, or similar human beta cell datasets ([11]). As earlier, the mean of this log-normal variation was always centered at the baseline value of the Riz *et al.* model parameter. Table 5.1 presents a list of all parameters varied, along with the corresponding means and standard deviations (normalized to the baseline Riz *et al.* model value).

5.2.5 3D Beta Cell Network Simulations

Multiple cell-based models have been developed in recent years [14, 15, 16, 17, 18, 19], to capture tissue electrodiffussion in varying degrees of detail. A recently published model aiming at balancing the need for cell-level accuracy and computational efficiency is the KNM [20]. This model incorporates individual cells with explicit representation of the local extracellular space. The fundamentals of this model are related to Kirchhoff's current law which states that the sum of all currents flowing into one node (cell) is equal to the sum of all currents flowing out of that node (cell). While incorporating individual cells, the computational efficiency of the KNM is still comparable to to models in which extracellular and intracellular space are not geometrically distinct e.g. the bidomain (BD) model [20]. The KNM can be reduced to the simplified KNM (SKNM) by assuming equal anisotropy of intra- and extracellular conductances, which further improves efficiency with little penalty on realism [21]. In this study, we apply the SKNM to study the effect of cellular heterogeneity on the integrated function of a connected network of islet beta cells. We assumed the extracellular potential to be negligible (equal to 0) which leads to the following equations [21] (or $G_e^{j,k} >> G_i j,k$):

$$C_m \frac{dv^k}{dt} = \frac{1}{A_m^k} \sum_{j \in N_k} G_i^{j,k}(v^j - v^k) - I_{ion}^k(v^k, s^k), \tag{5.5}$$

$$\frac{ds^k}{dt} = F_k(s^k, v^k) \tag{5.6}$$

C_m describes the specific membrane capacitance (in $\mu F/cm^2$), A_m^k is the membrane area of cell k (in cm^2), N_k is the number of connected cells to cell k, $G_i^{j,k}$ is the intracellular conductance between cells j and k (in mS), v^k is the membrane potential of cell k (in mV) (analogue for v^j) and I_{ion}^k is the ion current density through ion channels, pumps and exchangers on the membrane of cell k (in $\mu A/cm^2$). Lastly, F_k is a function describing the dynamics of a number of state variables s^k that model the membrane dynamics of cell k [21].

For the computational domain we used a human islet with 257 individual beta cells reconstructed from confocal microscopy data containing information about the positions, radii and contacts between all beta cells, based on ([22, 23]). To define which cells are electrotonically coupled via gap junctions, and to set the conduc-

tance for those connected beta cells, we computed the overlap (or separating distance) between adjacent cells in the confocal dataset. We assumed the gap junction conductance to be proportional to that distance, with an average gap junction conductance of $G_{mean} = 2 \times 10^{-7}$ mS [24]. The individual gap junction conductance $G_i^{j,k}$ between cell j and k is then calculated based on the distance $l^{j,k}$ between cells j and k normalized to the mean distance l_{mean} between all cells:

$$G_i^{j,k} = \frac{l^{j,k}}{l_{mean}} \cdot G_{mean} \tag{5.7}$$

As a baseline, we performed simulations of a homogeneous network i.e., each beta cell in the geometry represents an instance of the default Riz *et al.* model with original parameters. To study the impact of electro-metabolic heterogeneity we replace each of those default model instances with instances taken from the final population of the Riz *et al.* models. Thus, each cell in the heterogeneous beta cell network has an instance of the Riz *et al.* model with some variation (from default) in the underlying parameters (table 5.1), although the distribution across all cells remains fitted to the experimental distributions. Finally, the equation system is solved for each time step in two individual steps. First, the ordinary differential equations (ODE) of the cell model are solved by using the forward Euler method. The time step for solving the ODEs is typically ten times higher than for the partial differential equations (PDE) to ensure achieving a steady-state in the membrane model. Second, the PDEs are solved and the membrane potentials are updated. Parameters for the temporal discretization and numerical solver are shown in the supplementary material

5.3 Results

5.3.0.1 Sensitivity Analysis

As anticipated, the parameters related to Ca^{2+} channel and Na^{+} conductance and gating primarily affected the outcome metrics of interest (i.e., EE, TE, Vhalf, peak I_{Na}, peak I_{Ca}, and late I_{Ca}), while the parameters related to K^{+} channels did not. The following parameters were selected based on the 2- and 0.5-fold scaling results for the optimization process by the GA: g_{Na}, g_{CaPQ}, g_{CaL}, g_{NaLow}, V_{mNa}, V_{hNa}, V_{mNaLow}, and V_{hNaLow} (Figure 5.2).

5.3.1 Genetic Algorithm Optimization and Population Generation

Two sets of GA optimizations were executed as outlined in Subsection 5.2.4. The initial set concentrated on optimizing the standard deviations of g_{CaPQ} and g_{CaL}, while minimizing ER_1, pertaining to four distributions namely, EE and TE, and early and late Ca^{2+} current peaks. The second optimization was for the standard deviations

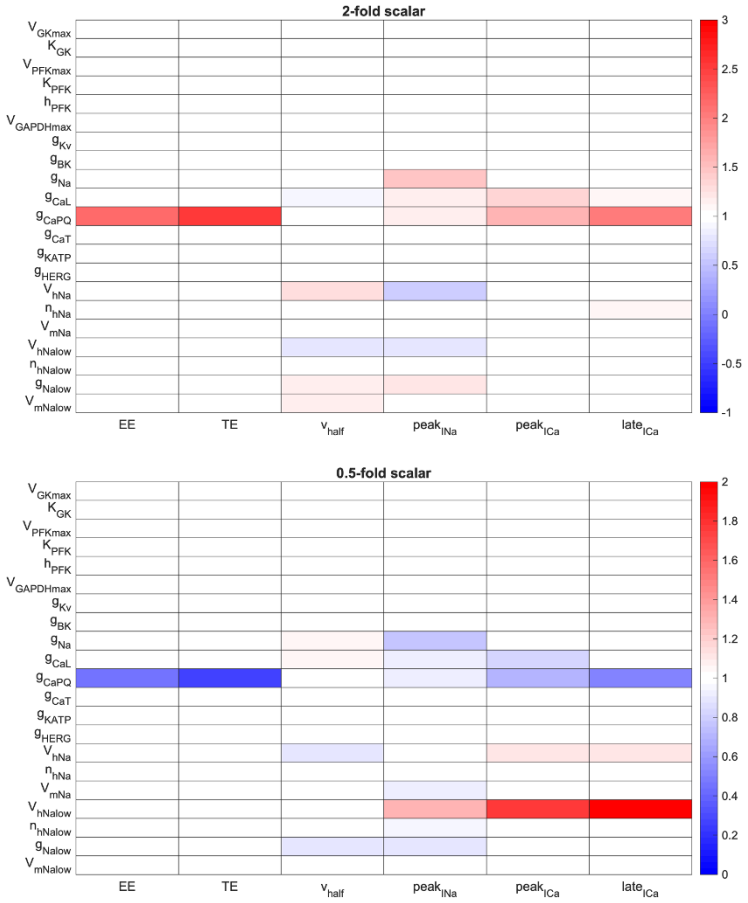

Fig. 5.2: Sensitivity analysis. The top panel shows the results of 2-fold parameter scaling and the bottom panel shows the results of 0.5-fold parameter scaling.

of g_{Na}, g_{Nalow}, V_{mNA}, V_{hNa}, V_{mNaLow}, V_{hNaLow} and the parameter $Frac_{high}$. In this case, ER_1 was minimized for the peak Na^+ current, while ER_2 was minimized for the Na^+ current half-inactivation (mV).

A detailed compilation of all parameters that were varied in the populations is presented in Table 5.1, encompassing the 9 parameters that were optimized using GA, as well as the additional 13 parameters whose standard deviations were obtained from independent data sources. The ultimate population was generated through log-normal variation, using the optimized standard deviations of parameters and $Frac_{high}$ (determined by the GA), as outlined in Subsection 5.2.4. Figure 5.3 provides comparison between the experimental and simulated metric distributions for all outcome metrics.

Table 5.1: Parameters varied in the model to create the final population, and their corresponding mean (μ) and standard deviation (σ); (Parameters optimized by the GA are in bold font)

Parameter	μ	σ	Reference
$V_{GK_{max}}$	1.31	1.15	[25]
K_{GK}	1.48	1.44	[26]
$V_{PFK_{max}}$	1.00	0.03	[27]
K_{PFK}	1.00	0.09	[27]
h_{PFK}	1.02	0.14	[27]
$V_{GAPDH_{max}}$	1.02	0.29	[28]
g_{Kv}	1.08	0.40	[29]
g_{BK}	1.26	1.14	[29]
$\mathbf{g_{CaL}}$	**1.01**	**0.15**	**GA**
$\mathbf{g_{CaPQ}}$	**1.20**	**0.68**	**GA**
g_{CaT}	1.07	0.44	[29]
g_{KATP}	1.47	1.53	[30]
g_{HERG}	1.05	0.34	[31]
$\mathbf{V_{hNa}}$	**1.01**	**0.18**	**GA**
n_{hNa}	1.00	0.12	[29]
$\mathbf{g_{Na}}$	**1.54**	**1.72**	**GA**
$\mathbf{V_{mNa}}$	**1.00**	**0.25**	**GA**
$\mathbf{V_{hNa_{low}}}$	**1.02**	**0.24**	**GA**
$n_{hNa_{low}}$	0.98	0.16	[7]
$\mathbf{g_{Na_{low}}}$	**1.33**	**1.01**	**GA**
$\mathbf{V_{mNa_{low}}}$	**0.97**	**0.35**	**GA**
$\mathbf{Frac_{high}}$	**0.21**	-	**GA**

5.3.2 3D Beta Cell Network Simulations

To assess the impact of heterogeneity on the behavior of an intact beta cell network, we compared a network of homogeneous beta cells with a heterogeneous network in which cells were sampled from the population optimized to fit the experimental distributions. For both simulations, the islet structure we used consisting of 257 beta cells with identical connectivity. Figure 5.4 shows membrane potential frames from these simulations. In the left column, we see that all beta cells of the homogeneous network depolarize simultaneously from a resting membrane potential (RMP) of -68 mV to a peak membrane potential of -11 mV. This is to be expected, given that all cells in the geometry have identical cellular properties. In contrast, in the heterogeneous network no coordinated depolarization can be observed. While some beta cells depolarize to a peak membrane potential of 16 mV, most beta cells remain at a membrane potentials between -73 mV and -30 mV.

To explore the role of specific subpopulations in the heterogeneous network, we analyzed the time courses of the membrane potentials of individual beta cells. Figure 5.5a illustrates the membrane potential of a typical beta cell in the homo-

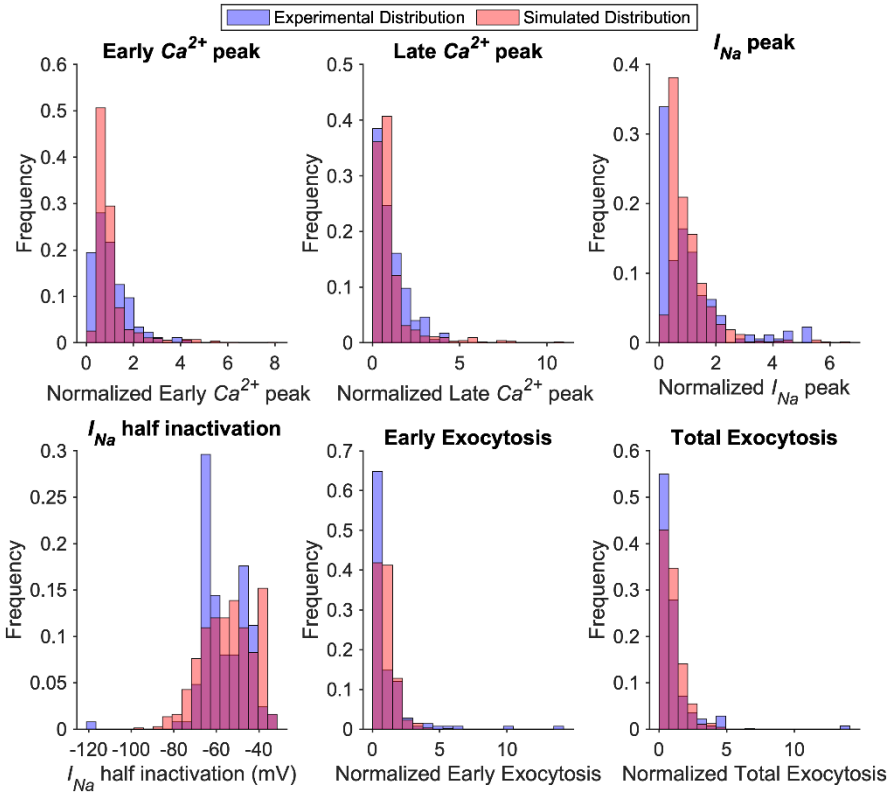

Fig. 5.3: Probability density histograms for the outcome metrics of the experimental and simulated population distributions [Blue: experimental distribution (n = 180); Red: optimized simulated distribution (n = 750); Purple: overlap]

geneous network within two periods of bursting behavior (40 s - 74 s and 185 s - 219 s) and a peak membrane potential of −11 mV. In the heterogeneous network we identified all beta cells with bursting behavior and evaluated if neighboring cells exhibited coordinated activity. Figure 5.5b shows a subset of six neighboring cells in the heterogeneous network in which interdependencies could be observed. The most significant bursting behavior can be observed for beta cell 141 with peak membrane potentials of −27 mV. However, the RMP of all beta cells of the heterogeneous network is significantly higher than in the homogeneous network with membrane potentials of −50 ± 5 mV. To evaluate if beta cell 141 exhibits hub-like behavior, we present the behavior of cells that are in its subnetwork. Figure 5.5c shows the connections of beta cell 141 with neighboring beta cells. It can be observed that the amplitudes of the beta cells diminish with increasing distance from cell 141 - see membrane potentials of beta cells 141, 156, 157 and 154 Figure 5.5b. However, beta cells 158 and 153 show significantly smaller amplitudes than beta cell 157

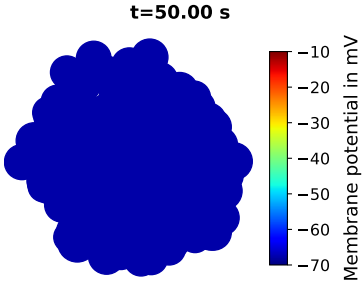

(a) Membrane potentials in homogeneous islet after 50.00 s

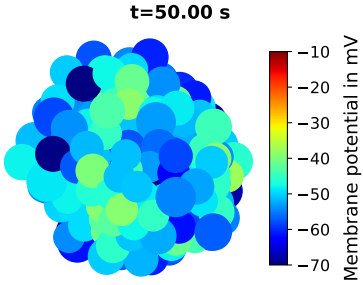

(b) Membrane potentials in heterogeneous islet after 50.00 s

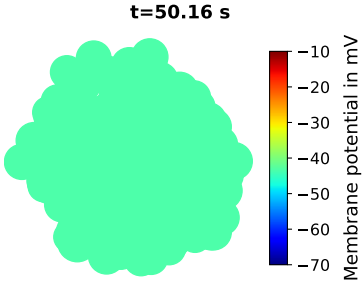

(c) Membrane potentials in homogeneous islet after 50.16 s

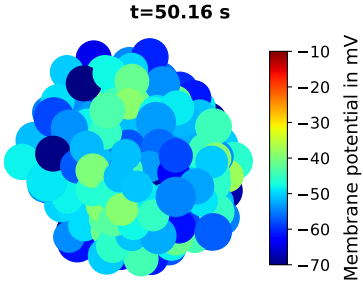

(d) Membrane potentials in heterogeneous islet after 50.16 s

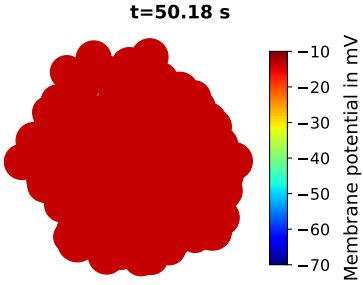

(e) Membrane potentials in homogeneous islet after 50.18 s

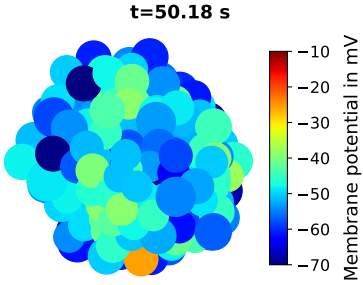

(f) Membrane potentials in heterogeneous islet after 50.18 s

Fig. 5.4: Membrane potentials at different time steps of a human islet with homogeneous (left column) and heterogeneous cellular properties (right column).

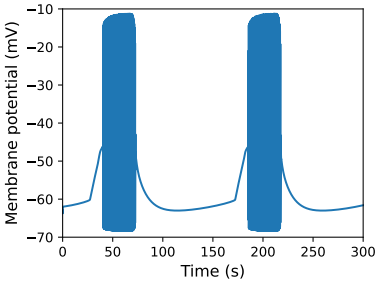

(a) Time course of the membrane potential of a beta cell from the homogeneous islet network

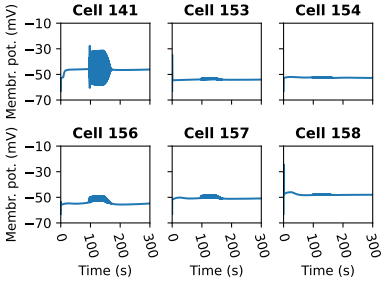

(b) Time course of the membrane potential of six neighboring beta cells from the heterogeneous islet network

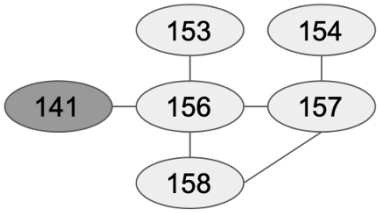

(c) Subset of the cell-cell contacts of the islet network showing the neighboring cells of cell 141.

Fig. 5.5: Time courses of the membrane potential of individual beta cells in the homogeneous (a) and heterogeneous islet network (b) and schematic subset of the cell-cell contacts of the islet network (c).

although they are all connected to beta cell 156. To summarize, only one subset of six neighboring beta cells of the heterogeneous network could be observed that show coordinated depolarizations. Moreover, the amplitudes of depolarizations decrease with increasing distance to the beta cell with the highest amplitudes. Together these analyses demonstrate that the higher activity of cell 141 is not sufficient to overcome the electrotonic load of its coupled adjacent beta cells.

5.4 Discussion

In this study, we have provided a workflow to create a heterogeneous model population that reflects experimental data to subsequently study the effects of this heterogeneity on a coupled pancreatic beta cell network. The sensitivity analysis was the first step to reduce the parameter space and to speed up the model fitting and

optimization procedure, while getting an idea about how the model responds to changes in parameters. In this study, we used a linear scaling technique similar to Meier *et al.* [32] to scale individual parameters which is rudimentary in comparison to Monte Carlo and Bayesian methods [33]. The parameter selection was based on the 2-fold and 0.5-fold scaling, because these scalars resulted in a robust change without producing unphysiological behavior. Figure 5.2 also shows that the parameters behave in a non-linear fashion. For example, a 0.5-fold decrease in V_{hNaLow} caused a more than 2-fold increase in peak I_{Ca} and late I_{Ca}, while increasing the parameter by 2-fold did not meaningfully change peak I_{Ca} and late I_{Ca}. Nonetheless, the identified parameters obtained by our linear sensitivity analysis provided a good starting point for the GA and substantially increased computational efficiency by reducing the parameter space to only 9 parameters.

A major initial assumption was that through implementing a log-normal variation within the parameter space would yield skewed distributions for early and late exocytosis, early and late Ca^{2+} current peaks, and the peak Na^{+} current, along with a double Gaussian distribution for the Na^{+} current half-inactivation. Our findings validate this assumption by demonstrating that the optimized final simulated population closely aligns with the experimental distributions (depicted in Figure 5.3). This outcome corroborates the insights from several previous studies [34, 35]. With the coherence observed in the simulated distributions, it is credible to claim that the simulated population mirrors the inherent heterogeneity observed in experimental electrophysiological metrics.

Through our SKNM network simulations, we showed that randomly applying experimentally constrained electrophysiologic heterogeneity tends to stabilize the overall behavior of a coupled network of human beta cells. Moreover, we could not observe locally specialized functional roles within the network based on intercellular heterogeneity. Although there were clear examples of locally important electrotonic synchronisation, the electrotonic load was too great to permit broader influence and regenerative local or global activation. The properties of neighbouring cells were important in determining this local electrotonic load. This can be seen in Figure 5.5b and Figure 5.5c, where the electrotonic distance (number of cells from source cell 141) was less important than the coupled cell's properties in determining their response.Thus, it is likely that either non-random distribution of cellular properties, or perhaps reduction or regionalisation of intercellular coupling may be required to observe typical hub or leader cell roles. These relationships require further assessment, and can now be studied in the future by extracting subpopulations from the experimental data set and by applying these parameter sets in specific regions of the islet.

5.5 Conclusion

This study showed a general approach to introduce physiologically realistic heterogeneity in a beta-cell network model by combining a population-of-models approach,

with a cell-based tissue electroconduction model - the SKNM. Since randomly applying heterogeneity (obtained from the fitted population) to the network model did not immediately yield prototypical glucose responses or experimentally observed functional specialization within the network, further investigation is required to determine the potential for regional similarities in cellular phenotype or intercellular coupling to permit those behaviors.

This work defines an initial framework for generating heterogeneous models of the human islet that are driven by recent high-volume experimental datasets. Models of this type are likely to be useful in understanding the role of intercellular heterogeneity in driving specific aspects of network behavior.

References

1. Steffen Walherr. Estimation methods for heterogeneous cell population models in systems biology. Journal of Royal Society, October 2018.
2. Kara Rogers. islets of Langerhans, volume 2. Encyclopedia Britannica, 2022.
3. Joseph W. Kim, John Z.Q. Luo, and Luguang Luo. Chapter 10 - bone marrow mesenchymal stem cells as a new therapeutic approach for diabetes mellitus. In Xiao-Dong Chen, editor, A Roadmap to Non-Hematopoietic Stem Cell-based Therapeutics, pages 251–273. Academic Press, 2019.
4. Richard KP Benninger and Vira Kravets. The physiological role of β-cell heterogeneity in pancreatic islet function. Nature Reviews Endocrinology, 18(1):9–22, 2022.
5. Gabriela Da Silva Xavier and Guy A. Rutter. Metabolic and functional heterogeneity in pancreatic ß cells. Journal of Molecular Biology, 432(5):1395–1406, 2020. Islet Biology in Type 2 diabetes.
6. Natalie R. Johnston, Ryan K. Mitchell, Elizabeth Haythorne, Maria Paiva Pessoa, Francesca Semplici, Jorge Ferrer, Lorenzo Piemonti, Piero Marchetti, Marco Bugliani, Domenico Bosco, Ekaterine Berishvili, Philip Duncanson, Michael Watkinson, Johannes Broichhagen, Dirk Trauner, Guy A. Rutter, and David J. Hodson. Beta cell hubs dictate pancreatic islet responses to glucose. Cell Metabolism, 24(3):389–401, 2016.
7. Joan Camunas-Soler, Xiao-Qing Dai, Yan Hang, Austin Bautista, James Lyon, Kunimasa Suzuki, Seung K. Kim, Stephen R. Quake, and Patrick E. MacDonald. Patch-seq links single-cell transcriptomes to human islet dysfunction in diabetes. Cell Metabolism, 31(5):1017–1031.e4, May 2020.
8. Eric A. Sobie. Parameter Sensitivity Analysis in Electrophysiological Models Using Multivariable Regression. Biophysical Journal, 96(4):1264–1274, February 2009.
9. Stefano Morotti and Eleonora Grandi. Logistic regression analysis of populations of electrophysiological models to assess proarrythmic risk. MethodsX, 4:25–34, January 2017.
10. Michela Riz, Matthias Braun, and Morten Gram Pedersen. Mathematical modeling of heterogeneous electrophysiological responses in human β-cells. PLoS Computational Biology, 10(1):e1003389, January 2014.
11. Matthias Braun, Reshma Ramracheya, Martin Bengtsson, Quan Zhang, Jovita Karanauskaite, Chris Partridge, Paul R Johnson, and Patrik Rorsman. Voltage-gated ion channels in human pancreatic beta-cells: electrophysiological characterization and role in insulin secretion. Diabetes, 57(6):1618–28, 2008.
12. The MathWorks Inc. Global optimization toolbox version 4.8.1 (r2023a), 2023.
13. The MathWorks Inc. Parallel computing toolbox version 7.8 (r2023a), 2023.
14. Karoline Jæger and Aslak Tveito. Derivation of a Cell-Based Mathematical Model of Excitable Cells, pages 1–13. Springer International Publishing, 10 2020.

15. Aslak Tveito, Karoline Jæger, Miroslav Kuchta, Kent-Andre Mardal, and Marie Rognes. A cell-based framework for numerical modeling of electrical conduction in cardiac tissue. Frontiers in Physics, 5, 10 2017.
16. Karoline Jæger, Andrew Edwards, Wayne Giles, and Aslak Tveito. From millimeters to micrometers; re-introducing myocytes in models of cardiac electrophysiology. Frontiers in Physiology, 12, 10 2021.
17. Ada Ellingsrud, Andreas Solbrå, Gaute Einevoll, Geir Halnes, and Marie Rognes. Finite element simulation of ionic electrodiffusion in cellular geometries. Frontiers in Neuroinformatics, 14:11, 03 2020.
18. Ada Ellingsrud, Cécile Daversin-Catty, and Marie Rognes. A Cell-Based Model for Ionic Electrodiffusion in Excitable Tissue, pages 14–27. Springer International Publishing, 10 2020.
19. Åshild Telle, James Trotter, Xing Cai, Henrik Finsberg, Miroslav Kuchta, Joakim Sundnes, and Samuel Wall. A cell-based framework for modeling cardiac mechanics. Biomechanics and Modeling in Mechanobiology, 22, 01 2023.
20. Karoline Jæger and Aslak Tveito. Efficient, cell-based simulations of cardiac electrophysiology; the kirchhoff network model (knm). NPJ systems biology and applications, 9:25, 06 2023.
21. Karoline Jæger and Aslak Tveito. The simplified kirchhoff network model (sknm); a cell-based reaction-diffusion model of excitable tissue. Unpublished, 2023.
22. Gerardo J. Félix-Martínez, Aurelio N. Mata, and J. Rafael Godínez-Fernández. Reconstructing human pancreatic islet architectures using computational optimization. Islets, 12(6):1–13, 2020.
23. Gerardo J. Félix-Martínez and J. R. Godínez-Fernández. Comparative analysis of reconstructed architectures from mice and human islets. Islets, 14(1):23–35, 2021.
24. Habo J. Jongsma and Ronald Wilders. Gap junctions in cardiovascular disease. Circulation Research, 86(12):1193–1197, 2000.
25. J Takeda, M Gidh-Jain, L Z Xu, P Froguel, G Velho, M Vaxillaire, D Cohen, F Shimada, H Makino, and S Nishi. Structure/function studies of human beta-cell glucokinase. enzymatic properties of a sequence polymorphism, mutations associated with diabetes, and other site-directed mutants. J. Biol. Chem., 268(20):15200–15204, July 1993.
26. M Gidh-Jain, J Takeda, L Z Xu, A J Lange, N Vionnet, M Stoffel, P Froguel, G Velho, F Sun, and D Cohen. Glucokinase mutations associated with non-insulin-dependent (type 2) diabetes mellitus have decreased enzymatic activity: implications for structure/function relationships. Proceedings of the National Academy of Sciences, 90(5):1932–1936, March 1993.
27. Peter M. Fernandes, James Kinkead, Iain McNae, Paul A.M. Michels, and Malcolm D. Walkinshaw. Biochemical and transcript level differences between the three human phosphofructokinases show optimisation of each isoform for specific metabolic niches. Biochemical Journal, 477(22):4425–4441, November 2020.
28. Michael J. Mac Donald. Does glyceraldehyde enter pancreatic islet metabolism via both the triokinase and the glyceraldehyde phosphate dehydrogenase reactions? Archives of Biochemistry and Biophysics, 270(1):15–22, April 1989.
29. Matthias Braun, Reshma Ramracheya, Martin Bengtsson, Quan Zhang, Jovita Karanauskaite, Chris Partridge, Paul R. Johnson, and Patrik Rorsman. Voltage-gated ion channels in human pancreatic β-cells: Electrophysiological characterization and role in insulin secretion. Diabetes, 57(6):1618–1628, June 2008.
30. R Bränström, Craig A Aspinwall, S Välimäki, C-G Östensson, A Tibell, M Eckhard, H Brandhorst, BE Corkey, P-O Berggren, and O Larsson. Long-chain coa esters activate human pancreatic beta-cell k atp channels: potential role in type 2 diabetes. Diabetologia, 47:277–283, 2004.
31. Barbara Rosati, Piero Marchetti, Olivia Crociani, Marzia Lecchi, Roberto Lupi, Annarosa Arcangeli, Massimo Olivotto, and Enzo Wanke. Glucose-and arginine-induced insulin secretion by human pancreatic β-cells: the role of HERG K+ channels in firing and release. The FASEB Journal, 14(15):2601–2610, 2000.
32. Stefan Meier, Adaïa Grundland, Dobromir Dobrev, Paul G. A. Volders, and Jordi Heijman. In silico analysis of the dynamic regulation of cardiac electrophysiology by kv11.1 ion-channel trafficking. The Journal of Physiology, 601(13):2711–2731, February 2023.

33. Brodie A. J. Lawson, Christopher C. Drovandi, Nicole Cusimano, Pamela Burrage, Blanca Rodriguez, and Kevin Burrage. Unlocking data sets by calibrating populations of models to data density: A study in atrial electrophysiology. Science Advances, 4(1), January 2018.
34. Trine Krogh-Madsen, Eric A. Sobie, and David J. Christini. Improving cardiomyocyte model fidelity and utility via dynamic electrophysiology protocols and optimization algorithms. The Journal of Physiology, 594(9):2525–2536, 2016.
35. Trine Krogh-Madsen, Anna F. Jacobson, Francis A. Ortega, and David J. Christini. Global Optimization of Ventricular Myocyte Model to Multi-Variable Objective Improves Predictions of Drug-Induced Torsades de Pointes. Frontiers in Physiology, 8, 2017.

Chapter 6
The Impact of Mechano-Electric Feedback on Drug- and Stretch- Induced Arrhythmia Using a Computational Model of Cardiac Electromechanics

Anthony Asencio, Melania Buonocunto, Matthew W Ellis, Karl Munthe, Kyle T Stark, Joakim Sundnes, Henrik Finsberg, and Hermenegild J Arevalo

Abstract Mechano-electric feedback (MEF) is thought to be an important factor in the increased arrhythmic risk observed clinically in heart failure and chronic infarct patients. Here, we utilize pathologic stretch as a parameter for investigating the sensitivity of cardiac electrophysiology and mechanics to MEF. To simulate the effects of stretch, we incorporated stretch-activated ion channels (SACs) into a coupled electro-mechanics model based on the well-established O'Hara-Rudy (ORd) (electrophysiology) Land (mechanics) models. We investigated the effect different degrees of stretch had upon electrophysiological parameters such as the action potential duration and calcium transient, as well as functional parameters like force production. We further determined the sensitivity of cardiac cells under stretch to various pro- and anti-arrhythmic drugs to better inform on drug risk

Anthony Asencio
Department of Bioengineering, University of Washington, USA

Melania Buonocunto
Department of Biomedical Engineering, Maastricht University, NL; Cardiovascular Research Institute Maastricht (CARIM), Maastricht University, NL

Matthew W Ellis
Department of Medicine, University of California San Diego, USA

Karl Munthe
Department of Computational Physiology, Simula Research Laboratory, NO; Department of Informatics, University of Oslo, NO

Kyle T Stark
Department of Mechanical and Aerospace Engineering, University of California San Diego, USA

Joakim Sundnes (corresponding author)
Department of Computational Physiology, Simula Research Laboratory, NO email: sundnes@simula.no

Henrik Finsberg
Department of Computational Physiology, Simula Research Laboratory, NO

Hermenegild J Arevalo
Department of Computational Physiology, Simula Research Laboratory, NO

K. J. McCabe (ed.), *Computational Physiology*, Simula SpringerBriefs on Computing 17,
https://doi.org/10.1007/978-3-031-53145-3_6

classifications and indications. Our results indicate that pathologic stretch may exert a severe pro-arrhythmic effect on cardiac cells, which markedly exacerbates the risk profile of pro-arrhythmic drugs, but one which was mitigated through the action of anti-arrhythmic compounds.

6.1 Introduction

Patients with heart failure have increased risk of arrhythmia, which may be exacerbated by some medications used in treatment. The Comprehensive in vitro Pro-Arrhythmia Assay (CiPA) involves computational and experimental modeling alongside clinical observations to form a risk stratification profile for clinically prescribed medications for heart failure patients. In the present study we sought to further inform these risk profiles by incorporating mechano-electric feedback (MEF) into the in silico modeling of drug effects, using a coupled model based on the O'Hara-Rudy model (ORd) for human ventricular electrophysiology [1] and the model by Land et al. for myocyte mechanics [2]. The coupling of the two models occurs primarily through intracellular calcium, which regulates tension development by binding to Troponin C, see, for instance, [2] for details. This binding is tension dependent, and thereby creates an MEF effect where the mechanical state of the myocyte affects the concentration of free calcium and thereby the electrical activity of the cell.

MEF is thought to be a significant contributor to spontaneous arrhythmia development in heart failure patients [3], but has yet to be deeply investigated in computational studies coupling cardiac electrophysiology and mechanics. In addition to the tension-dependent calcium buffering, known mechanisms of MEF include stretch-activated ion channels (SACs) [4]. These are channels in the cell membrane that open in response to mechanical stimuli (i.e., cell stretch), and thereby allow ions to flow in and out of the cell. Three SACs are typically recognized in cardiac tissue; non-selective cation channels (SACns) primarily conducting sodium and potassium (and, to a lesser degree, calcium), potassium-selective channels (SACK), and calcium-selective channels (SACCa). We incorporated established and physiologically representative mathematical formulations for these three SACs into the coupled electro-mechanics model.

Furthermore, we chose various CiPA compounds across the risk profile, including Dofetilide and Bepridil (high risk), Domperidone and Cisapride (intermediate risk), and Ranolazine and Diltiazem (low risk). These drugs were chosen due to their role in blocking either rectifying potassium currents, which contributes to elongated action potentials (AP) and possible early after depolarization events, calcium currents, a critical linkage mechanism in MEF, or both. We sought to assess the effect of pathological stretch via SAC activation on electrophysiology and mechanics at baseline, and in combination with drug activity to investigate any altered sensitivity to drug action.

6.2 Models and Methods

In this section we first describe the single cell electro-mechanics model, including MEF and the modifications to incorporate drugs, as well as the experimental protocol. The coupled electro-mechanics model was based on the published version of the ORd and Land et al models [1, 2], and we here focus on the coupling of the models in terms of calcium binding, force development, and SACs. For a complete specification of the models we refer to the original publications.

6.2.1 Stretch-Activated Channels

We incorporated three SACs currents in the coupled ORd-Land model: I_{SACns}, I_{SACKo} and I_{SACCaP}. The implementation of the first two currents was based on the formulation by Niederer and Smith (2007) [5], while their calibration and the stretch dependence of the I_{SACns} expression were based on Buonocunto et al. (2023) [6]. Finally, we formulated the last current deriving it from the expression of the background calcium current of the ORd model. The mechanical input to the SACs is the extension ratio λ, which is the ratio of the current sarcomere length (SL) to the slack length. The SACs are formulated so that they are closed and non-conducting for $\lambda \leq 1$ (contraction), and open for $\lambda > 1$ (stretch).

The stretch-activated I_{SACns} current was defined as the sum of a sodium and a potassium component:

$$I_{SACns} = I_{SACns_{Na}} + I_{SACns_K}, \tag{6.1}$$

with:

$$I_{SACns_{Na}} = r \cdot g_{ns} \cdot \gamma_{SL,ns} \cdot (V_m - E_{Na}), \tag{6.2}$$

$$I_{SACns_K} = g_{ns} \cdot \gamma_{SL,K} \cdot (V_m - E_K). \tag{6.3}$$

Here, g_{ns} is the maximal conductance of the SAC_{ns}, E_{Na} and E_K are the reversal potentials of sodium and potassium, and $\gamma_{SL,ns}$ the sigmoidal stretch dependence of the conductance, defined as

$$\gamma_{\mathrm{SL,ns}} = 0.5 \frac{\beta_{\mathrm{ns}} (\lambda - 1)^3}{0.15^3 + (\lambda - 1)^3} .$$

Furthermore, the stretch-activated I_{Ko} current was formulated as

$$I_{SACKo} = g_{Ko} \cdot \frac{\gamma_{SL,Ko} \cdot (V - E_K)}{1 + e^{\frac{10+V}{45}}}, \tag{6.4}$$

with g_{Ko} being the maximal conductance of the SAC_{Ko}, and $\gamma_{SL,Ko}$ the stretch dependence of the conductance defined by $\gamma_{\mathrm{SL,Ko}} = \beta_{\mathrm{Ko}} \ (\lambda - 1) + 0.7$. Finally, we formulated the the calcium mechanosensitive current as

$$I_{SACCaP} = 4 \cdot G_{CaP} \cdot x \cdot (-0.341 \cdot [Ca^{2+}]_o + [Ca^{2+}]_i \cdot e^{\frac{2VF}{RT}}) \cdot \frac{VF^2}{RT(e^{\cdot \frac{2VF}{RT}} - 1.0)}, \quad (6.5)$$

with G_{CaP} being the channel conductance, F, R, and T conventional thermodynamic constants, $[Ca^{2+}]_i$ and $[Ca^{2+}]_o$ the intracellular and extracellular calcium concentrations. In addition, both I_{SACns} and I_{SACKo} were divided by the membrane capacitance C_m which was expressed as a Hill-curve that increases with increasing stretch:

$$C_{\mathrm{m}} = 1.534 \times 10^{-4} \left(\frac{(\lambda - 1)^4}{0.035^4 + (\lambda - 1)^4} + 1 \right), \quad (6.6)$$

as experimentally observed by [7] and parameterised by [6].

6.2.2 Mechanical Modeling

The mechanical aspect of our model was addressed by the incorporation of the Land model of cardiac contraction [2]. Here, the total force is expressed as a sum of different passive and active contributions [8]. The active force results from the crossbridge cycle, in which ATP-driven myosin translates along filamentous actin. The resulting force is expressed as the product of the mean cross-bridge distortion and cross-bridge stiffness, assuming that these behave as elastic springs. Passive forces include an elastic component coming mainly from titin and collagen, and a viscous component. Force balance requires that the net force on a myocyte is zero:

$$F_a + F_p + F_{se} + F_v + F_{pre} = 0, \quad (6.7)$$

where F_a is the active force, F_p is the passive elastic force, $F_{se} = K_{se}(\lambda - \lambda_{set})$ is a series elastic force, for which the spring stiffness K_{se} and set stretch λ_{set} can be varied to mimic different experimental settings. Furthermore, F_v is the viscous force and F_{pre} is a constant preload applied to the myocyte.

The formulation of the active force is taken from [2], and given by

$$F_a = h(\lambda) \frac{T_{ref}}{r_s} ((1 + \zeta_s)S + \zeta_w W). \quad (6.8)$$

Here, T_{ref} is the tetanic (maximum) force at the resting length, $\lambda = 1$ [8, 2], r_s is the steady state duty ratio, while $h(\lambda)$ is a phenomenological function that accounts for the force-length relationship. Finally, the expression $((1+\zeta_s)S+\zeta_w W)$ describes how the dynamic force varies with the crossbridge cycling, with ζ_s and ζ_w being the distortion of the crossbridges in the strongly (S) and weakly (W) bound states, respectively.

The sensitivity of active force to stretch is increased by the cooperativity of tropomyosin along actin. The binding of calcium to a single troponin site increases the probability of calcium binding to the neighboring sites, thereby increasing the

myosin binding probability and, as a result, the active force. For a more detailed description and complete formulation of the equations, we refer to Land, et al. [2].

6.2.3 Modeling the Effect of Drugs

To model the activity of various drugs on ion channel conductance, we used the following equation:

$$SF = \frac{g_{drug}}{g} = \left[1 + \left(\frac{EFTPC}{IC_{50}}\right)^{h}\right]^{-1}. \tag{6.9}$$

Here g is a measure of ion channel conductance, EFTPC is the effective free therapeutic plasma concentration of each drug, IC_{50} is the inhibitory concentration of the drug necessary to bring each respective channel activity down to 50%, and h is the Hill coefficient characterizing cooperativity of the drug and channel interaction. EFTPC, IC_{50}, and h for each drug and channel used in this study were based on previously published experimental and clinical results [9, 10, 11]. SF indicates the scaling factor for each respective channel, which could be used as a parameter in the coupled model to simulate drug action.

As an example, Table 6.1 summarizes the scaling factors for the various ion channels for the compound Ranolazine.

Table 6.1: Ion channel scaling factors (SF) for various plasma concentrations of Ranolazine

Channel SF	1x EFTPC	2x EFTPC	4x EFTPC
I_{Kr}	0.810	0.681	0.516
I_{Na}	0.663	0.512	0.360
I_{NaL}	0.800	0.668	0.503
I_{CaL}	0.975	0.954	0.918
I_{Ks}	0.994	0.989	0.978
I_{K1}	1.000	1.000	1.000
I_{to}	1.000	1.000	1.000

6.2.4 Experimental Protocol

After pre-pacing our simulations for 50 beats to reach steady state for all the electrophysiological signals, we ran isometric test simulations using the governing equations presented above and $K_{se} = 10^6$. The stretch was kept constant (at

$\lambda = 0.9, 0.95, 1, 1.05, 1.1, 1.2$) for the duration of the cycle length (1000 ms) while the electromechanics signals were evaluated. Furthermore, to observe the effect of quick stretch release on the electromechanics signals, we performed a stretch/release test. It consisted of holding stretch constant at a set value ($\lambda = 1.00, 1.05, 1.1$) for 600 ms, and then suddenly releasing 2% of the applied stretch and keeping it constant for the remaining cycle length (400 ms).

6.3 Results

6.3.1 Isometric Behavior

Application of isometric stretch and contraction in presence of SACs did not provoke any changes when $\lambda \leq 1$, while it caused prolongation of the AP with $\lambda > 1$ (figure 6.1A). Additionally, $\lambda = 1.20$ caused a complete loss of AP morphology and prevented repolarization. Similarly, the intracellular Ca^{2+} peak value increased with all λ values, although it provoked larger increase with $\lambda > 1$ (figure 6.1B). However, $\lambda = 1.2$ completely flattened the signal. Similar behaviour was observed for the Ca^{2+} bound to Troponin (data not shown). Furthermore, the active force signal was found to increase positively with both expansion (stretch > 1) and compression (stretch ≤ 1) in figure 6.2A in absence of SACs. The addition of current from SACs (figure 6.2B) prolonged the duration of the active force signal and accentuated the dome shape for values of stretch > 1. Stretch values less than or equal to one were not effected by the presence of SACs. However stretch > 1 increased active force relative to the no-SACs case.

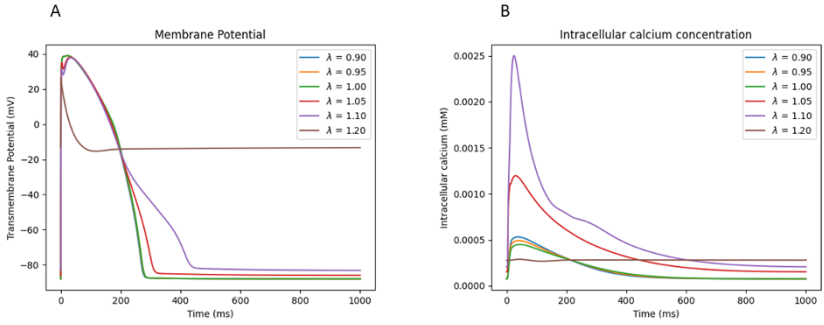

Fig. 6.1: Membrane Potential A) and Intracellular [Ca^{2+}] B) over a range of isometric stretches in presence of SACs.

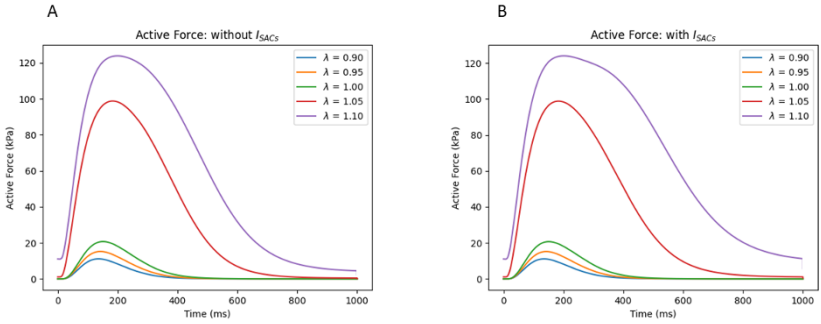

Fig. 6.2: Active forces over a range of isometric stretches A) without SACs and B) with SACs.

6.3.2 Stretch/Release Test

We performed the stretch/release test and evaluated the changes to the electromechanics signals at the moment of release and in presence of SACs. The membrane voltage underwent a small (< 5%) sudden decrease in amplitude (figure 6.3A), while the active force showed a more pronounced drop (maximum 25%) and a subsequent recovery of the signal with decreased amplitude (figure 6.3B) with $\lambda > 1$.

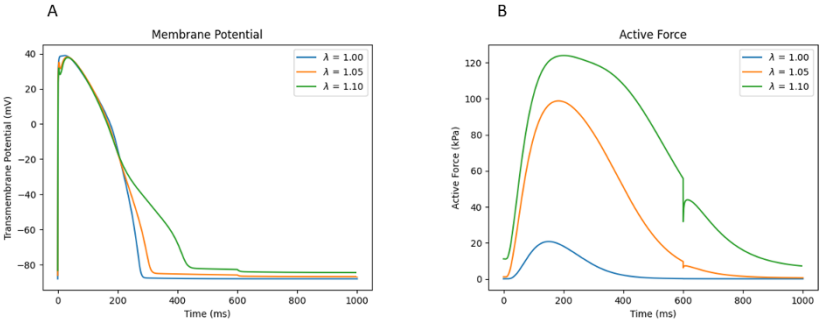

Fig. 6.3: Effects of stretch/release test on A) Membrane potential and B) Active force in presence of SACs.

6.3.3 Drug Effects in Isometric Conditions

Using (6.9) with reference values for drug concentration and activity [9, 10, 11], we assessed the effect of each drug on the AP and force output. The results are summarized in Table 6.2, and a representative plot is shown in figure 6.4.

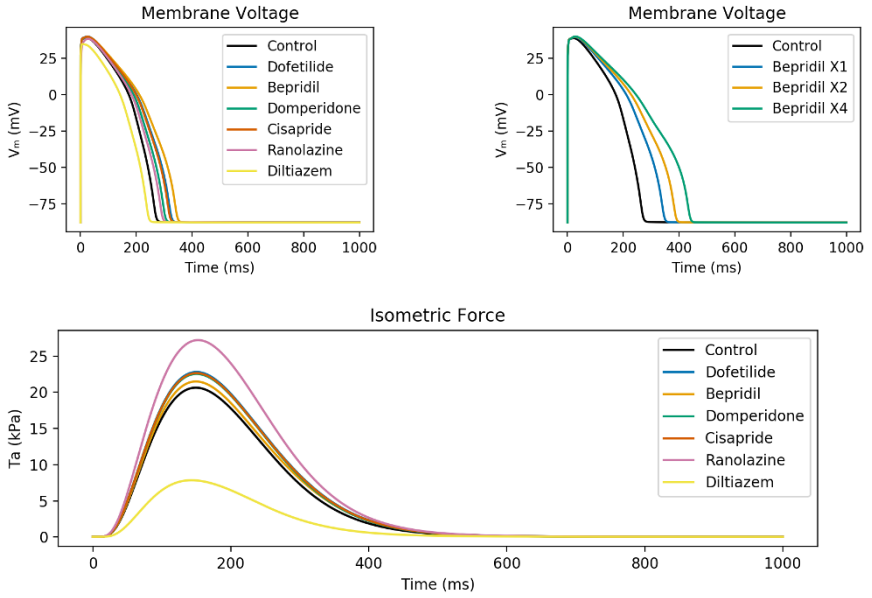

Fig. 6.4: Effect of various CiPA drug compounds on the cardiac action potential.

Table 6.2: Effect of CiPA drugs on the action potential duration at 90% repolarization APD_{90} and maximum force

Drug	APD_{90} (ms)	Maximum Force (kPa)
Control	263.7	20.6
Dofetilide	317.9	22.8
Bepridil	339.2	21.5
Domperidone	296.2	22.5
Cisapride	312.8	22.6
Ranolazine	286.1	28.0
Diltiazem	236.9	10.3

Of the drugs assessed, Bepridil displayed the most pronounced effects on the AP relative to the control state, causing the largest increase of APD_{90} at the EFTPC. To further classify the pro-arrhythmic effect of Bepridil, we ran additional simulations at twice and four times the EFTPC of the drug, and observed worsening on the above outcomes, including longer APD_{90} and lower maximum force values with higher doses, as well as the appearance of early after depolarizations indicative of arrhythmia risk.

6.3.4 Combining Drugs with Stretch

In order to evaluate the effect of MEF more comprehensively, we next combined our modeling of pathologic stretch together with drug implementations. Based on known drug activity and our results at the EFTPC of each simulated drug, we focused our efforts on Bepridil (a high-risk CiPA pro-arrhythmic compound which elongated APD_{90} versus control) and Diltiazem (a low-risk CiPA anti-arrhythmic compound which shortened the APD_{90} and greatly reduced maximum force versus control) to characterize the extent to which stretch sensitizes cardiomyocytes to drug action. As shown in Figure 6.5, we found that the introduction of 5% pathologic stretch served to elongate the APD_{90} at 1x EFTPC Bepridil by over 200 ms versus the unstretched condition, a duration twice that of the control condition, while exacerbating the appearance of early after depolarization events. On the other hand, the presence of Diltiazem greatly mitigated the deleterious effects of pathologic stretch, with the 1x EFTPC and 5% pathologic stretch maintaining an action potential of similar duration and appearance to the control condition.

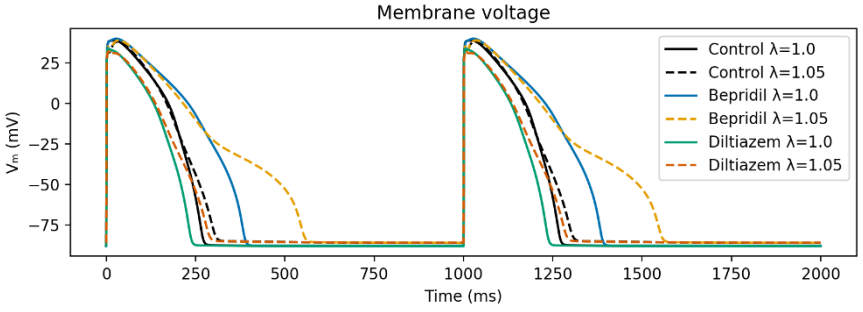

Fig. 6.5: Effect of 2X plasma concentration of the pro-arrhythmic Bepridil and anti-arrhythmic Diltiazem on the cardiac action potential when combined with pathologic stretch.

6.4 Conclusion

We have developed a coupled model of mechano-electric feedback in human cardiomyocytes, by incorporating mechano-electric feedback in the form of SACs in the ORd-Landcoupled electromechanics model. The SACs were formulated so that they would have no effect on sarcomeric force production or AP morphology when stretch was less than or equal to one, which is consistent with previous studies. However, under conditions of pathological stretch, the SACs were shown to amplify the force-stretch relation and the increased Ca^{2+} binding with stretch, which is expected since the SACs give rise to an increase in Ca^{2+} influx. Following this finding, we incorporated non-physiologic stretch into our drug implementation scheme. Focusing on the most pro-arrhythmic compound assessed, Bepridil, and the most anti-arrhythmic drug assessed, Diltiazem, we were able to characterize the interaction between drug activity and pathologic stretch. Notably, we found that even 5% non-physiologic stretch was able to markedly exacerbate the pro-arrhythmic status of Bepridil, elongating the APD_{90} significantly, producing AP signatures more similar to many times the effective free therapeutic plasma concentration of the drug. This was in contrast to the anti-arrhythmic calcium channel blocker Diltiazem, which served to mitigate the pathological activity of non-physiological stretching, maintaining an AP signature highly similar to the unstretched control condition. The ORd-Land model with SACs was also straight forwardly implemented in a 3D finite element method (FEM) solver based on FEniCS[1] and used to compute the contraction and relaxation of a small rectangular slab of heart muscle tissue. Preliminary results indicate that the tissue reacts qualitatively similar to the cell model, but further investigation is needed to quantify how the 3D FEM model changes when SACs are included and compare the simulation results to experimental results. As mechano-electric feedback remains an understudied consideration in arrhythmia risk stratification models, we believe our findings here provide a more comprehensive model for cardiac disease modeling and better inform drug risk classifications and indications, thereby improving clinical care for patients with heart disease.

References

1. Thomas O'Hara, László Virág, András Varró, and Yoram Rudy. Simulation of the undiseased human cardiac ventricular action potential: model formulation and experimental validation. PLoS computational biology, 7(5):e1002061, 2011.
2. Sander Land, So-Jin Park-Holohan, Nicolas P Smith, Cristobal G Dos Remedios, Jonathan C Kentish, and Steven A Niederer. A model of cardiac contraction based on novel measurements of tension development in human cardiomyocytes. J. Mol. Cell. Cardiol., 106:68–83, May 2017.
3. T Alexander Quinn and Peter Kohl. Cardiac mechano-electric coupling: acute effects of mechanical stimulation on heart rate and rhythm. Physiological reviews, 101(1):37–92, 2021.

[1] https://fenicsproject.org/

4. Rémi Peyronnet, Jeanne M Nerbonne, and Peter Kohl. Cardiac mechano-gated ion channels and arrhythmias. Circulation research, 118(2):311–329, 2016.
5. Steven A Niederer and Nicolas P Smith. A mathematical model of the slow force response to stretch in rat ventricular myocytes. Biophysical journal, 92(11):4030–4044, 2007.
6. Melania Buonocunto, Aurore Lyon, Tammo Delhaas, Jordi Heijman, and Joost Lumens. Electrophysiological effects of stretch-activated ion channels: a systematic computational characterization. The Journal of Physiology, 2023.
7. Bernardo L de Oliveira, Emily R Pfeiffer, Joakim Sundnes, Samuel T Wall, and Andrew D McCulloch. Increased cell membrane capacitance is the dominant mechanism of stretch-dependent conduction slowing in the rabbit heart: a computational study. Cellular and molecular bioengineering, 8:237–246, 2015.
8. A. Raaum. Computational study of the impact of parameter variability and drugs on healthy and failing cardiac cells: A population of models approach to characterize drug effects on cell electrophysiology and mechanics. University of Oslo, Spring 2023.
9. William J. Crumb, Jose Vicente, Lars Johannesen, and David G. Strauss. An evaluation of 30 clinical drugs against the comprehensive in vitro proarrhythmia assay (cipa) proposed ion channel panel. Journal of Pharmacological and Toxicological Methods, 81:251–262, 2016. Focused Issue on Safety Pharmacology.
10. Zhihua Li, Sara Dutta, Jiansong Sheng, Phu N. Tran, Wendy Wu, Kelly Chang, Thembi Mdluli, David G. Strauss, and Thomas Colatsky. Improving the in silico assessment of proarrhythmia risk by combining herg (human ether-à-go-go-related gene) channel–drug binding kinetics and multichannel pharmacology. Circulation: Arrhythmia and Electrophysiology, 10(2):e004628, 2017.
11. Jordi Llopis-Lorente, Beatriz Trenor, and Javier Saiz. Considering population variability of electrophysiological models improves the in silico assessment of drug-induced torsadogenic risk. Computer Methods and Programs in Biomedicine, 221:106934, 2022.

Chapter 7
Impact of Modeling Assumptions on Hemodynamic Stresses in Predicting Cerebral Aneurysm Rupture Status

Guillermo L Nozaleda, Sofia Poloni, Luca Soliveri, Kristian Valen-Sendstad

Abstract Approximately 3% of the population is estimated to have cerebral aneurysms, which are the leading cause of subarachnoid haemorrhage. Convincing evidences suggest that wall shear stresses (WSS) play a role in vessel remodeling and in the development of vascular diseases. Since WSS cannot be directly measured, researchers have resorted to using medical images available in routine clinical practice to simulate computational fluid dynamics (CFD) and investigate patient-specific vascular conditions. They retrospectively analyse the correlation between WSS and disease outcomes to find potential clinical tools for future use. However, most of these models are based on assumptions that introduce variability and error. In this work we investigated the effects of a non-Newtonian viscosity model and inflow uncertainty on the prediction of commonly computed hemodynamic metrics. Our results show a substantial influence of the non-Newtonian model and blood flow rate on CFD outcomes, highlighting the need of incorporating non-Newtonian rheology and patient-specific blood flow measurements in CFD simulations.

Guillermo L Nozaleda
Department of Mechanical and Aerospace Engineering, University of California San Diego, USA

Sofia Poloni
Department of Engineering and Applied Sciences, University of Bergamo, IT

Luca Soliveri
Department of Biomedical Engineering, Istituto di Ricerche Farmacologiche Mario Negri (IRCCS), IT

Kristian Valen-Sendstad (corresponding author)
Department of Computational Physiology, Simula Research Laboratory, NO e-mail: kvs@simula.no

K. J. McCabe (ed.), *Computational Physiology*, Simula SpringerBriefs on Computing 17,
https://doi.org/10.1007/978-3-031-53145-3_7

7.1 Introduction

Roughly 3% of human population is estimated to be affected by cerebral aneurysms, which stand as the primary trigger for subarachnoid hemorrhages [1]. Aneurysm formation involves a complex interplay between biological processes within the blood vessel wall and hemodynamic factors [2]. The underlying hypothesis suggests that abnormal WSS triggers an inflammatory reaction, impacting arterial wall remodeling and significantly contributing to aneurysm initiation and progression [3]. If the arterial wall fails to withstand these forces, the aneurysm may rupture, resulting in high risk of mortality [4].

In the management of an aneurysm, evaluating risk of rupture is thus of utmost importance for clinicians [5]. Hemodynamic factors, especially WSS measurements, serve as common rupture indicators. However, direct WSS measurement from clinical observations is not feasible [6]. As an alternative, researchers employ real geometries from routine clinical practice to perform computational fluid dynamics (CFD) simulations and study patient-specific vascular conditions [7, 8, 9, 10, 11, 12]. Nevertheless, the reliability of CFD in the context of aneurysm management remains a subject of ongoing debate. In this context, a recent review by Steinman [6] explores each stage of the patient-specific CFD pipeline, emphasizing the influence of sources of variability and error. These sources include imaging techniques, blood rheology and artery wall characterization, prescribed boundary conditions, segmentation methods, and variations in solver numerics. While some of this variability can be mitigated through appropriate modeling, some assumptions are more critical to overcome, primarily due to the lack of patient-specific data.

Blood behaves as a non-Newtonian fluid and artery walls undergo cyclic deformations. Nevertheless, Steinman [6] argues that the potential benefits of including these characteristics in CFD simulations might be outweighed by the computational effort required. Consequently, many studies prefer simplified assumptions of constant viscosity and rigid walls, reducing computational cost and modeling complexity. Despite some efforts to investigate the effects of these simplifications [13, 14, 15], the debate surrounding proper modeling techniques remains open. When it comes to boundary conditions, it is important to establish reasonable outflow rates by employing proper scaling laws [16]. As for inflow rates, the generalized absence of patient-specific data makes it necessary to rely on estimations. This becomes a primary limitation, particularly since WSS magnitude and distribution are highly responsive to variations in these prescribed values [13, 17]. Additionally, careful consideration should be given to the locations of model truncation and diameter measurements to ensure accurate results [6]. Regarding solver numerics, Valen-Sendstad [18] demonstrated how commonly used schemes, meshes, and time steps in aneurysm CFD may dampen flow instabilities and alter stress distribution compared to higher-order approaches adopting fine spatial and temporal discretisations. Khan *et al.* [19], on the other hand, warned against relying on default schemes from commercial software. Furthermore, many studies assumed laminar flow and employed dissipative schemes for stability, which can potentially affect accuracy. Therefore, achieving a reliable numerical solution entails advanced schemes, avoiding laminar assumptions, ensur-

ing minimal dissipation, and fine discretisations. Our work considers these aspects for improved precision and robustness.

In the literature, most studies tend to focus on assessing the impact of a single factor on WSS. This often involves comparing works carried out with different CFD settings and methodologies, which may lead to ambiguous and misleading conclusions due to their reliance on particular numerical aspects. To address this limitation, our present study takes a more comprehensive approach by conducting an analysis that considers various modeling assumptions. The primary objective is to evaluate how these different conditions can influence the CFD outcomes, thereby providing further insights into the sources of variability and error. Specifically, the current work compares the impact of the controversial non-Newtonian model with that of inflow rates, which is universally considered to be one of the most influential between the modeling assumptions.

7.2 Methods

7.2.1 Study Population and Design

Five aneurysms geometries were selected form the open source AneuriskWeb repository [20]. These cases all involve internal carotid artery (ICA) aneurysms to ensure analysis consistency. For each geometry, we conducted four simulations: i) standard simulation (V0) with an standard inflow and constant viscosity, ii) non-Newtonian viscosity model, iii) 25% reduction in blood flow, and iv) 25% increase in blood flow. The conducted simulations, based on the standard deviations reported by Hoi *et al.* [21], were solved using the high performance Saga HPC cluster, a compute node with 20 Intel Xeon-Gold 6138 2.0 GHz cores. The typical computation time per simulation averaged 12 hours.

7.2.2 Computational Fluid Dynamics

Consider an incompressible fluid of kinematic viscosity ν and density ρ, in the absence of body forces the problem reduces to the integration of

$$\frac{\partial \boldsymbol{u}}{\partial t} + (\boldsymbol{u} \cdot \nabla)\, \boldsymbol{u} = \nu \nabla^2 \boldsymbol{u} - \nabla p, \tag{7.1}$$

$$\nabla \cdot \boldsymbol{u} = 0, \tag{7.2}$$

where $\boldsymbol{u} = (u_1, u_2, u_3)$ and p are the velocity and reduced pressure of the fluid.

The Navier-Stokes equations (7.1)-(7.2) were numerically solved using *Oasis*, an open-source and validated CFD solver [22]. *Oasis* is based on the Finite Element Method implemented on the FEniCS computing platform [23]. It utilizes a

segregated, space/time centered, incremental pressure correction scheme to achieve accurate solutions while minimizing numerical dispersion and diffusion [24]. Below, we provide a description of the spatial and temporal discretisations used in *Oasis*. For more detailed information about the solver and its numerical implementation, readers are referred to the original manuscript by Mortensen *et al.* [22].

7.2.2.1 Fractional Step Algorithm

In Oasis, a space/time catered fractional step method is used to advance in time. Let $[0, T]$ represent a cardiac cycle, which is divided into uniform intervals of length $\Delta t = t^n - t^{n-1}$, with $n \in \mathbb{Z}$. Specifically, we set $T = 0.951$ s and $\Delta t = 0.0951$ ms, resulting in 10,000 timesteps per cycle. Simulations spanned 3 cardiac cycles. Denoting u_k^n as the k velocity component at time t^n, the algorithm looks as follows

$$\textbf{Step 1:} \left\{ \frac{u_k^I - u_k^{n-1}}{\Delta t} + B_k^{n-1/2} = \nu \nabla^2 \tilde{u}_k - \nabla_k p^* \qquad \text{for} \quad k = \{1, 2, 3\}, \right. \tag{7.3}$$

$$\textbf{Step 2:} \left\{ \nabla^2 \varphi = -\frac{1}{\Delta t} \nabla \cdot \boldsymbol{u}^I, \right. \tag{7.4}$$

$$\textbf{Step 3:} \left\{ \frac{u_k^n - u_k^I}{\Delta t} = -\nabla_k \varphi \qquad \text{for} \quad k = \{1, 2, 3\}, \right. \tag{7.5}$$

where $\varphi = p^{n-1/2} - p^*$ denotes a pressure correction and p^* is a tentative pressure. In the first step (7.3), the viscous terms are handled using a Crank-Nicolson scheme, such that $\tilde{u}_k = 0.5\left(u_k^I + u_k^{n-1}\right)$, and the convective terms are incorporated in $B_k^{n-1/2}$. For the latter computation, Oasis provides two options,

$$B_k^{n-1/2} = \frac{3}{2}\boldsymbol{u}^{n-1} \cdot \nabla u_k^{n-1} - \frac{1}{2}\boldsymbol{u}^{n-2} \cdot \nabla u_k^{n-2} \quad \text{and} \quad B_k^{n-1/2} = \bar{\boldsymbol{u}} \cdot \nabla \tilde{u}_k. \tag{7.6}$$

The first approach in (7.6) consists of a fully explicit Adams-Bashforth discretization. In contrast, the second scheme is implicit, with $\bar{\boldsymbol{u}} = 1.5\boldsymbol{u}^{n-1} - 0.5\boldsymbol{u}^{n-2}$ and $\tilde{u}_k = 0.5\left(u_k^I + u_k^{n-1}\right)$, as given above.

Our objective is to calculate the updated values of $\boldsymbol{u}^n$ and $p^{n-1/2}$ for each time step. To accomplish this, we start by solving (7.3) to determine the tentative velocity $\boldsymbol{u}^I$, which is non-solenoidal (i.e., $\nabla \cdot \boldsymbol{u}^I \neq 0$). The velocity $\boldsymbol{u}^I$ is then used to determine $p^{n-1/2}$ upon resolution of Poisson's equation (7.4). Finally, we calculate from (7.5) the updated divergence-free velocity field $\boldsymbol{u}^n$.

7.2.2.2 Variational Formulation

For the spatial discretization, the finite element method is used to discretise (7.3)–(7.5) on the bounded domain $\Omega \subset \mathbb{R}^3$, with boundary $\partial\Omega$. All simulations employed second-degree Lagrange polynomials for velocity and first-degree for pres-

sure. This scheme guarantees second-order accuracy in the L2 norm, leading to an error reduction rate of at least $O(h^2)$ as the mesh size h is refined. Meshes with $210,000 - 240,000$ elements were obtained using VaMPy, which is equivalent to $1.68 - 1.92$ million linear elements [25]. We define the trial and test spaces

$$V = \left\{ v \in H^1(\Omega) : v = u_0 \text{ on } \partial\Omega \right\}, \quad \hat{V} = \left\{ v \in H^1(\Omega) : v = 0 \text{ on } \partial\Omega \right\}, \tag{7.7}$$

where $H^1(\Omega)$ is the Sobolev space, which contains functions v satisfying that v^2 and $|\nabla v|^2$ have finite integrals over Ω. Consider v and q to be the test functions for the velocity and pressure, respectively. The variational formulation of (7.3)–(7.5) can be obtained multiplying each equation by the corresponding test function and integrating along the domain, thereby yielding

$$\int_\Omega \frac{u_k^I - u_k^{n-1}}{\Delta t} v + B_k^{n-1/2} v + \nu \nabla \tilde{u}_k \cdot \nabla v \, \mathrm{d}x = \int_{\partial\Omega} \nu \nabla_n \tilde{u}_k v \mathrm{d}s - \int_\Omega \nabla_k p^* v \mathrm{d}x, \tag{7.8}$$

$$\int_\Omega \nabla\varphi \cdot \nabla q \, \mathrm{d}x - \int_{\partial\Omega} \nabla_n \varphi q \, \mathrm{d}s = \int_\Omega \frac{\nabla \cdot \boldsymbol{u}^I}{\Delta t} q \, \mathrm{d}x, \tag{7.9}$$

$$\int_\Omega \frac{u_k^n - u_k^I}{\Delta t} v \, \mathrm{d}x = -\int_\Omega \nabla_k \varphi v \, \mathrm{d}x, \tag{7.10}$$

after use is made of integration by parts. Above, ∇_n represents the gradient in the outward normal direction to the boundary $\partial\Omega$.

7.2.2.3 Boundary Conditions and Viscosity Models

In the absence of patient-specific measurements, an average blood flow of $4.05\,\mathrm{cm}^3/\mathrm{s}$ was applied at the inlet, referencing [21]. The inlet boundary conditions were established using the generalized blood flow curve from Oasis. Outlet pressure conditions were adjusted to achieve a blood flow split based on outlet cross-sectional areas.

Blood's viscosity changes in response to shear stress, a phenomenon known as non-Newtonian behavior. Despite this knowledge, many studies on intracranial aneurysms simplify blood as Newtonian fluid [10, 11, 12], assuming constant viscosity. This work aims to contrast the Newtonian approximation with a more accurate representation of the fluid rheology. In particular, the modified Cross model [26, 27]

$$\frac{\mu(\dot{\gamma}) - \mu_\infty}{\mu_0 - \mu_\infty} = \frac{1}{[1 + (\lambda\dot{\gamma})^m]^a} \tag{7.11}$$

is adopted here to characterize blood's non-Newtonian behavior. In the above expression $\dot{\gamma}$ is the shear rate, $\mu_\infty = 3.372\,\mathrm{mPa} \cdot \mathrm{s}$ and $\mu_0 = 3.372\,\mathrm{mPa} \cdot \mathrm{s}$ are the infinite-shear and zero-shear viscosities, respectively, whereas $\lambda = 3.736\,\mathrm{s}$, $m = 2.406$, and $a = 0.34$ represent fitting parameters. The kinematic viscosity, used in the above formulation, can be obtained from (7.11) as $\nu = \mu/\rho$.

7.2.3 Post-Processing

The post-processing of the results was performed exploiting VaMPy [25] functionalities and Paraview software. The post-processing was performed on the third cycle, to avoid artifacts due to initialization, and focusing on the aneurysm sac only. Commonly used rupture risk metrics, specifically time-averaged wall shear stresses (TAWSS) and oscillatory shear index (OSI), were calculated as follows

$$\text{TAWSS} = \frac{1}{T}\int_0^T \tau_W \mathrm{d}t \quad \text{and} \quad \text{OSI} = \frac{1}{2} - \left(1 - \frac{|\int_0^T \tau_W \mathrm{d}t|}{\int_0^T |\tau_W| \mathrm{d}t}\right). \tag{7.12}$$

Furthermore, VaMPy was adjusted to handle non-Newtonian effects during post-processing, including the storage of viscosity values from simulations for stress calculations.

7.3 Results

Figure 7.1 illustrates the qualitative velocity magnitude isosurfaces at the systolic peak for the four cases under analysis: the standard simulation (V0), the non-Newtonian model, and inflow rates altered by ±25%. In the standard simulation, distinct low-velocity recirculation zones and a complex flow phenotype are evident within the aneurysm sac. When incorporating non-Newtonian effects, the velocity gradient in the same region decreases due to higher viscosity values associated with low shear rates. In scenarios where the inflow rate is decreased or increased by 25%, there is a corresponding reduction or augmentation of velocity within the aneurysmal area.

Examining the distribution of TAWSS in Figure 7.2A, it is evident that TAWSS registers higher values at the neck of the aneurysm and exhibits lower values within the sac, where velocity recirculation is prominent. This pattern remains consistent for all models considered here. Furthermore, Figure 7.2B quantifies the effect of modeling assumption on the TAWSS within the aneurysm sac with respect to the V0 simulation. In the case of the non-Newtonian assumption, stresses decrease due to heightened viscosity. This effect mirrors the consequences of reduced inflow, where it is intuitive that lower flow results in decreased TAWSS. Likewise, an increase in inflow leads to a rise in TAWSS within the aneurysm sac, as expected. To conclude this part of the analysis, Table 7.1 outlines the influence of different modeling assumptions on TAWSS, expressed as a percentage alteration with respect to the V0 simulation. The numbers here reported solidify the observation that all cases exert a substantial impact on TAWSS. Notably, TAWSS displays heightened sensitivity to variations in flow beyond what would be expected from a linear relationship. The influence of the non-Newtonian assumption on stress levels is particularly significant, resulting comparable to a 25% decrease in inflow.

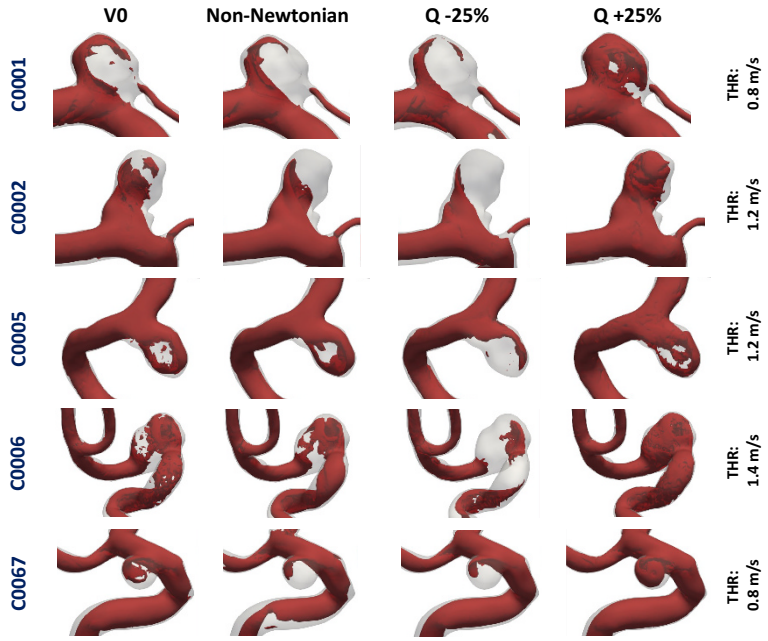

Fig. 7.1: Velocity magnitude isosurface. *Q: blood flow. THR: velocity threshold.*

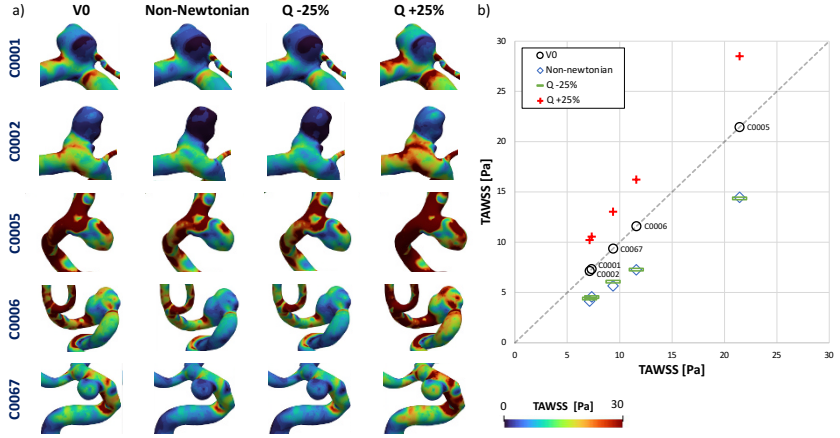

Fig. 7.2: a) Maps of TAWSS distribution. b) Effect of modeling assumptions on TAWSS with respect to the V0 simulation. *Q: blood flow. TAWSS: time average wall shear stress.*

Table 7.1: Impact of modeling assumptions: percentage variation of TAWSS with respect to V0 simulation. *Q: blood flow. TAWSS: time average wall shear stress.*

	TAWSS		
	Non-Newtonian	**Q - 25%**	**Q +25%**
C0001	-37,62	-38,13	44,01
C0002	-41,76	-38,69	43,17
C0005	-32,50	-33,10	32,98
C0006	-37,29	-37,40	40,01
C0067	-39,58	-35,20	39,15

Attention is given in Figure 7.3A to the OSI distribution for all geometries and models, highlighting regions within the aneurysmal sac with elevated OSI values, indicative of disturbed flow. From the quantitative results (Figure 7.3B and Table 7.2), it follows that OSI variations are more complex and do not correlate with the variations of inflow. Instead, the pronounced variability suggests that OSI is more sensitive to model geometries. Concerning the impact of non-Newtonian effects, the results underscore a substantial influence on OSI magnitude.

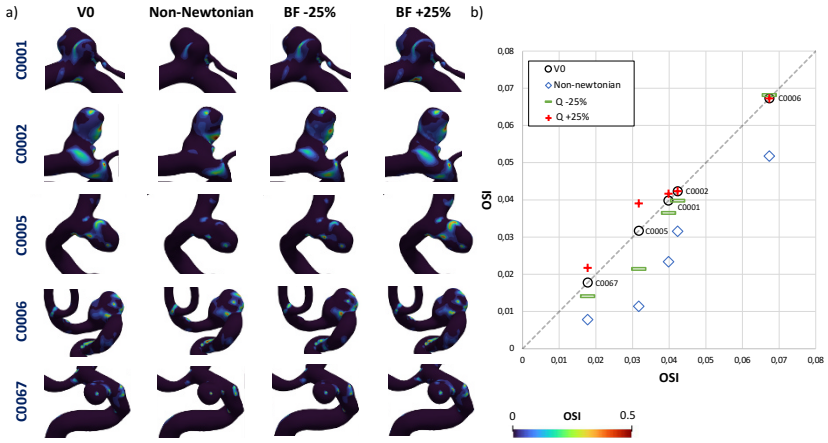

Fig. 7.3: a) Maps of OSI distribution. b) Effect of modeling assumptions on OSI with respect to the V0 simulation. *Q: blood flow. OSI: oscillatory shear index.*

Table 7.2: Impact of modeling assumptions: percentage variation of OSI with respect to V0 simulation. *Q: blood flow. OSI: oscillatory shear index.*

	OSI		
	Non-Newtonian	**Q - 25%**	**Q +25%**
C0001	-41,29	-8,53	4,64
C0002	-25,40	-6,15	0,11
C0005	-64,08	-32,46	23,23
C0006	-23,09	1,23	-0,08
C0067	-56,03	-20,85	22,42

7.4 Conclusion

7.4.1 Impact

Medical images available from clinical practice are extensively utilized for simulating CFD and exploring patient-specific vascular conditions, with the final aim of predicting rupture in cerebral aneurysms. However, most computational models are patient-specific in terms of their lumen geometry only and rely on numerous assumptions, which introduce a wide range of uncertainty and error.

In the current study we have performed CFD simulations under different modeling assumptions on 5 ICA aneurysms geometries. Specifically, our work aims at comparing the impact of the controversial non-Newtonian model (widespread model limitation) with that of inflow rates (major cause of uncertainty).

Our results demonstrate that TAWSS reacts more sensitively to flow changes compared to the linear relationship, with WSS varying by 33-44% for a 25% blood flow change. Conversely, changes in OSI with respect to inlet flow variations are more complex, exhibiting high variability. The non-Newtonian viscosity model notably affects CFD outcomes. TAWSS reduction due to the Modified Cross model matches a 25% blood flow reduction (-33/-42%). A high sensibility to the rheological properties of the fluid is also found in OSI values (-23/-56%). These findings underscore the need for patient-specific flow data and non-Newtonian rheology in CFD analysis to enhance reliability and reduce variability.

7.4.2 Relation to Others

Regarding the influence of inlet blood flow assumptions on WSS metrics, Evju [13] also noted a TAWSS decrease of -47% for a 25% reduction in blood flow. Similarly, OSI results align with existing literature, exhibiting complex behavior that does not correlate with inflow variations [28].

Addressing the variability linked to inlet flow rates could be alleviated by incorporating patient-specific flows measured via Doppler Ultrasound during clinical practice. The complexity deepens concerning the impact of the non-Newtonian model.

Steinman's review [6] delves into the non-Newtonian controversy, revealing that many CFD analyses overlook non-Newtonian viscosity due to computational costs outweighing perceived benefits. However, our work unveils a substantial influence of non-Newtonian viscosity on near-wall hemodynamic parameters. Our findings echo Mahrous' recent review on non-Newtonian CFD models of intracranial aneurysms, demonstrating that the commonly used Newtonian assumption leads to an overestimation of aneurysm WSS by 17-50% [29]. This effect extends to OSI, as highlighted by Oliveira [30], who observed an underestimation of surface-averaged OSI by over 30%. Thus, we sustain that incorporating a non-Newtonian viscosity model is pivotal and should be a consideration in future CFD studies on cerebral aneurysms.

7.4.3 Limitations

There are certain aspects of the patient-specific pipeline [6] that have not been explored in our discussion, representing limitations of our work and potential avenues for future research. For example, we have not taken into account the variability of rheological properties among individuals. As per [31], viscosity can vary by up to ±20% across different subjects. With regard to boundary conditions, our study did not explore the effects of different outflow conditions. We applied an inlet blood flow and waveform from literature to all models, regardless of parent artery diameters. The latter might lead to elevated WSS values in vessels with smaller calibers.

Further limitations include the lack of an assessment of imaging and lumen segmentation, known sources of error [32, 33]. Moreover, our post-processing exclusively targets the aneurysm sac region, with the selection of the cut zone at the aneurysm neck being arbitrary and operator-dependent, thereby introducing variability. Numerical considerations pose another limitation, as we did not extensively examine convergence in both space and time. However, the adopted spatial and temporal discretization guarantees the accuracy of the results. Lastly, our quantitative analysis focuses on the calculation of TAWSS and OSI, while numerous other hemodynamic indicators in the literature could be explored.

References

1. Monique HM Vlak. Prevalence of unruptured intracranial aneurysms, with emphasis on sex, age, comorbidity, country, and time period: a systematic review and meta-analysis. The Lancet Neurology, 10:626 – 636, 2011.
2. Juan C Lasheras. The biomechanics of arterial aneurysms. Annu. Rev. Fluid Mech., 39:293–319, 2007.
3. Juhana Frösen, Juan Cebral, Anne M Robertson, and Tomohiro Aoki. Flow-induced, inflammation-mediated arterial wall remodeling in the formation and progression of intracranial aneurysms. Neurosurgical focus, 47(1):E21, 2019.
4. Andre A Le Roux and M Christopher Wallace. Outcome and cost of aneurysmal subarachnoid hemorrhage. Neurosurgery Clinics, 21(2):235–246, 2010.

5. David O Wiebers. Unruptured intracranial aneurysms: natural history, clinical outcome, and risks of surgical and endovascular treatment. The Lancet, 362(9378):103–110, 2003.
6. David A. Steinman and Vitor M. Pereira. How patient specific are patient-specific computational models of cerebral aneurysms? an overview of sources of error and variability. Neurosurgical focus, 47(E14), 2019.
7. Tamer Hassan, Eugene V Timofeev, Masayuki Ezura, Tsutomu Saito, Akira Takahashi, Kazuyoshi Takayama, and Takashi Yoshimoto. Hemodynamic analysis of an adult vein of galen aneurysm malformation by use of 3d image-based computational fluid dynamics. American journal of neuroradiology, 24(6):1075–1082, 2003.
8. Liang-Der Jou, Christopher M Quick, William L Young, Michael T Lawton, Randall Higashida, Alastair Martin, and David Saloner. Computational approach to quantifying hemodynamic forces in giant cerebral aneurysms. American Journal of Neuroradiology, 24(9):1804–1810, 2003.
9. David A Steinman, Jaques S Milner, Chris J Norley, Stephen P Lownie, and David W Holdsworth. Image-based computational simulation of flow dynamics in a giant intracranial aneurysm. American Journal of Neuroradiology, 24(4):559–566, 2003.
10. Juan R Cebral, Fernando Mut, Jane Weir, and Christopher Putman. Quantitative characterization of the hemodynamic environment in ruptured and unruptured brain aneurysms. American Journal of Neuroradiology, 32(1):145–151, 2011.
11. Juan R Cebral, Fernando Mut, Jane Weir, and Christopher M Putman. Association of hemodynamic characteristics and cerebral aneurysm rupture. American Journal of Neuroradiology, 32(2):264–270, 2011.
12. Jianping Xiang, Sabareesh K Natarajan, Markus Tremmel, Ding Ma, J Mocco, L Nelson Hopkins, Adnan H Siddiqui, Elad I Levy, and Hui Meng. Hemodynamic–morphologic discriminants for intracranial aneurysm rupture. Stroke, 42(1):144–152, 2011.
13. Øyvind Evju, Kristian Valen-Sendstad, and Kent-André Mardal. A study of wall shear stress in 12 aneurysms with respect to different viscosity models and flow conditions. Journal of biomechanics, 46(16):2802–2808, 2013.
14. Ryo Torii, Marie Oshima, Toshio Kobayashi, Kiyoshi Takagi, and Tayfun E Tezduyar. Fluid–structure interaction modeling of blood flow and cerebral aneurysm: significance of artery and aneurysm shapes. Computer Methods in Applied Mechanics and Engineering, 198(45-46):3613–3621, 2009.
15. Yuri Bazilevs, M-C Hsu, Y Zhang, W Wang, X Liang, T Kvamsdal, R Brekken, and JG Isaksen. A fully-coupled fluid-structure interaction simulation of cerebral aneurysms. Computational mechanics, 46:3–16, 2010.
16. C Chnafa, O Brina, VM Pereira, and DA Steinman. Better than nothing: a rational approach for minimizing the impact of outflow strategy on cerebrovascular simulations. American journal of neuroradiology, 39(2):337–343, 2018.
17. Alberto Marzo, Pankaj Singh, Ignacio Larrabide, Alessandro Radaelli, Stuart Coley, Matt Gwilliam, Iain D Wilkinson, Patricia Lawford, Philippe Reymond, Umang Patel, et al. Computational hemodynamics in cerebral aneurysms: the effects of modeled versus measured boundary conditions. Annals of biomedical engineering, 39:884–896, 2011.
18. Steinman DA Valen-Sendstad K. Mind the gap: impact of computational fluid dynamics solution strategy on prediction of intracranial aneurysm hemodynamics and rupture status indicators. American journal of neuroradiology, 35(3):536–43, 2014.
19. Steinman DA Khan MO, Valen-Sendstad K. Narrowing the expertise gap for predicting intracranial aneurysm hemodynamics: Impact of solver numerics versus mesh and time-step resolution. American journal of neuroradiology, 37(7):1310–1316, 2015.
20. Aneurisk-Team. AneuriskWeb project website, http://ecm2.mathcs.emory.edu/aneuriskweb. Web Site, 2012.
21. Yiemeng Hoi, Bruce A Wasserman, Yuanyuan J Xie, Samer S Najjar, Luigi Ferruci, Edward G Lakatta, Gary Gerstenblith, and David A Steinman. Characterization of volumetric flow rate waveforms at the carotid bifurcations of older adults. Physiological measurement, 31(3):291, 2010.

22. Mikael Mortensen and Kristian Valen-Sendstad. Oasis: a high-level/high-performance open source navier–stokes solver. Computer physics communications, 188:177–188, 2015.
23. Fenics project. https://fenicsproject.org/, 2019-04-01. 0.4.
24. George Em Karniadakis, George Karniadakis, and Spencer Sherwin. Spectral/hp element methods for computational fluid dynamics. Oxford University Press, 2005.
25. Henrik A. Kjeldsberg, Aslak W. Bergersen, and Kristian Valen-Sendstad. Vampy: An automated and objective pipeline for modeling vascular geometries. Journal of Open Source Software, 8(85):5278, 2023.
26. MO Khan, K Valen-Sendstad, and DA Steinman. Direct numerical simulation of laminar-turbulent transition in a non-axisymmetric stenosis model for newtonian vs. shear-thinning non-newtonian rheologies. Flow, Turbulence and Combustion, 102:43–72, 2019.
27. AL Haley, K Valen-Sendstad, and DA Steinman. On delayed transition to turbulence in an eccentric stenosis model for clean vs. noisy high-fidelity cfd. Journal of Biomechanics, 125:110588, 2021.
28. Hamidreza Rajabzadeh-Oghaz, Pim van Ooij, Sricharan S Veeturi, Vincent M Tutino, Jaco JM Zwanenburg, and Hui Meng. Inter-patient variations in flow boundary conditions at middle cerebral artery from 7t pc-mri and influence on computational fluid dynamics of intracranial aneurysms. Computers in biology and medicine, 120:103759, 2020.
29. Samar A Mahrous, Nor Azwadi Che Sidik, and Khalid M Saqr. Newtonian and non-newtonian cfd models of intracranial aneurysm: a review. CFD Letters, 12(1):62–86, 2020.
30. Iago L Oliveira, Gabriel B Santos, José L Gasche, Julio Militzer, and Carlos E Baccin. Non-newtonian blood modeling in intracranial aneurysm hemodynamics: impact on the wall shear stress and oscillatory shear index metrics for ruptured and unruptured cases. Journal of Biomechanical Engineering, 143(7):071006, 2021.
31. Frieke MA Box, Rob J van der Geest, Marcel CM Rutten, and Johan HC Reiber. The influence of flow, vessel diameter, and non-newtonian blood viscosity on the wall shear stress in a carotid bifurcation model for unsteady flow. Investigative radiology, 40(5):277–294, 2005.
32. Kristian Valen-Sendstad, Aslak W Bergersen, Yuji Shimogonya, Leonid Goubergrits, Jan Bruening, Jordi Pallares, Salvatore Cito, Senol Piskin, Kerem Pekkan, Arjan J Geers, et al. Real-world variability in the prediction of intracranial aneurysm wall shear stress: the 2015 international aneurysm cfd challenge. Cardiovascular engineering and technology, 9:544–564, 2018.
33. Philipp Berg, Samuel Voß, Sylvia Saalfeld, Gábor Janiga, Aslak W Bergersen, Kristian Valen-Sendstad, Jan Bruening, Leonid Goubergrits, Andreas Spuler, Nicole M Cancelliere, et al. Multiple aneurysms anatomy challenge 2018 (match): phase i: segmentation. Cardiovascular engineering and technology, 9:565–581, 2018.